An Electromagnetic Trapping Platform for Single Molecule Studies

by

Chang Jiang

A dissertation submitted in partial fulfillment
of the requirements for the degree of
Doctor of Philosophy
(Mechanical Engineering)
in the University of Michigan
2015

Doctoral committee:

Professor Edgar Meyhöfer, Chair
Associate Professor Wei Cheng
Assistant Professor Jianping Fu
Professor Noel C. Perkins

DEDICATION

To my dad, Xiangming Jiang, and my mom, Yunjuan Wang –

Thank you for your unconditional love and support.

ACKNOWLEDGEMENT

This dissertation is the product of many years of effort under the guidance of my advisor, Edgar Meyhofer. It was he who constantly challenged me, taught me how to think critically with a scientific mind, and how to be patient and persistent through research. His support, advice and expertise helped me to progressively learn how to become an independent researcher and made my graduate work possible. The conversation with him has always been inspiring, philosophical, and joyful. This makes him my great mentor, my kind friend and my motivating supervisor.

I am extremely thankful to my colleagues and collaborators. I'm particularly grateful to Jenna Campbell, Neha Kaul, Troy Lionberger, Diane Wiener, Dakotah Thompson, and Erika Cline, who made our lab a friendly and supportive environment. Thank you for your effort, advice and insights that contributed to the fruition of my research; thank you for the encouragement you gave me when I was baffled by the obstacles during my study and research; thank you for the laughter you brought to my daily work through graduate life.

I would like to acknowledge the support I received from my committee members, Noel Perkins, Jianping Fu and Wei Cheng. I am extremely grateful to the valuable time and insightful advice that they generously gave to me. Their response to my questions was always speedy. Their advice broadened my perspective on my projects.

Finally, I would like to thank my family and friends, who have given me unconditional support through my graduate life. My parents' love and encouragement have been critical to my accomplishments. Their motivation and support gave me strength in overcoming every hurdle I encountered during my study and research.

TABLE OF CONTENTS

LIST OF FIGURES

LIST OF ABBREVIATIONS

ADP	adenosine diphosphate
AMPPNP	adenosine 5’-(β,γ-imido)triphosphate
ATP	adenosine triphosphate
BSA	bovine serum albumin
DBI	dual-color bifocal imaging system
DNA	deoxyribonucleic acid
DTT	dithiothrietol
eMT	electromagnetic tweezers
MES	2-(N-morpholino)ethanesulfonic acid
$MgCl_2$	magnesium chloride
MT	magnetic tweezers
N.A.	numerical aperture
ODFS	oblique dark-field scattering system
op-amp	operational amplifier
PBS	phosphate buffered saline
RNA	ribonucleic acid
RNAP	RNA polymerase
TIRFM	total internal reflection fluorescence microscopy

Chapter 1

BACKGROUND

In this chapter, I will begin with a discussion of the roles that mechanics play in biological processes, and I will review the techniques that have been developed to study the effect of force and torque perturbation on biological processes. The understanding of how mechanical perturbation can influence the kinetics of biological reactions and structural dynamics of biological molecules will help us gain insights into the molecular mechanism of biological machineries. In particular, I will review the development and recent advancement of magnetic tweezers, and its application to a range of microbiological and single molecule investigations. Then I will discuss how single molecule fluorescence imaging, and single molecule fluorescence resonance energy transfer (smFRET) have contributed to the understanding of the kinetics and dynamics of biomolecules and the interaction between biomolecules. I will look at examples as to how a novel technique, where the mechanical status of the biomolecule can be controlled and monitored simultaneously with fluorescence microscopy, can reveal valuable information about the kinetics and structural dynamics of biomolecules under force and torque. I will discuss the challenges of the implementation of this novel technique and provide specifications that are required to achieve such instrumentation.

1.1 Forces and Torques in Biology

Mechanics plays a fundamental role in biological processes. Many critical cellular processes are driven by linear forces. Cell motility, a highly dynamic phenomenon that is essential to chemotaxis, wound healing, cancer metastasis and immune response, requires force generated by cytoskeleton and motor proteins, in particular, the actin-myosin system that transduces chemical energy in the form of ATP, an energy source used in most cellular metabolism, into mechanical energy[1]. Intracellular transport, the trafficking of proteins, organelles and mRNA to the locations where they are needed in the cell, is essential for cellular function, survival and morphogenesis. Such transport is conducted by motor proteins that need to overcome viscous drag forces in the crowded cellular environment, and the free energy driving the mechanical motion is also coupled with the chemical reaction of ATP hydrolysis[2,3].

On the other hand, the importance of torque involved in biological processes can be appreciated in the example of rotating motion of the flagellar motor, a protein complex embedded in the plasma membrane of bacteria, such as *Eschericia coli* and *Salmonella typhimurium*[4]. The rotary motion of the motor protein is driven by the proton gradient that exists across the plasma membrane and is required for propelling the flagella of bacteria, making their motility possible. Another example is a related rotary motor, F_0F_1-ATPase, whose rotational motion, depending on the direction, can be used either to synthesize ATP, or to restore the proton gradient across the plasma membrane by hydrolyzing ATP[5,6].

The interplay of force and torque can be appreciated by the example of nucleic acid under mechanical stress during essential processes such as DNA replication, and transcription of DNA into RNA by RNA polymerases. It has been established that DNA topology can be changed when forces and torques are applied to DNA. DNA molecules store and preserve the genetic code that defines the organisms and determines all their functions. During each cell cycle, DNA molecules go through replication and transcription, both of which require that the double-stranded, helical structure of DNA molecules be separated into single-stranded DNA so that their genetic information can be accessed by DNA binding proteins, such as DNA polymerases during replication, and RNA polymerase in the case of transcription. Such essential cellular processes that involve the interaction between DNA molecule and the machineries that open the double-stranded helix when they track along DNA are mechanical processes in nature. When these DNA tracking translocases, such as DNA and RNA polymerases, move along DNA templates, individual translocases can exert up to tens of piconewton of force on DNA during actions[7-9]. In the meantime, the unwinding of the DNA double helix to access the genetic information results in rotational motion and the generation of torsional strains[10], and the translocases need to overcome the torsional stress stored in the DNA double-helical structure in order to access the DNA nucleotide bases[11]. This accumulated torque induces supercoiling of the DNA molecule on long-length scales, positive in the front and negative in the rear[12–14]. Supercoiling is defined as a change of the DNA linking number away from its intrinsic, torsionally relaxed helicity of one turn per 10.5 base pairs. The sum of twist, the number of times that the two strands are twisted about each other, and writhe, the number of times that the DNA helix is coiled about itself in three-dimensional space, is defined as DNA's linking number, the total number of times one strand of the DNA helix is linked with the other in a covalently closed circular molecule.

Supercoiling can lead to formation of plectonemes and can alter the structure of DNA away from its canonical B-form. Such structural change is essential to many biological processes. Although the genetic information encoded in DNA is embodied in a one-dimensional array of sequences, it is the three-dimensional structure of the genetic material that controls how this information is replicated, expressed, and recombined in the cell[15–17]. In *E.coli*, the best-studied prokaryotic bacteria, the chromosome is negatively supercoiled[18]. In eukaryotes, about every 146 base-pairs of DNA is wound on nucleosomes, a protein octamer that consists of histones[19], and such nucleosomal arrays are further compacted to form the chromatin structure. To regulate the degree of supercoiling, cells developed a family of proteins called topoisomerases to constantly modify the three-dimensional topology of DNA, which is critical for cellular processes and cell viability[20-23]. DNA topoisomerases introduce temporary single- or double-strand breaks in the DNA to solve the topological problems associated with DNA replication, transcription, recombination, and chromatin remodeling. In addition, these enzymes adjust the level of DNA supercoiling both to facilitate protein interactions with the DNA and to prevent excessive supercoiling that is deleterious.

1.2 Magnetic tweezers for Biological Studies

The ability to study these fundamental processes has been revolutionized over the past two decades by the development of single-molecule force spectroscopy techniques that allow application and measurement of force, torque, displacement and rotation generated by molecules ranging from nucleic acids to proteins. Conventional biochemical ensemble assays are not suitable for characterizing the aforementioned mechanical properties, because these approaches lack the capability of controllably extending and/or twisting biomolecules to mimic the mechanical stresses that are imparted to biomolecules in the cell, nor do they have the time resolution to distinguish the fast dynamical changes in DNA conformation and to study mechanochemical reaction cycles. Single-molecule biomechanics is an emerging field that is capable of overcoming these technical limitations,

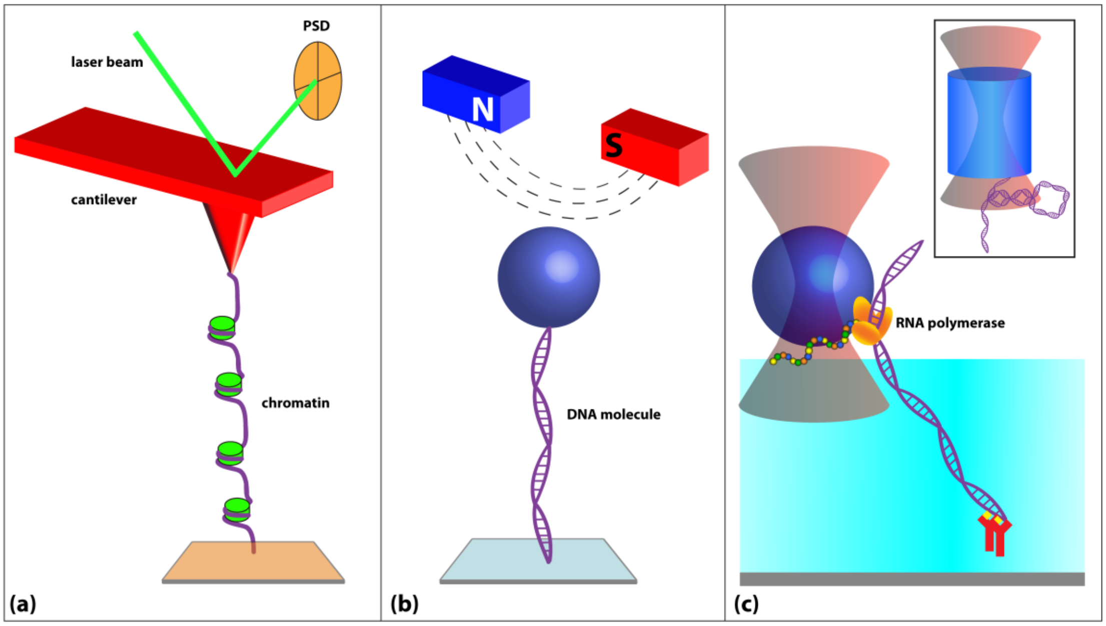

Figure 1.1 Single-molecule force spectroscopy techniques. (a) Schematic of an atomic force microscopy assay. A piece of molecule is tethered to the sharp tip of the AFM cantilever that is placed above a piezoelectric scanning stage. The retraction of the scanning stage along vertical axis applies force to the molecule, deflecting the cantilever. The deflection is detected by the laser beam reflected off the cantilever onto a position sensitive detector. (b) Schematic of a magnetic tweezers assay. A DNA molecule is tether to a superparamagnetic bead on one end and to the surface of the chamber on the other end. The bead is pulled upward and rotated along the optical axis of the microscope objective by an external magnetic field that is generated by a pair of magnets, imparting force and torque to the attached DNA molecule. (c) Schematic of an optical tweezers assay. A polystyrene or silica bead is trapped by a laser trap. A DNA tracking enzyme is attached to the bead and as the enzyme translocates along DNA molecule that is immobilized on the surface of the chamber, the bead is pulled along DNA, away from the equilibrium position of the laser trap. Inset shows that using an optically anisotropic birefringent particle allows torque to be generated on the particle by polarized laser beam.

principally because here the mechanical state of biological molecules or molecular system is precisely controlled in the experiment and the ensuing responses are directly observed.

In the past two decades force spectroscopy techniques have been developed that allow direct application of force and torque on biological macromolecules[24–28]. Methods such as atomic force microscopy (AFM), optical tweezers (OT)[29–33], and magnetic tweezers (MT)[34–38], have been invented and applied to study mechanical properties of proteins and DNA molecules. Detailed measurements of the tensional[39,40] and torsional[41–45] elasticity of DNA molecule allowed investigation of nucleic-acid molecular motors and proteins that modify DNA, in an unconventional manner that circumvents the averaging effects of ensemble biochemical assays[46-49]. Such direct measurement of the effect of mechanical perturbation on DNA and DNA binding protein dynamics offers an unprecedented opportunity for unambiguously studying the mechanical properties of DNA and its effect on biological functionality of associated proteins. Hence developing an instrument that allows directly applying torque and force on DNA molecule using single-molecule assay

	AFM	Magnetic tweezers	Optical tweezers
Force rang(pN)	$10\text{-}10^5$	$10^{-3}\text{-}10^4$	$10^{-2}\text{-}10^2$
No heating and photodamage	Yes	Yes	No
Parallel	No	Yes	No
Torque	No	Yes	Yes
3D position and rotation control	No	Yes	No
Decoupling of force and torque	No	Yes	No

Table 1.1 Comparison of single-molecule force spectroscopy techniques.

is not only suitable but also necessary for an unambiguous study of how torsional stress in DNA is coupled to its conformational change and how kinetics of the biochemical reactions of DNA binding proteins are dependent on the torsional states in the template DNA.

Magnetic tweezers are an instrument that uses magnetic fields to impart a force or torque to the substrate of interest[38]. It has been proven to be a powerful tool to elucidate the biomechanical properties essential for cell functions. In the past, a quadruple-tip magnetic trap was developed for atomic physics[50], as well as single-pole[51] and four-pole[52] configurations were used for biophysics applications. Ever since Crick's first *in vitro* studies of the viscoelastic properties of cytoplasm[53], magnetic forces have been used to investigate a wide range of biophysical properties[54], from the cellular-level study of mechanotransduction across the cell membrane and through the cytoskeleton[55], to the molecular-level studies of stiffness of antibody-antigen complex[56], function of F1-ATPase in ATP synthesis as a component of F_0F_1-ATP synthase[57] and its stiffness[58], and interaction between histones and DNA[59]. Various forms of magnetic tweezers have been developed using different sources for generating magnetic fields to directly apply perturbation including forces and torques to DNA and DNA binding proteins through manipulating the paramagnetic beads as force probes conjugated to biomolecules. Permanent magnets[60–62], electromagnets[63,64] and MEMS lab-on-chip devices[65,66], have been utilized to study the mechanical properties of DNA, and DNA supercoiling and conformational transition[67,68],as well as changes of DNA's physical properties regulated by small molecule binding[69].

1.3 Single Molecule Fluorescence Imaging

Single molecule fluorescence measurements have revolutionized biological inquiries by providing previously unobtainable data on elementary molecular processes[70].

Single molecule fluorescence microscopy aims to optically detect the location of target molecules by specifically labeling them with fluorophores. The spatial resolution using conventional fluorescence microscopy is normally limited to ~200nm, predicted by Abbe diffraction limit. However, recent development in fluorescence technology including FIONA (fluorescence imaging with one nanometer accuracy)[71,72], STED (stimulated emission depletion)[73], SOFI (super-resolution optical fluctuation imaging), and superresolution imaging techniques[74,75] based on stochastic localization, such as FPALM (fluorescence photoactivation localization microscopy)[76,77] and STORM (stochastic optical reconstruction microscopy)[78], has overcome the diffraction limit and achieved localization of objects with sizes down to 2-20nm. In TIRFM (total internal reflection microscopy), excitation laser beam creates an evanescent electromagnetic field that penetrates into the limited specimen region immediately adjacent to the interface between two media having different refractive indices, activating only the fluorophores located within a distance of typically several hundred nanometers from the substrate. This significantly reduces background fluorescence from outside the focal plane and dramatically improves the signal-to-noise ratio of the fluorescent images. TIRFM has been extensively used to investigate a wide range of biological processes[79], e.g., formation of amyloid fibril associated with Alzheimer's disease[80], molecular interactions on lipid membrane surfaces[81], actin polymerization and its regulation[82], and the effect of post-translational modification of tubulin on the motility of motor molecules[83], to name just a few, and it has also been used in drug discoveries[84].

Fluorescence resonance energy transfer (FRET) extends fluorescence imaging to investigate various biological systems involving either intramolecular interactions, such as conformational dynamics of DNA, RNA, and proteins, or intermolecular interactions of proteins with DNA, RNA, and other ligands[85–87]. FRET between a donor and an acceptor fluorophore takes place, via dipole-dipole interaction, when they are within 10 nm of each other, making it an attractive method for probing distances and distance dynamics in and between biological macromolecules. smFRET (FRET at the single-molecule level) has rapidly developed to answer fundamental questions about replication, recombination, transcription, translation, RNA folding and catalysis[88]. For example, smFRET was used to monitor the initiation and elongation complexes during transcription of the model enzyme, T7 RNA polymerase (RNAP) found in bacteriophage, and found that the rate-limiting step in the transcription process lies in the transition from transcription initiation to elongation of the RNAP[89]. Goldman's group used smFRET to investigate the influence of strong downstream mRNA secondary structures, such as stem-loops or pseudoknots, on the reaction rates for specific steps within the elongation cycle of the *Escherichia coli* ribosome during translation process[90].

1.4 Combining magnetic tweezers with fluorescence microscopy

As powerful as force spectroscopy and fluorescence microscopy are individually, their combination allows for addressing unique questions that cannot be answered with either single technique alone. Combining magnetic tweezers with fluorescence microscopy offers additional possibilities for studying single molecule behavior[91]. Smith et al. was among the first to have used epifluorescence microscope with magnetic tweezers[39]. The magnetic tweezers were used to apply an upward pulling force and in the meantime flow force was used to extend DNA in the horizontal direction. The movement of DNA was monitored by fluorescently labeling DNA with a large number of ethidium bromide molecules via intercalation. The elasticity of DNA was derived from the force-extension curve and the effect of intercalating agent on the elasticity was revealed. Combined with TIRFM and fluorescence polarization microscopy, Hugel et al. used magnetic tweezers to investigate the putative rotary motion model of the portal motor connector of bacteriophage Φ29 for the purpose of understanding the mechanism of packing the double-stranded DNA of the viral genome into its protein capsid[92]. In their experiment, while the activity of the viral DNA packing was being watched by the decrease in the length of DNA tethered to a magnetic bead, the orientation of the motor was monitored by TIRF polarization microscopy. Adachi et al studied conversion of Cy3-ATP into Cy3-ADP by F1-ATPase under forced rotation, by combining single-molecule imaging of a fluorescent ATP analog and applying a torque against F1-ATPase motion using magnetic tweezers[93]. These experiments revealed valuable kinetic information and the mechanism of the biological processes that are intrinsically mechanical by nature. With similar method, the calibration of one of the first artificial molecular force sensors was also achieved by stretching a piece of immobilized single-stranded DNA molecule labeled with two fluorophores that form a FRET pair[94].

1.5 Motivation Statement and Research Goals

Despite recent advancement in the development of magnetic tweezers, simultaneous force and torque applications in which the two components are decoupled and controlled independently remain challenging, and have only been implemented by recently-developed hybrid magnetic tweezers combining electro- and permanent magnets[95]. Electromagnetic tweezers offer certain advantages over magnetic tweezers composed of permanent magnets, including easy modulation of the magnetic field by changing the currents applied to the electromagnetic solenoid coils, eliminating the need for mechanical positioners to translate or rotate the permanent magnets in permanent magnetic tweezers. In addition, the current in solenoids can be changed at a time scale much faster than common mechanical positioners, allowing it to increase the bandwidth of the experiments and introduce various forms of feedback control. My first goal was to design and implement *bona fide* electromagnetic tweezers (eMT) that can apply force and torque on single biomolecules or polymer molecules conjugated via superparamagnetic microspheres, and can control the two components independently simply by changing the currents applied to different coils of the eMT. This instrument offers flexibility in manipulating the tension and torsion applied to biomolecules and has the potential to provide novel insights for a variety of biological processes such as transcription, translation and DNA replication.

The combination of force spectroscopy using magnetic tweezers and FRET measurement has been used to investigate biological processes, but the combination of torque spectroscopy and fluorescence imaging has not been fully explored. Such combination will allow yet-to-be-achieved but surely important studies, such as how conformations of DNA-bound proteins are affected by the supercoiling state of DNA. Firstly, the capability of monitoring the torsional status of the biomolecule by detecting the angular motion of the force probe is necessary for accurate implementation of torque spectroscopy, meanwhile it needs to be implemented so that it does not interfere with the fluorescence detection. Secondly, the current imaging based techniques for detecting the angular orientation of force probes usually entail time-consuming post-processing of images, limiting the temporal resolution of the experiments, accompanied by a high demand in computational power. To overcome these shortcomings, my second goal was to develop a novel method for tracking rotational motion that does not interfere with the biological fluorescence detection and is capable of mapping angular motion to electrical signals acquired by optoelectronic devices, allowing angular detection with higher bandwidth.

A dual-color imaging device allows the simultaneous visualization of two different wavelengths emitted from a sample, and is commonly used in FRET measurements. Because of the chromatic aberration from the optics in the microscope, which is common for a microscope objective with high numerical aperture, such as that employed in objective-type TIRFM, focusing simultaneously two wavelength onto the same CCD camera remains challenging. Furthermore, diffraction limited applications such as protein co-localization are very sensitive to the registration between the two channels, and superresolution imaging techniques based on stochastic localization typically require long-period acquisition. Therefore, channel-registration and long-term relative drift between the two channels are important to the accuracy and applicability of the instrument to biological single molecule studies. My third goal was to develop an imaging system that can detect spectrally and spatially differentiated fluorescent particles using a single CCD camera with high-precision registration and low long-term mechanical drift.

In this thesis, chapter 2 and chapter 3 will describe the design and characterization of the magnetic tweezers instrument based completely on electromagnets, which can independently control force and torque on micrometer-sized magnetic beads. Chapter 4 will present the methodology that allows using an optoelectronic system to directly record the angular displacement of particles undergoing rotational motion by using asymmetric illumination of optically anisotropic beads. In chapter 5, I will describe a dual-color and bifocal imaging system that allows two spatially identical images with distinct emission spectra to be simultaneously acquired by a single camera, while the two channels can be independently and continuously focused.

1.6 Bibliography

1. Lodish, H. *et al. Molecular Cell Biology*. (W. H. Freeman, 2000).
2. Hirokawa, N., Noda, Y., Tanaka, Y. & Niwa, S. Kinesin superfamily motor proteins and intracellular transport. *Nat Rev Mol Cell Biol* **10,** 682–696 (2009).
3. Tomlin, S. G. Vesicular transport across endothelial cells. *Biochim Biophys Acta* **183,** 559–64 (1969).
4. Sowa, Y. & Berry, R. M. The Rotary Bacterial Flagellar Motor. *Comprehensive Biophysics, Vol 8: Bioenergetics* (2011).
5. Capaldi, R. A., Aggeler, R., Gogol, E. P. & Wilkens, S. Structure of the Escherichia coli ATP synthase and role of the gamma and epsilon subunits in coupling catalytic site and proton channeling functions. *J. Bioenerg. Biomembr.* **24,** 435–439 (1992).
6. Deckers-Hebestreit, G. & Altendorf, K. The F_0F_1-type ATP synthases of bacteria: structure and function of the F_0 complex. *Annu. Rev. Microbiol.* **50,** 791–824 (1996).
7. Yin, H., Landick, R. & Gelles, J. Tethered particle motion method for studying transcript elongation by a single RNA polymerase molecule. *Biophys J* **67,** 2468–78 (1994).
8. Wang, M. D. *et al.* Force and velocity measured for single molecules of RNA polymerase. *Science* **282,** 902–7 (1998).
9. Yin, H. *et al.* Transcription against an applied force. *Science* **270,** 1653–1657 (1995).
10. Liu, L. F. & Wang, J. C. Supercoiling of the DNA template during transcription. *Proc Natl Acad Sci* **84,** 7024–7 (1987).
11. Ma, J., Bai, L. & Wang, M. D. Transcription Under Torsion. *Science* **340,** 1580–1583 (2013).
12. Liu, L. F. & Wang, J. C. Supercoiling of the DNA template during transcription. *Proc Natl Acad Sci* **84,** 7024–7 (1987).

13. Rahmouni, A. R. & Wells, R. D. Direct evidence for the effect of transcription on local DNA supercoiling in vivo. *Journal of Molecular Biology* **223,** 131–144 (1992).
14. Wu, H. Y., Shyy, S., Wang, J. C. & Liu, L. F. Transcription generates positively and negatively supercoiled domains in the template. *Cell* **53,** 433–440 (1988).
15. Kanaar, R. & Cozzarelli, N. R. Roles of supercoiled DNA structure in DNA transactions. *Current Opinion in Structural Biology* **2,** 369–379 (1992).
16. Kahn, W. J. D. DNA topology: Applications to gene expression. *Current Organic Chemistry* **6,** 815–826 (2002).
17. Deweese, J. E. & Osheroff, N. The DNA cleavage reaction of topoisomerase II: wolf in sheep’s clothing. *Nucleic Acids Res* **37,** 738–48 (2009).
18. Worcel, A. & Burgi, E. Structure of folded chromosome of Escherichia coli. *Journal of Molecular Biology* **71,** 127–& (1972).
19. Luger, K., Mader, A. W., Richmond, R. K., Sargent, D. F. & Richmond, T. J. Crystal structure of the nucleosome core particle at 2.8 Å resolution. *Nature* **389,** 251–60 (1997).
20. Drlica, K. Control of bacterial DNA supercoiling. *Mol Microbiol* **6,** 425–33 (1992).
21. Stasiak, A. DNA topology: Feeling the pulse of a topoisomerase. *Current Biology* **10,** R526–R528 (2000).
22. Champoux, J. J. DNA Topoisomerases: Structure, Function, and Mechanism. *Annual Review of Biochemistry* **70,** 369–413 (2001).
23. Koster, D. A., Crut, A., Shuman, S., Bjornsti, M.-A. & Dekker, N. H. Cellular Strategies for Regulating DNA Supercoiling: A Single-Molecule Perspective. *Cell* **142,** 519–530 (2010).
24. Clausen-Schaumann, H., Rief, M., Tolksdorf, C. & Gaub, H. E. Mechanical stability of single DNA molecules. *Biophys J* **78,** 1997–2007 (2000).
25. Strick, T. R. & et al. Stretching of macromolecules and proteins. *Reports on Progress in Physics* **66,** 1 (2003).
26. Neuman, K. C., Lionnet, T. & Allemand, J. F. Single-molecule micromanipulation techniques. *Annual Review of Materials Research* **37,** 33–67 (2007).
27. Neuman, K. C. & Nagy, A. Single-molecule force spectroscopy: optical tweezers, magnetic tweezers and atomic force microscopy. *Nat Methods* **5,** 491–505 (2008).

28. Walter, N. G., Huang, C. Y., Manzo, A. J. & Sobhy, M. A. Do-it-yourself guide: how to use the modern single-molecule toolkit. *Nature Methods* **5,** 475–489 (2008).
29. Wang, M. D. *et al.* Force and velocity measured for single molecules of RNA polymerase. *Science* **282,** 902–7 (1998).
30. Bennink, M. L. *et al.* Single-molecule manipulation of double-stranded DNA using optical tweezers: interaction studies of DNA with RecA and YOYO-1. *Cytometry* **36,** 200–8 (1999).
31. La Porta, A. & Wang, M. D. Optical torque wrench: angular trapping, rotation, and torque detection of quartz microparticles. *Phys Rev Lett* **92,** 190801 (2004).
32. Oroszi, L. *et al.* Direct Measurement of Torque in an Optical Trap and Its Application to Double-Strand DNA. *Phys Rev Lett* **97,** 058301 (2006).
33. Forth, S. *et al.* Abrupt buckling transition observed during the plectoneme formation of individual DNA molecules. *Phys Rev Lett* **100,** 148301 (2008).
34. Bustamante, C., Macosko, J. C. & Wuite, G. J. Grabbing the cat by the tail: manipulating molecules one by one. *Nat Rev Mol Cell Biol* **1,** 130–6 (2000).
35. Gosse, C. & Croquette, V. Magnetic tweezers: Micromanipulation and force measurement at the molecular level. *Biophys J* **82,** 3314–3329 (2002).
36. Zlatanova, J. & Leuba, S. H. Magnetic tweezers: a sensitive tool to study DNA and chromatin at the single-molecule level. *Biochemistry and Cell Biology* **81,** 151–159 (2003).
37. Crut, A., Koster, D. A., Seidel, R., Wiggins, C. H. & Dekker, N. H. Fast dynamics of supercoiled DNA revealed by single-molecule experiments. *Proc Natl Acad Sci* **104,** 11957–62 (2007).
38. Vilfan, I. D., Lipfert, J., Koster, D. A., Lemay, S. G. & Dekker, N. H. in *Handbook of Single-Molecule Biophysics* 371–395 (Springer New York, 2009).
39. Smith, S. B., Finzi, L. & Bustamante, C. Direct mechanical measurements of the elasticity of single DNA molecules by using magnetic beads. *Science* **258,** 1122–6 (1992).
40. Strick, T. R., Allemand, J. F., Bensimon, D., Bensimon, A. & Croquette, V. The elasticity of a single supercoiled DNA molecule. *Science* **271,** 1835–7 (1996).

41. Lipfert, J., Wiggin, M., Kerssemakers, J. W. J., Pedaci, F. & Dekker, N. H. Freely orbiting magnetic tweezers to directly monitor changes in the twist of nucleic acids. *Nat Commun* **2,** 439 (2011).
42. Lipfert, J., Kerssemakers, J. W., Jager, T. & Dekker, N. H. Magnetic torque tweezers: measuring torsional stiffness in DNA and RecA-DNA filaments. *Nat Methods* **7,** 977–80 (2010).
43. Lipfert, J., Klijnhout, S. & Dekker, N. H. Torsional sensing of small-molecule binding using magnetic tweezers. *Nucleic Acids Res* **38,** 7122–7132 (2010).
44. Lipfert, J., Lee, M., Ordu, O., Kerssemakers, J. W. J. & Dekker, N. H. Magnetic Tweezers for the Measurement of Twist and Torque. e51503 (2014).
45. Lebel, P., Basu, A., Oberstrass, F. C., Tretter, E. M. & Bryant, Z. Gold rotor bead tracking for high-speed measurements of DNA twist, torque and extension. *Nat Meth* (2014).
46. Charvin, G., Strick, T. R., Bensimon, D. & Croquette, V. Topoisomerase IV bends and overtwists DNA upon binding. *Biophys J* **89,** 384–392 (2005).
47. Gore, J. *et al.* Mechanochemical analysis of DNA gyrase using rotor bead tracking. *Nature* **439,** 100–4 (2006).
48. Koster, D. A., Palle, K., Bot, E. S. M., Bjornsti, M.-A. & Dekker, N. H. Antitumour drugs impede DNA uncoiling by topoisomerase I. *Nature* **448,** 213–217 (2007).
49. Basu, A., Schoeffler, A. J., Berger, J. M. & Bryant, Z. ATP binding controls distinct structural transitions of Escherichia coli DNA gyrase in complex with DNA. *Nat Struct Mol Biol* **19,** 538–546 (2012).
50. Vuletic, V., Hansch, T. W. & Zimmermann, C. Steep magnetic trap for ultra cold atoms. *Europhysics Letters* **36,** 349–354 (1996).
51. Alenghat, F. J., Fabry, B., Tsai, K. Y., Goldmann, W. H. & Ingber, D. E. Analysis of cell mechanics in single vinculin-deficient cells using a magnetic tweezer. *Biochemical and Biophysical Research Communications* **277,** 93–99 (2000).
52. Amblard, F., Yurke, B., Pargellis, A. & Leibler, S. A magnetic manipulator for studying local rheology and micromechanical properties of biological systems. *Rev Sci Instrum* **67,** 818–827 (1996).

53. Crick, F. H. C. & Hughes, A. F. W. The physical properties of cytoplasm: A study by means of the magnetic particle method Part I. Experimental. *Experimental Cell Research* **1,** 37–80 (1950).
54. Fisher, J. K. *et al.* Magnetic force micromanipulation systems for the biological sciences. *Nano* **1,** 191–205 (2006).
55. Wang, N., Butler, J. P. & Ingber, D. E. Mechanotransduction across the cell surface and through the cytoskeleton. *Science* **260,** 1124–1127 (1993).
56. Janssen, X. J. A. *et al.* Torsion Stiffness of a Protein Pair Determined by Magnetic Particles. *Biophys J* **100,** 2262–2267 (2011).
57. Saita, E. *et al.* Activation and Stiffness of the Inhibited States of F(1)-ATPase Probed by Single-molecule Manipulation. *Journal of Biological Chemistry* **285,** 11411–11417 (2010).
58. Okuno, D., Iino, R. & Noji, H. Stiffness of gamma subunit of F(1)-ATPase. *European Biophysics Journal with Biophysics Letters* **39,** 1589–1596 (2010).
59. Fisher, J. K. *et al.* Thin-foil magnetic force system for high-numerical-aperture microscopy. *Rev Sci Instrum* **77,** nihms8302 (2006).
60. Celedon, A. *et al.* Magnetic tweezers measurement of single molecule torque. *Nano Lett* **9,** 1720–5 (2009).
61. Klaue, D. & Seidel, R. Torsional stiffness of single superparamagnetic microspheres in an external magnetic field. *Phys Rev Lett* **102,** 028302 (2009).
62. Lipfert, J., Koster, D. A., Vilfan, I. D., Hage, S. & Dekker, N. H. Single-molecule magnetic tweezers studies of type IB topoisomerases. *Methods Mol Biol* **582,** 71–89 (2009).
63. Fisher, J. K. *et al.* Three-dimensional force microscope: A nanometric optical tracking and magnetic manipulation system for the biomedical sciences. *Rev Sci Instrum* **76,** (2005).
64. Fisher, J. K. *et al.* Thin-foil magnetic force system for high-numerical-aperture microscopy. *Rev Sci Instrum* **77,** nihms8302 (2006).
65. Chaves, R. C., Bensimon, D. & Freitas, P. P. Single molecule actuation and detection on a lab-on-a-chip magnetoresistive platform. *Journal of Applied Physics* **109,** 064702 (2011).

66. Chiou, C. H. & Lee, G. B. A micromachined DNA manipulation platform for the stretching and rotation of a single DNA molecule. *Journal of Micromechanics and Microengineering* **15,** 109–117 (2005).
67. Strick, T. R., Allemand, J. F., Bensimon, D. & Croquette, V. Behavior of supercoiled DNA. *Biophys J* **74,** 2016–28 (1998).
68. Brutzer, H., Luzzietti, N., Klaue, D. & Seidel, R. Energetics at the DNA Supercoiling Transition. *Biophys J* **98,** 1267–1276 (2010).
69. Celedon, A., Wirtz, D. & Sun, S. Torsional mechanics of DNA are regulated by small-molecule intercalation. *J Phys Chem B* **114,** 16929–35 (2010).
70. Weiss, S. Fluorescence Spectroscopy of Single Biomolecules. *Science* **283,** 1676–1683 (1999).
71. Hoffman, M. T., Sheung, J. & Selvin, P. R. Fluorescence imaging with one nanometer accuracy: in vitro and in vivo studies of molecular motors. *Methods Mol Biol* **778,** 33–56 (2011).
72. Yildiz, A. *et al.* Myosin V walks hand-over-hand: single fluorophore imaging with 1.5-nm localization. *Science* **300,** 2061–5 (2003).
73. Klar, T. A., Jakobs, S., Dyba, M., Egner, A. & Hell, S. W. Fluorescence microscopy with diffraction resolution barrier broken by stimulated emission. *PNAS* **97,** 8206–8210 (2000).
74. Fernández-Suárez, M. & Ting, A. Y. Fluorescent probes for super-resolution imaging in living cells. *Nat Rev Mol Cell Biol* **9,** 929–943 (2008).
75. Patterson, G., Davidson, M., Manley, S. & Lippincott-Schwartz, J. Superresolution Imaging using Single-Molecule Localization. *Annual Review of Physical Chemistry* **61,** 345–367 (2010).
76. Hess, S. T., Girirajan, T. P. K. & Mason, M. D. Ultra-High Resolution Imaging by Fluorescence Photoactivation Localization Microscopy. *Biophysical Journal* **91,** 4258–4272 (2006).
77. Manley, S. *et al.* High-density mapping of single-molecule trajectories with photoactivated localization microscopy. *Nat Meth* **5,** 155–157 (2008).
78. Rust, M. J., Bates, M. & Zhuang, X. Sub-diffraction-limit imaging by stochastic optical reconstruction microscopy (STORM). *Nat Meth* **3,** 793–796 (2006).

79. Schneckenburger, H. Total internal reflection fluorescence microscopy: technical innovations and novel applications. *Current Opinion in Biotechnology* **16,** 13–18 (2005).
80. Ban, T. *et al.* Direct Observation of Aβ Amyloid Fibril Growth and Inhibition. *Journal of Molecular Biology* **344,** 757–767 (2004).
81. Baksh, M. M., Jaros, M. & Groves, J. T. Detection of molecular interactions at membrane surfaces through colloid phase transitions. *Nature* **427,** 139–141 (2004).
82. Kuhn, J. R. & Pollard, T. D. Real-Time Measurements of Actin Filament Polymerization by Total Internal Reflection Fluorescence Microscopy. *Biophysical Journal* **88,** 1387–1402 (2005).
83. Kaul, N., Soppina, V. & Verhey, K. J. Effects of α-Tubulin K40 Acetylation and Detyrosination on Kinesin-1 Motility in a Purified System. *Biophysical Journal* **106,** 2636–2643 (2014).
84. Bullen, A. Microscopic imaging techniques for drug discovery. *Nat Rev Drug Discov* **7,** 54–67 (2008).
85. Schuler, B. Single-molecule FRET of protein structure and dynamics - a primer. *Journal of Nanobiotechnology* **11,** S2 (2013).
86. Joo, C., Balci, H., Ishitsuka, Y., Buranachai, C. & Ha, T. Advances in single-molecule fluorescence methods for molecular biology. *Annu Rev Biochem* **77,** 51–76 (2008).
87. Schuler, B. & Hofmann, H. Single-molecule spectroscopy of protein folding dynamics-expanding scope and timescales. *Curr. Opin. Struct. Biol.* **23,** 36–47 (2013).
88. Qiu, Y. & Myong, S. Single Molecule Detection of One, Two and Multiplex Proteins Involved in DNA/RNA Transaction. *Cel. Mol. Bioeng.* **4,** 125–137 (2011).
89. Tang, G. Q., Roy, R., Bandwar, R. P., Ha, T. & Patel, S. S. Real-time observation of the transition from transcription initiation to elongation of the RNA polymerase. *Proc Natl Acad Sci* (2009).
90. Chen, C. *et al.* Dynamics of translation by single ribosomes through mRNA secondary structures. *Nat Struct Mol Biol* **20,** 582–588 (2013).
91. Jacobs, M. J. & Blank, K. Joining forces: integrating the mechanical and optical single molecule toolkits. *Chem. Sci.* **5,** 1680–1697 (2014).

92. Hugel, T. *et al*. Experimental Test of Connector Rotation during DNA Packaging into Bacteriophage φ29 Capsids. *PLoS Biol* **5,** e59 (2007).
93. Adachi, K. *et al.* Coupling of Rotation and Catalysis in F1-ATPase Revealed by Single-Molecule Imaging and Manipulation. *Cell* **130,** 309–321 (2007).
94. Shroff, H. *et al.* Biocompatible force sensor with optical readout and dimensions of 6 nm3. *Nano Lett* **5,** 1509–14 (2005).
95. Janssen, X. J. A. *et al.* Electromagnetic Torque Tweezers: A Versatile Approach for Measurement of Single-Molecule Twist and Torque. *Nano Letters* **12,** 3634–3639 (2012).

Chapter 2

DESIGN OF ELECTROMAGNETIC TWEEZERS WITH INDEPENDENT FORCE AND TORQUE CONTROL

In this chapter, I first discuss the considerations required by the design of electromagnetic tweezers, including a brief review of the general issues associated with magnetic tweezers, the fundamental physics of the force and torque that can be generated on a superparamagnetic bead by an external magnetic field, and the way that force and torque can be decoupled. I present a guideline for the design and instrumentation of the tweezers system and itemize the modules and components required for a functional electromagnetic tweezers that are suitable for biophysical studies. Then I describe the implementation of electromagnetic tweezers and its integration into an inverted microscopy system, including simulation of the magnetic field, implementation of the electrical and thermal control systems, and the design of other peripheral modules such as software programs and piezoelectric nanopositioners that are required for biophysical studies. The conclusion and discussion are presented in the context of its application in single-molecule investigations and its potential usage in a variety of prospective experiments.

2.1 Introduction

Magnetic tweezers use either permanent magnets or electromagnets to apply an external magnetic field on magnetically permeable microspheres that contain magnetic nanoparticles to apply forces and torques to them. Electromagnetic tweezers (eMT) are very useful in force and torque applications due to diverse configurations in which they can be implemented. Single pole and dual pole eMT were commonly implemented forms[1-3] and some were capable of generating above 10nN of force[4]. Gosse implemented a multipole eMT capable of applying an upward force while applying a torque in the meantime[5]. Amblard[6] and Pavone[7] developed different forms of octapole instruments to apply torque and limited force. Haber[8] and Huang[9] constructed eMT systems that produce a uniform field gradient to apply constant force.

Superparamagnetic microspheres are usually used in the magnetic trapping experiments to impart forces and torques to biological molecules conjugated to the microspheres. Superparamagnetic microspheres are micron-sized spherical particles that contain very fine iron oxide nanoparticles dispersed in silica or polystyrene matrix, and they can be magnetized when placed in an externally applied magnetic field with no hysteresis. When the magnetic field is applied to a superparamagnetic bead, an induced dipole is generated in the bead. The force (F) imparted to the microsphere is:

$$F = \frac{1}{2}\nabla(\vec{m} \cdot \vec{B}) \,, \tag{2.1}$$

where m is the induced dipole moment of the superparamagnetic microsphere and B is the magnetic flux density applied to the microsphere. Anisotropy, a term used to describe the dependence of the internal energy on the direction of the spontaneous magnetization, exists in the superparamagnetic particles, resulting in easy and hard directions of magnetization of the particles. The total magnetization of a microsphere will prefer to lie along the easy axis. The energetic difference between the easy and hard axes results from two microscopic interactions: the spin–orbit interaction and the long-range dipolar coupling of magnetic moments, giving rise to various forms of anisotropies, including magnetocrystalline anisotropy, shape anisotropy, strain anisotropy and surface anisotropy, all contributing to the overall magnetic anisotropy[10,11]. Due to this anisotropy, the superparamagnetic microspheres behaves like a birefringent particle to which a torque can be applied when the anisotropic axis does not align perfectly with the externally applied magnetic field, but forms an angle in between with the field. The torque generated on the superparamagnetic particle is:

$$\tau = \vec{m}_0 \times \vec{B} \, , \tag{2.2}$$

where $\vec{m}_0$ is a minor component of magnetic moment not aligned with the external field due to anisotropy of the particle, and the direction of $\vec{m}_0$ defines the anisotropy axis (easy axis) of the particle[12].

The difficulty of designing magnetic tweezers for single-molecule experiments where force and torque are both applied and need to be independently controlled lies in the intrinsic relationship of force and torque relative to the magnetic field, described by the two aforementioned equations. With the angle between the magnetic dipole of the microsphere and the external magnetic field fixed, and assuming the angle is small, the force imparted on the superparamagnetic bead is proportional to the gradient of the magnetic field, while the torque imparted on the microsphere is proportional to the magnetic field itself. This basic relationship between the force and torque acting on a superparamagnetic microsphere is the source of a longstanding challenge in developing an electromagnetic tweezer setup that can be used to generate piconewton forces and apply constant torque to micrometer-sized beads at the same time. In the implementation of magnetic tweezers where tens of piconewton of force is desired on a typical superparamagnetic bead often used in magnetic trapping experiments, e.g., MyOne bead (Invitrogen), a magnetic field gradient of ~1000T/m is required. Such a field is very non-uniform and is not suitable for applying a constant torque over a large sample region, since a constant torque requires a uniform, constant magnetic field in the vicinity of the microsphere.

Furthermore, the magnetic field strength in the plane where torque is applied needs to be tuned so that the torsional trap stiffness matches that of the molecule under study. The torque that is imparted on a microsphere can be determined from the shift in the average angle $<\theta - \theta_0>$ deviated from the equilibrium angle of the microsphere when no torque is applied, θ_0, and can be expressed as:

$$\tau = k_\theta < \theta - \theta_0 > , \tag{2.2}$$

in which k_θ is the torsional stiffness of the trap, and k_θ can be calibrated by applying equipartition theorem and observing the average width of the angular Brownian fluctuation:

$$k_\theta = \frac{k_B T}{< \delta\theta^2 >} , \tag{2.3}$$

where k_B is the Boltzmann constant, T is the absolute temperature, and $< \delta\theta^2 >$ is the average variance of angular fluctuation. If the trap stiffness is too compliant, the torque that can be applied is not sufficient to fully probe the torsional response of the molecule; if the trap stiffness is too rigid, the rotational thermal motion may become too small to be measured as well as the angular displacement from the equilibrium angular position of the torque trap, which prevents accurate torque measurements.

Conventional magnetic tweezers have been widely used to apply tensile force and change supercoiling status on nucleic acids. Its simplicity and robustness of the experimental implementation made it a popular tool to study mechanical properties of DNA molecule and dependence of interaction between DNA and DNA binding proteins on the supercoiling status of DNA. They are usually composed of a pair of permanent magnets that can be translated and rotated by positioners, and the magnetic field produced by the permanent magnets is used to apply both force and torque to magnetic beads. The magnetic field tightly constrains the rotation of the bead and the externally controlled rotation of the magnets sets the desired number of applied turns to the molecule of interest conjugated to the magnetic bead, which is usually tethered to the surface of flow cell, or reaction chamber. In this conventional configuration, the magnetic tweezers do not track the rotational motion of the bead, hence do not measure the torque applied to the biomolecule directly[13,14]. This is majorly because in this configuration, the strong magnetic field that is approximately parallel to the sample plane (the plane perpendicular to the axis of rotational motion) in the vicinity of the sample under study results in a very strong trap torsional stiffness that is orders of magnitude greater than most biological molecules. A trap torsional stiffness on the order of $10^5\ \mathrm{pN \cdot nm/rad}$ was observed when 10pN of force is applied to the magnetic bead[15]. The same problem is present in electromagnetic tweezers that generate a similar orientation of magnetic field for both force and torque application[16]. The estimated trap torsional stiffness is estimated to be on the order of $10^4\ \mathrm{pN \cdot nm/rad}$ when approximately 1pN of force is applied to the magnetic bead[17].

To solve the problem of high trap torsional stiffness associated with the conventional magnetic tweezers and to apply a field that gives rise to a trap torsional stiffness matching most of the biological molecules, a couple of approaches have been taken to improve the performance of torque measurements. In magnetic torque tweezers, a hollow cylindrical permanent magnet generates an approximately vertically aligned field for force generation, while a small permanent magnet attached to the side of the big cylindrical magnet superimposes a faint angular bias field to constrain the angular orientation of the bead[18]. Such a configuration reduces the trap torsional stiffness to $10^2 \mathrm{pN \cdot nm/rad}$, which is a hundred fold reduction compared to the conventional magnetic tweezers. In the case of electromagnetic tweezers, the rotation motion of the field and its frequency can be modulated by the electric current applied to the solenoid coils. A softer trap torsional stiffness can be created by using a nonlinear coupling regime of a damped rotator system, namely by applying a frequency- and amplitude modulated electric current and rotate the microspheres in the asynchronous regime[17,19]. A similar magnitude of stiffness compared to the magnetic torque tweezers has been achieved.

Electromagnetic tweezers have certain advantages over the magnetic tweezers composed of permanent magnets. Firstly, the magnetic field generated by electromagnetic tweezers can be easily modulated by changing the currents applied to the electromagnetic solenoid coils that compose the tweezers. This voids the necessity of mechanical positioners to manipulate the translational and rotational motion of the magnets, which are required for changing the magnitude and orientation of the magnetic field in the sample region, making electromagnetic tweezers less susceptible to mechanical drift. Secondly, with proper electric circuitries, the current in the solenoid coils can be changed at a time scale much faster than common mechanical positioners, hence the electromagnetic tweezers have the potential to significantly increase the bandwidth of the experiments and introduce various forms of feedback control. Electromagnetic tweezers have been successfully used to generate as large as nanonewtons force on microspheres for probing the mechanical and rheological properties of intracellular environment as well as mechanical responses of biomolecules[20]. Also they have been used to apply rotation motion to magnetic beads in magneto-optical trap in which force on the bead is separately applied by optical tweezers[7].

In the following sections, I will describe the implementation of an electromagnetic tweezers system that is capable of applying force and torque on superparamagnetic beads in a decoupled manner, by using two superimposed field generated by different configuration of electromagnets with distinct geometrical designs.

2.2 Mechanical Design and Implementation of Electromagnetic Tweezers

An electromagnet usually consists of a solenoid with a cylindrical magnetic core. Electromagnetic monopoles, composed of one solenoid to produce a magnetic field gradient along one dimension, were used in biophysical studies to stretch single molecules, where no torque or three dimensional manipulations are required[21–23]. The equation describing the force generated on a magnetic particle by externally applied field (Eq. 2.1) indicates that in order to generate a sufficiently large force, a sufficient large magnetic field gradient is required. This means that for force application, the magnetic core placed in the solenoid needs to serve the function as to concentrate the magnetic field in the vicinity of the sample region to enhance the field gradient in that region. Rods of various ferromagnetic materials are commercially available. They should be machined in a way that the end of the core is able to concentrate the magnetic field and provide the largest possible field gradient in the area of interest. In general, this can be achieved by making the tip of the core sharper, because the magnetic flux density is inversely proportional to the area through which the magnetic flux is guided. This could be understood in the example of a parabolically-shaped pole tip with magnetization M_m. The magnitude of the magnetic field strength B, and its gradient ∇B decays with the distance z from the tip according to the equation as follows[24]:

$$B(z) = \frac{\mu_0 M_m}{4\beta z + 1}, \tag{2.5}$$

$$\nabla B(z) = \frac{4\mu_0 \beta M_m}{(4\beta z+1)^2}, \tag{2.6}$$

where μ_0 is the magnetic permeability in vacuum, $M_m$is the uniform magnetization of the pole material and β is a geometric factor determined by the radius of the tip, i.e., sharpness of the paraboloid. From these relationships, it can be seen that the magnetic field of a sharp tip ($\beta \gg 1$) is highly non-uniform in the region close to the electromagnetic pole ($z \ll 1$). Furthermore, both the strength of the field and its gradient drop when distance z increases, providing a uniform magnetic field in the area far away from the tip, making such area suitable for applying constant torques. Even though the equations only predict the field and field gradient distribution in the vicinity of a parabolic shaped core tip, the general principle that the field decays rapidly with distance applies to the similar geometry of electromagnetic solenoids as well.

We predicted the magnetic field strength (B field) and its gradient (∇B) by conducting simulations in COMSOL Multiphysics (COMSOL Inc.) using its AC/DC module. Figure 2.1 (a) shows the geometry of the solenoid coils and magnetic core. The simulation is conducted by multi-turn coil domain conditions with 200 coil windings and a range of electric current is applied to the coil. The core has a 40mm long cylindrical body and is tapered gradually to a smaller diameter to condense the magnetic field into progressively smaller cross-section area, and its tip assumes a hemispherical shape with radius of 0.25mm. The core material is set as soft iron due to its reasonably large saturation magnetization and easiness for mechanical machining procedures. The simulation result shown in Figure 2.1 (b) demonstrates that the ∇B-distance dependence can be empirically determined by a power law:

$$|\nabla \mathrm{B}| = \frac{\mathrm{A} \cdot \mathrm{I}}{\left(\frac{\mathrm{z}}{\delta} + 1\right)^{\mathrm{p}}} \ , \tag{2.4}$$

where I is the current applied to the solenoid for monopole excitation, and z is the distance from the pole tip, with scaling factor A, distance offset δ, and exponent p being fitting parameters. The fitting parameters are constant for various currents applied to the coil with decaying exponent parameter p=2.68, z offset δ=0.2mm, and scaling factor A=900 T/m. The model prediction is similar to previous results for a related geometry reported by Bijamov and coworkers[23].

The steep gradient in the vicinity of the pole tip, $> \sim 100\mathrm{T/m}$ within several hundred micrometers from the tip, is suitable for generating a high magnetic force on the superparamagnetic microspheres. For example, when 1A of current is applied to the coil of the monopole, the simulation result in Figure 2.1 (b) indicates that at the 0.2mm away from the tip of the metal core, the gradient of the magnetic field is about 250T/m. Considering MyOne beads, a commonly used superparamagnetic bead purchasable from Invitrogen, whose saturation magnetization is $\mathrm{m_{sat}} = 25.92 \times 10^{-15} \mathrm{A \cdot m^2}$ and saturation

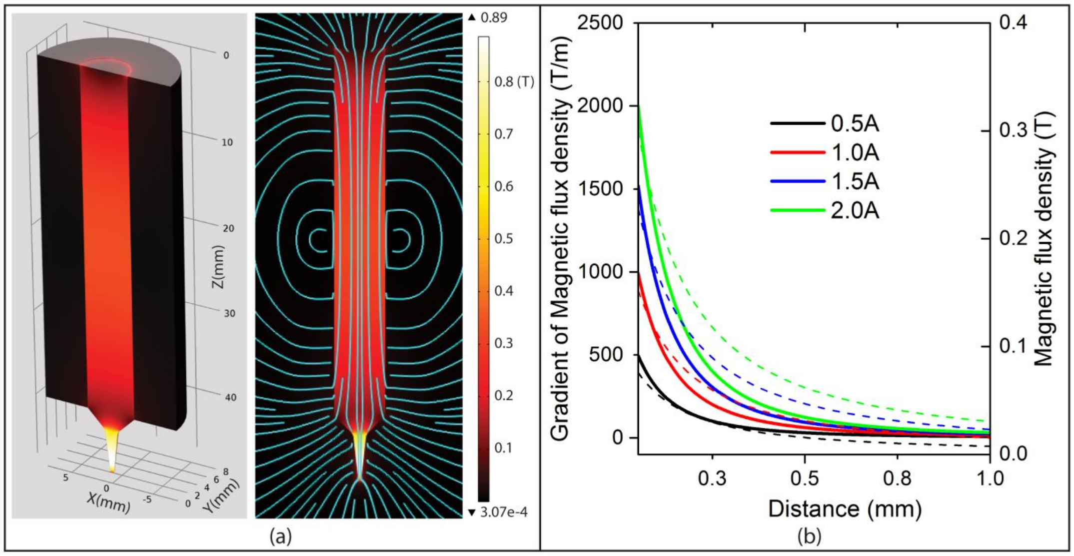

Figure 2.1 Simulation of the distribution of magnetic field strength of a monopole electromagnet. (a) Geometry of the model designed for simulation is color-mapped by magnetic field strength distributed in the magnetic core. The simulation result is visualized when 1.5A of current is applied to the solenoid coil. The color map indicates the magnitude of magnetic field strength. 2D streamline of magnetic flux is plotted under the same simulation condition. (b) The distribution of magnetic flux density (dashed lines) and its gradient (solid lines) inside and outside of the electromagnetic soft iron core when the monopole electromagnetic tweezer is excited by electric current of 0.5, 1.0, 1.5 and 2.0 amperes respectively.

field strength at 12mT[25], the force applied to the bead is ~6pN. Because the magnetization of beads scales roughly with their volume, beads of different sizes can be selected to meet the desired force requirement of a particular experiment. Beads with larger diameter, such as M280 (2.8μm diameter, $\mathrm{m_{sat}} = 160.57 \times 10^{-15}\mathrm{A \cdot m^2}$) and M450 (4.4μm diameter, $\mathrm{m_{sat}} = 1450 \times 10^{-15}\mathrm{A \cdot m^2}$) beads, both commercially available for purchase from Invitrogen, can be used in the applications where higher force is required.

As seen above, the gradient of the magnetic field decays to roughly a constant at distances above several millimeters away from the tip and the field strength becomes a fraction of tenth of the field near the pole tip, which is suitable for producing soft trap

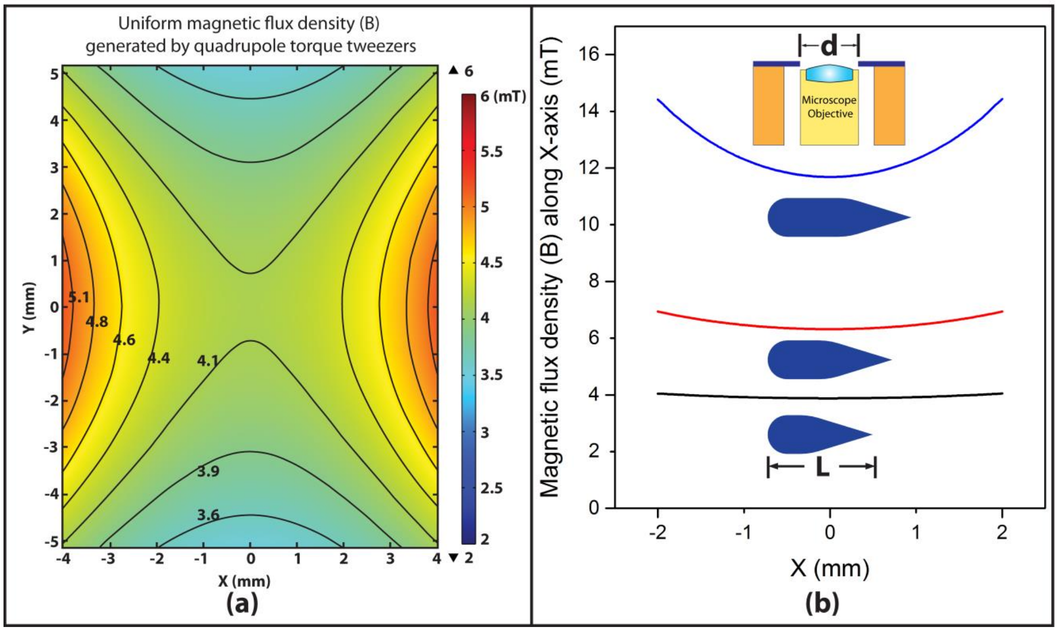

Figure 2.2 Uniform magnetic flux density generated by quadrupole torque tweezers. (a) COMSOL simulation of the magnetic flux density. The distribution of the magnetic flux density created by the quadrupole electromagnetic tweezers when the 1A of current is applied to the two diagonal poles (with tips of length L=16mm). The origin indicates the center of the quadrupole in the vicinity of the sample region, on the optical axis of the microscope. A uniform field is generated in the sample area, ideal for applying a uniform torque. (b) The length of the tip can be varied to change the field strength in the middle area of the quadrupole and can be used to vary the trap torsional stiffness accordingly. Tips with length L=16mm, 19mm, 22mm are used in the simulation. The longer tips that extend closer to the sample region are capable of generating higher magnetic field but this is accompanied by slight increase in the nonuniformity in the field. Tips with the length of 16mm are used in the experiments reported here. The corresponding distances between tip ends of diagonal poles are 20mm, 14mm, 8mm.

stiffness for torque application. We used simulation to predict the magnetic field produced by a pair of dipole with opposite direction of DC current applied to each, one producing an N polarity and the other producing an S polarity. In each pole, the magnetic field is constrained dominantly in the magnetic core within the coil, as shown in the monopole simulation, and is then guided to the sample plane a couple of millimeters above the microscope objective by a piece of thin tip with thickness of 1mm. The geometric configuration for simulation and the design of pole tips are shown in the illustrations in Figure 2.2 (b). As shown in Figure 2.2 (a), the magnetic field in the central area is approximately constant, which results in uniform torques that can be applied to the microspheres over several mm^2 of area. The tips mounted on the magnetic core can be easily replaced and the variation of the length of the tips can fine tune the magnitude of the field, making possible a variation of the trap torsional stiffness.

Following the guideline for force and torque generation provided by the simulation results, the electromagnetic tweezers (eMT) were designed to consist of multiple poles which are operated in different regimes for force and torque generation. The eMT is composed of a monopole for force generation and a set of quadrupoles for torque generation. We use the monopole in the direct vicinity to the trapping region to generate a strong magnetic field gradient and to generate a strong force on the superparamagnetic microspheres located in that region. We use the separate set of quadrupoles whose pole-tips are centimeters away from the sample region to produce a uniform field that is capable of rotation for applying torque on the microspheres. Five electromagnetic poles form a pyramid-like shape, each pole representing a pinnacle of the pyramid, shown in Figure 2.3a. Each of the five electromagnetic poles is composed of a solenoid with a cylindrical metal core. The solenoids are constructed by winding up polyimide insulated copper wire (AWG 19, MWS Wire Industries) by about 200 turns, giving rise to an inductance of ~180μH and a resistance of ~0.15 Ω. The geometry of the poles of the electromagnetic tweezers is designed for adapting into a customized microscope stage. In the setup, the monopole generates, in the vicinity of the sample region, a magnetic field

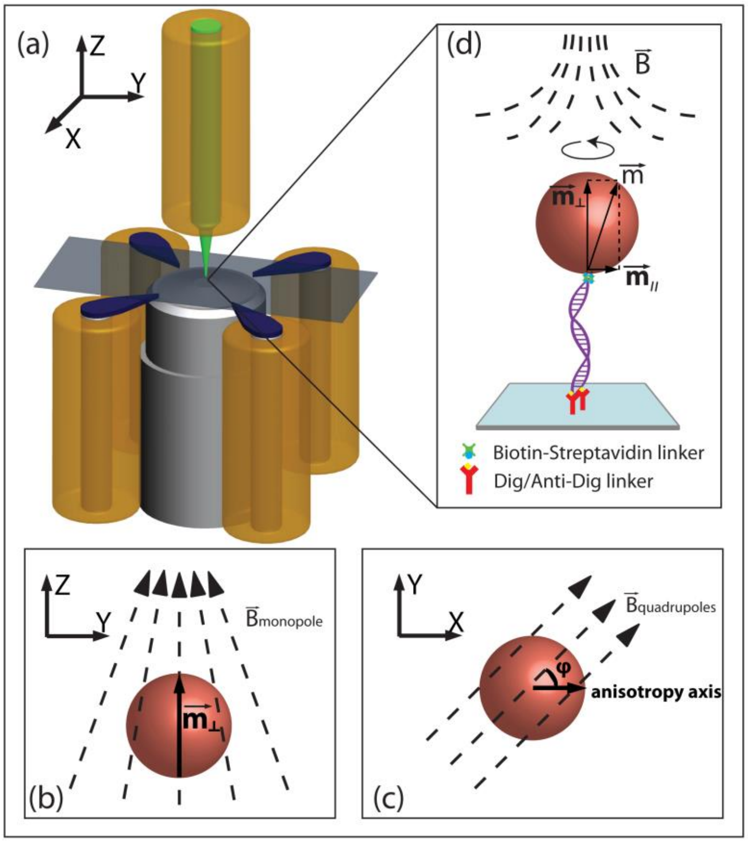

Figure 2.3 Configuration of the electromagnetic tweezers. (a) The electromagnetic tweezers are composed of one monopole placed closely above the sample to generate an upward pulling force on the superparamagnetic microsphere, and a set of quadrupole surrounding the microscope objective for torque generation. (b) The monopole generates a sharp magnetic field gradient and induces a dipole moment $m_\perp$ along z axis. A force is generated on the microsphere in z-direction. (c) The quadrupoles generate a uniform magnetic field in x-y plane. When a torque is applied to the bead, the angular orientation of the bead's anisotropy axis is displaced from the field direction by an angular phase difference φ ($\varphi = \theta - \theta_0$ in Equation 2.3). (d) When both the monopole and quadrupoles are excited by applying current through their solenoid coils, a superimposed field consisting of an approximately vertically aligned field generated by the monopole and a horizontally aligned field generated by the quadrupoles, hence both force and torque can be generated on the microsphere. The schematic illustrates an experiment in which force and torque applied to the microsphere are imparted to a single DNA-molecule.

with a sharp gradient along the microscope's optical axis (z-axis). This field induces a component of the dipole moment $m_\perp$ along z-axis and generates a force on the

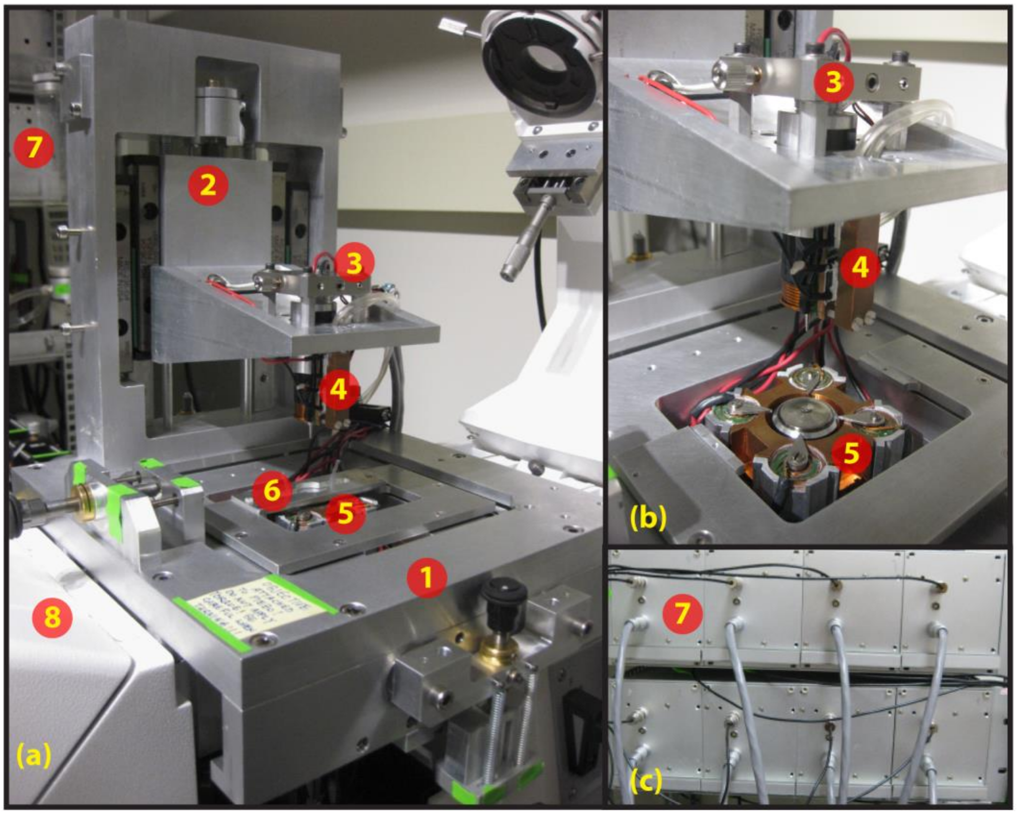

Figure 2.4 Mechanical Design and Implementation of Electromagnetic Tweezers. Electromagnetic tweezers are integrated into a custom modified inverted microscope. (1) Custom designed XY positioning stage with fine-focus minimal-drift control of objective lens. (2) Elevation mechanism for controlling z-position of the monopole. (3) XY positioner of the monopole. (4) Monopole force tweezers of the eMT. (5) Quadrupoles torque tweezers of the eMT. (6) Flow cell fixture. (7) Electronic modules for eMT driver circuits and temperature control system. (8) Zeiss Axiovert inverted microscope.

microsphere. The quadrupole tweezers generate a uniform magnetic field in x-y plane and induces a dipole moment $m_{\|}$ in the same plane, at the meantime, when there is no torque applied to the bead, the anisotropy axis tends to align with the external field. When a torque is applied to the bead, the direction of the anisotropy axis is displaced to form an angle with the external field. The torque generated by this misalignment between the anisotropy axis and the direction of the external field is described by Equation 2.2. When both the monopole and quadrupoles are activated simultaneously by the currents applied through their solenoid coils, a superimposed field is produced in the sample region, consisting of an approximately vertically aligned field generated by the monopole, and a horizontally aligned field generated by the quadrupoles, thus both force and torque can be generated on the microsphere.

The eMT is integrated into the optical system of an epi-fluorescence inverted microscope (Figure 2.4). Custom designed cross-roller bearing stage with fine objective focusing mechanism is mounted on the microscope for adjusting the XY position of the sample chamber, or flow cell, which is stably held in position by flow cell fixture. The monopole is mounted on a linear roller bearing positioning stage that allows Z-direction motion and the Z-position is fine adjusted by a high-precision adjustment screw (AJS100-02H, Newport). The XY position of the monopole can be fine adjusted by a flexure translation mount (CP1XY, Thorlabs).

2.3 Design of Electric System for Driving Eletromagnetic Tweezers

A voltage-to-current converter amplifier is needed for each of the poles to drive current through solenoid coils. The voltage input to each amplifier is commanded by computer through FPGA multifunction RIO board cards (PCI-7833R, National Instruments) and controlled by custom Labview programs. Each amplifier outputs a current through solenoid coils that is proportional to the command voltage input. A high-bandwidth amplifier has advantages, including potential implementation of high-bandwidth feedback control in force and torque generation that allows expanding the range of experiments for which this eMT can be used. In addition, it will be possible to remove remnant magnetization of the metal cores and tips of the poles rapidly, thus minimize the hysteresis of the magnetic field and reduce the remnant force and torque in the eMT. However, due to the high inductance of the coils, a high-bandwidth amplifier requires higher driving energy since the voltage across the inductor increases proportionately to the frequency of the current applied to the inductor, assuming the amplitude of the current maintains the same.

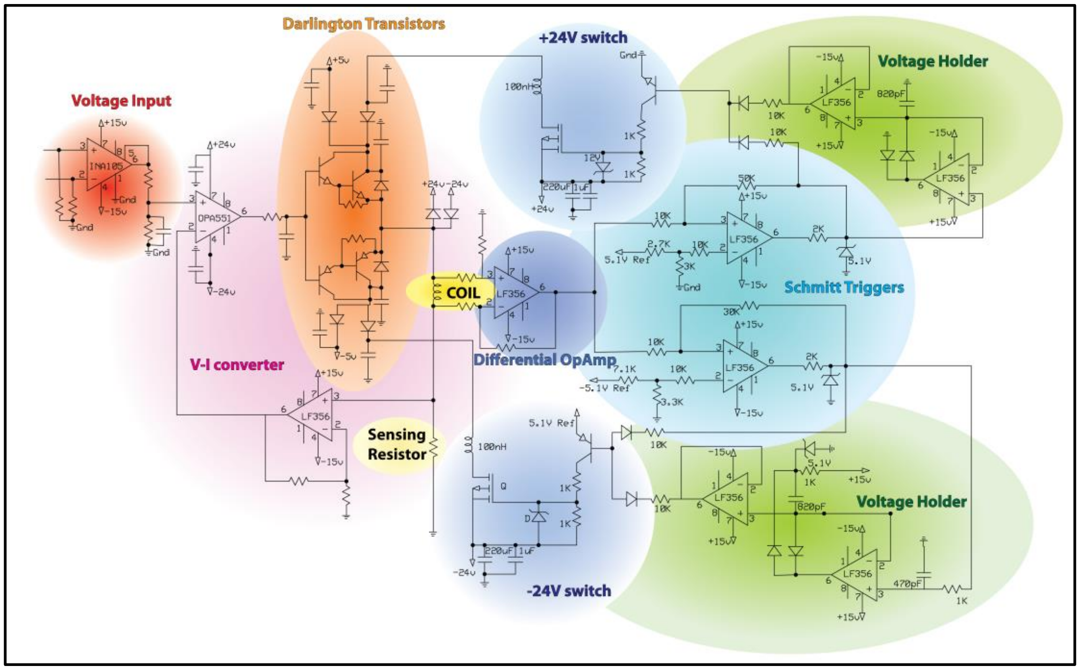

Figure 2.5 Circuit diagram illustration of the voltage-to-current converter. The circuit illustration shows the main components of the voltage-to-current drivers for the solenoid coils. The circuit is composed mainly of an instrumentation operational amplifier (op-amp) receiving a command voltage from a computer and then the voltage-to-current converter module delivers a current to the coil that is proportionate to its voltage input. At low bandwidth domain, ±5V serve as supply voltages to drive the current through the solenoid coil by Darlington transistors. At high frequency domain, the voltage across the coil increases and it is sensed by the differential op-amp. When the voltage exceeds a threshold voltage set by Schmitt triggers, ±24V supply voltage will be activated by the ±24V switching circuits. All supply voltages of op-amps are properly filtered by by-pass capacitors.

The circuit needs to strike a balance between the constant force and torque applications that only require DC and low-bandwidth circuit response, and the potential closed-loop feedback control that requires high-bandwidth circuit response, e.g., in the case of position clamp experiments, and degaussing procedures to remove remnant magnetization of the electromagnetic poles. We implemented a circuit with a mechanism that is capable of automatically sensing the energy needs of driving current through

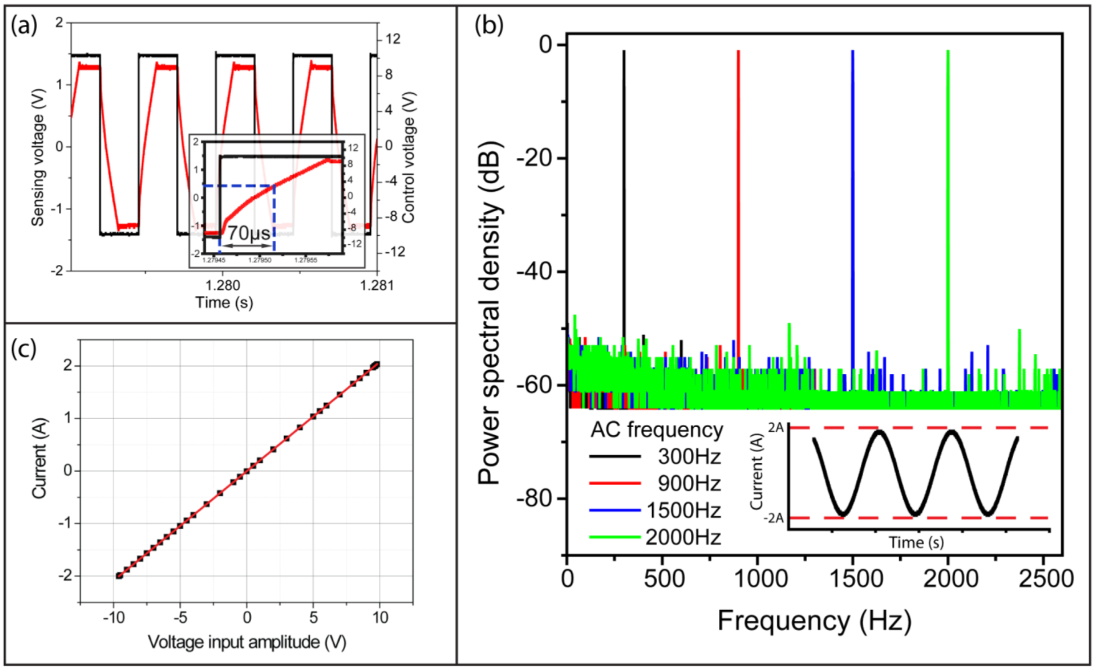

Figure 2.6 Characterization of the voltage-to-current converter. (a) The voltage signals are converted to current signals by voltage-current converter amplifiers. The step response of the transconductance amplifier simulated by large signal square waves demonstrates that the bandwidth of the circuit for feedback control can reach up to about 3kHz, with an inductive load of up to 800μH. (b) The power spectral density (PSD) analysis of the transconductance current output when 300Hz, 900Hz, 1500Hz and 2000Hz sinusoidal electric current with amplitude of 2 Amp is applied to the solenoid coils. (c) Calibration of the voltage-current converter shows the output of electrical current applied to solenoids of the electromagnetic tweezers increases linearly with input command voltage sent to transconductance amplifier from computer. The sign of the current value indicates the polarity of the magnetic pole.

solenoid coils at different frequency domains, by monitoring the voltage across the coil by a differential amplifier. At low-bandwidth or DC mode, where the voltage across the coil is low due to the low resistance of the coil, ±5V power supplies are used as energy source to deliver the current through the coil by Darlington transistors. At high-frequency mode, the voltage across the coil increases due to the high inductance of the coils. When the voltage exceeds a preset threshold voltage programmed into the Schmitt trigger, the ±24V switching circuit modules are activated and the current driven through coils are supplied by ±24V power supplies. The amplifier is capable of reaching up to about 3kHz, with an inductive load of up to 800μH, for large signal response (Figure 2.6a). The power spectral density (PSD) analysis of the amplifier when 2A of current is applied to the solenoid coils at various frequencies demonstrates low harmonic distortion (Figure 2.6b). The amplifier transconductance measurement shows great linearity of the output current applied to solenoid coils with regard to the input command voltage sent to voltage-to-current converters from the computer (Figure 2.6c).

2.4 Design of Temperature Control System

Temperature control of the electromagnetic coils is crucial for stable experimental observations. For high-precision experiments that require nanometer resolution and stability, Joule heating of the copper wires of the solenoids will introduce thermal expansion and drift to the mechanical components, causing uncertainty and inaccuracy to experiment results. Heating can also cause temperature variation in the sample chamber, resulting in the changes of reaction conditions as well as potential thermal damage to the biological reagents and biopolymers under study. It is especially worth noting that the force generated by the monopole is sensitive to the distance between the sample and the

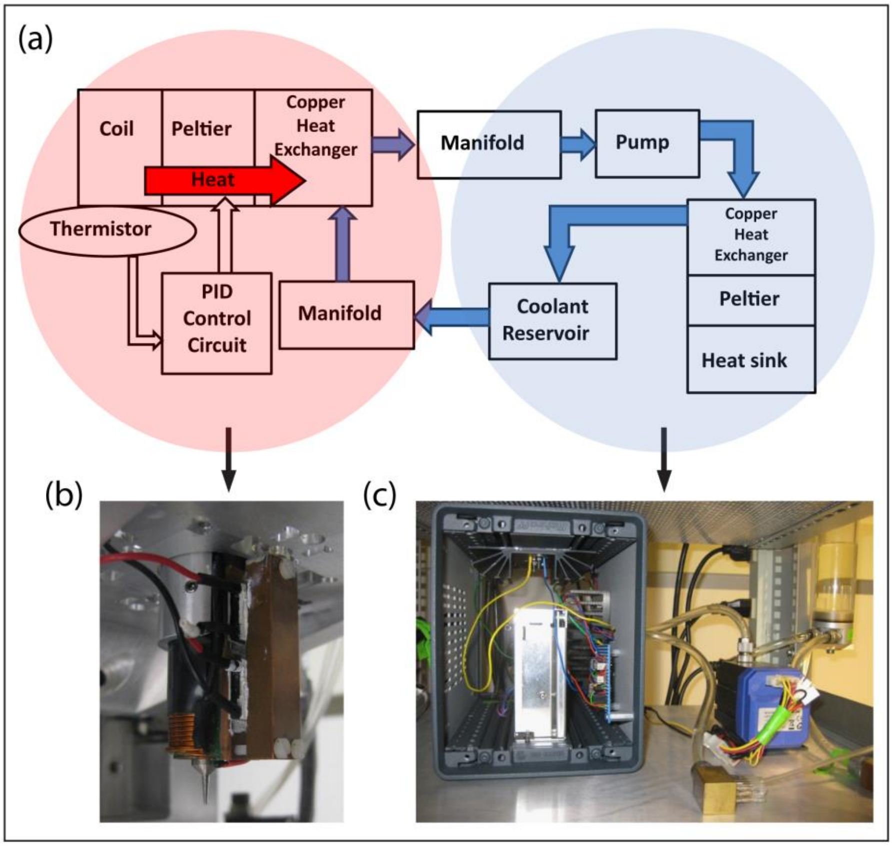

Figure 2.7 Design and implementation of the cooling system for temperature control. (a) Block diagram of active heat dissipation system consisting of Peltier thermo-electric cooling devices that are placed in the proximity of the coils. The temperature of coils are sensed by thermistors which in turn convert the temperature signal into an electric signal for an analog PID temperature control circuit for actively and precisely maintaining the eMT at a desired temperature. This active cooling method avoids thermal drift caused by heat produced by the coils during experiments. (b) and (c) show the implementation of the cooling system. Copper blocks serving as heat exchange units with coolant flowing through are attached to the thermos-electric cooling devices, which in turn are placed in the vicinity of solenoids. The heat generated in the coils is guided away from the microscope by coolant circulation system and the heat carried in the coolant is further dissipated by a secondary thermos-electric cooling system.

tip of the metal core. The Joule heating in the coil results in the thermal expansion of monopole core and could change the distance between the sample and the monopole tip. Using a temperature coefficient of iron (~10^{-5}ppm/K) to estimate the thermal expansion of a metal core caused by temperature rise in solenoid coils, the metal core of the solenoid elongates by $\sim 10\mu m$ when its temperature is increased by 10K. Without active cooling, we indeed observed that when the monopole is placed in contact at the top of the sample chamber and activated, beads adsorbed to the bottom surface of the flow cell were not stably maintained in focus. We noticed such drift in focus was reversible when the electric

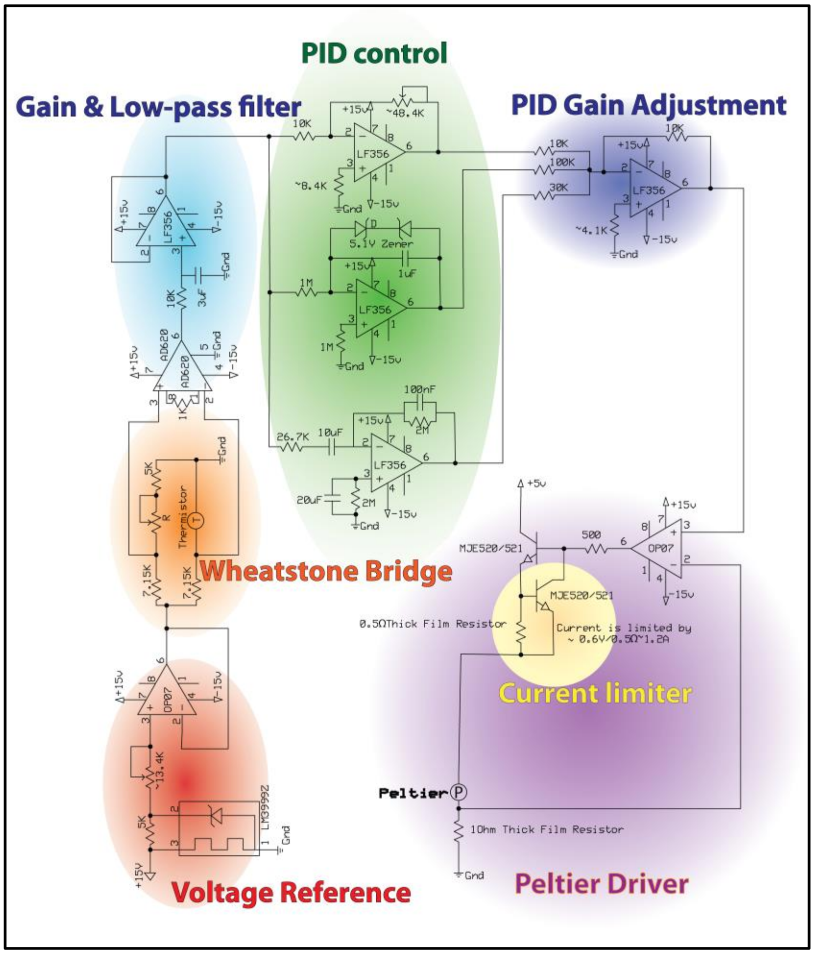

Figure 2.8 Circuit diagram of the PID control module for temperature control. The PID control circuit consists of a Wheatstone bridge that effectively compares the set temperature determined by voltage reference to the temperature measured by the thermistor, which is attached to the solenoid coil. The difference signal is low-passed, amplified and sent into a PID control module. The PID control output signal commands the driver circuit of the Peltiers, the thermoelectric cooling devices placed in the vicinity of solenoid coils of the tweezers, resulting in the active cooling of the coils.

current was switched off in the monopole. It indicates that the monopole was expanding due to elevated temperature from Joule heating.

To solve the heating problem, we use thermoelectric cooling devices to actively remove the heat away from the coil. These devices operate according to the principle of Peltier effect and use the electrical energy for cooling. The thermoelectric cooling devices are controlled by custom made PID control circuitry (Figure 2.8), with the temperature of the coil measured by the thermistor as feedback signal. The heat is transferred to copper heat exchangers (Figure 2.7b) and further carried away from the tweezers by the coolant

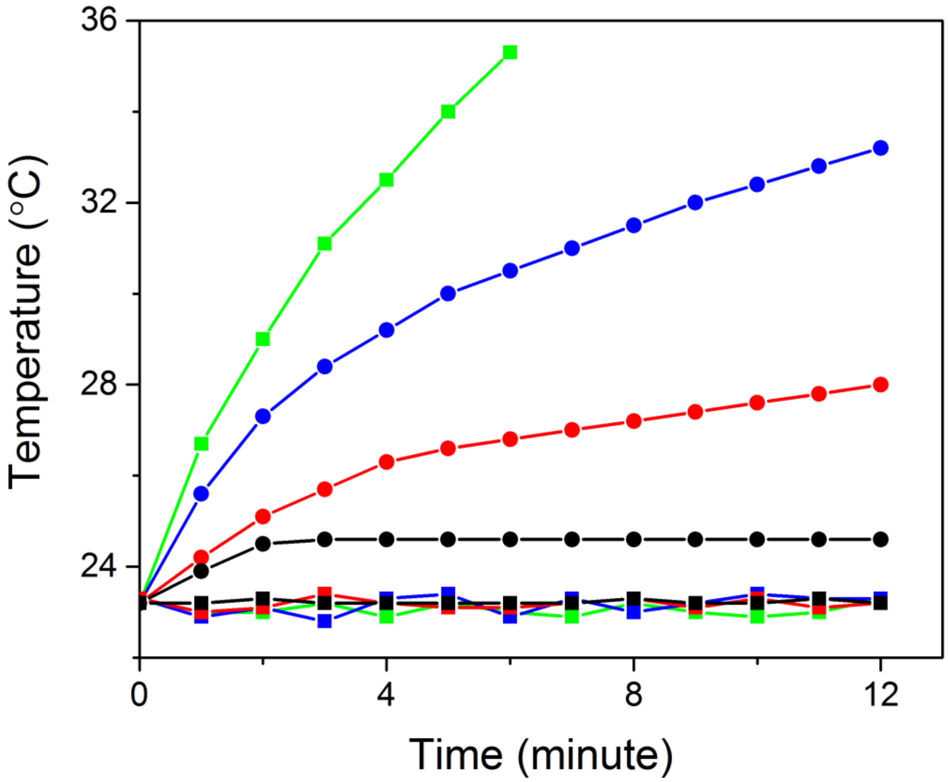

Figure 2.9 Cooling system maintains the constant temperature of the electromagnetic tweezers. When 1A (black), 2A (red), 3A (blue), and 4A (green) of current are applied to the solenoid coils of the tweezers, the temperature increases over time when the cooling system is switched off (circle data points). When the cooling system is switched on, the fluctuation of temperature is maintained within ~0.1K (square data points).

fluid in a cooling system driven by a liquid pump (Figure 2.7c), and the temperature of the coolant is maintained at the set temperature by another similar temperature control loop. The temperature of the tweezers system rises significantly when the cooling system is switched off and electric current of intermediate magnitude is applied to the coil. The temperature rises by more than 10K within 5 minutes when 4A of current is applied to the coil. Such tremendous increase of temperature is almost eliminated and the temperature of the system is maintained to ~0.1℃ when the active cooling is at work (Figure 4b). This significantly improves the thermal stability of the tweezers system, which is indicated by the observation that beads adsorbed to the bottom of surface are maintained in focus when the monopole is placed in contact at the top of the sample chamber and activated.

2.5 Design of Microscope Objective Positioner

Three-dimensional (3D) particle tracking has become a common tool in diverse scientific disciplines ranging from microbiology, biophysical studies to colloidal science and fluid mechanics. The capability of accurate focusing of the microscope objective by a known distance is essential for an array of technologies including confocal imaging, stochastic optical reconstruction microscopy (STORM) and photoactivated localization (PALM) imaging[26–31]. The relative displacement between the focus plane of the objective lens and the sample plane under study is usually achieved by either using piezoelectric stage with z-positioning function to introduce a shift of sample in z-direction, or using an objective focusing elements that change the z-position of the microscope objective. Commercially available 3D piezoelectric stage positioners are usually very costly; meanwhile the objective focusing elements usually occupy a space larger than the microscope objective and reduce the lateral movement range of the sample. To accommodate the compact design requirements of implementing a z-positioning mechanism to shift the focus plane of the microscope objective, we use a ring stack piezo device to actuate the z-positon shift (Figure 2.10). Strain gauges are adhered to the outside cylindrical surface of the ring stack piezo device to sense the axial elongation when the device is actuated. Adapters are designed for the piezo device and fixated to the device by epoxy adhesive. To one end, a matching adapter upon which the microscope objective can be mounted is attached, and to the other end, the whole assembly is screwed to a custom-designed objective focusing mechanism for long-range coarse adjustment.

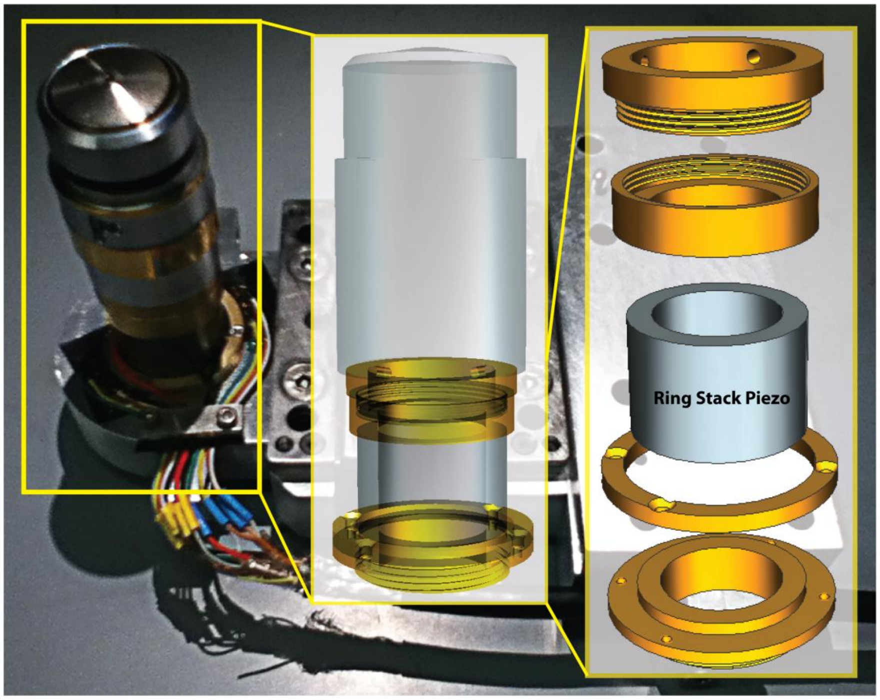

Figure 2.10 Microscope objective focusing mechanism and assembly. The core of a microscope objective is fixated to an adapter. The matching adapters are adhered to a ring stack piezo by epoxy adhesive. Strain gauges are adhered to the outside cylindrical surface of the ring stack piezo device to sense the axial elongation when the device is actuated.

A variety of methods have been developed to track the z-position, the displacement along optical axis of the microscope objective, for example, multiplane imagining, methods that simultaneously image multiple z-slices[32,33]. They are potentially powerful for imaging particles of nanometer size whose defocused image is difficult to acquire and analyze due to the small amount of emitted light they can provide. For larger sized particles, ranging from the size comparable to the diffraction limit of the visible light, a couple of hundred nanometers, to micron-sized objects, their defocused images are a convenient way to determine their 3D position[34,35]. When a particle is not in the focal plane of the imaging optical system, spherical aberrations and diffraction give rise to formation of ring patterns surrounding the particle[16,35–38]. The radius of the rings in the defocused image can be used to decide the z-position of the particle (Figure 2.11). When using fluorescence microscopy, the ring pattern of the particle is particularly convenient for tracking z-position, because the radius of the outermost ring can be easily determined by fitting the intensity profile of the out-of-focus image to an equation representing a Gaussian peak surrounded by a ring with radius R_0:

$$I = A \cdot \exp[-B((x-x_0)^2+(y-y_0)^2)] + C \cdot \exp\left[-D(\sqrt{(x-x_0)^2+(y-y_0)^2} - R_0)^2\right] + \mathrm{E} \ , \qquad (2.8)$$

where A, B, C, D, E, R_0 are all fitting parameters. In this method, the necessity of creating a lookup table as required when using parallel light illumination is avoided. The radius of the ring as a function the distance between the microsphere and the focal plane of the objective is fitted to a polynomial function of third-order. When the distance displacement is restricted to several micrometers, the local fitting function can be approximated by a linear function.

In single-molecule tethered particle experiments, where a micron-sized bead is usually attached to the molecule under study as a force probe, this method is convenient

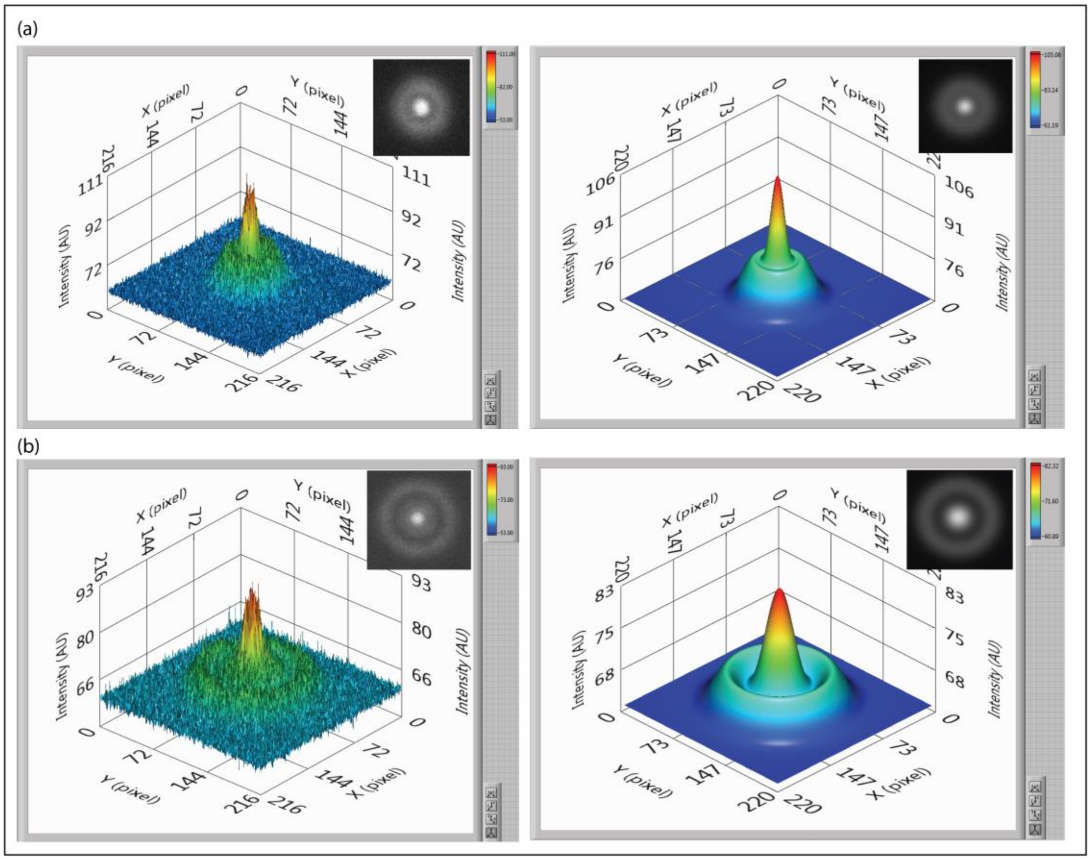

Figure 2.11 Z-position tracking of fluorescent microspheres. When a fluorescent particle is out of the focal plane of the imaging optics, spherical aberrations and diffraction give rise to formation of ring patterns around the fluorescent particle. The radius of the rings increases with the distance between the particle and the focal plane of the imagining optical system. The image of the diffraction ring patterns can be fitted to a Gaussian peak function surrounded by a ring. (a) and (b) are examples of the acquired raw images (left) of a particle at different distance from the focal plane and their intensity profile after fitting process.

and yields accurate results. However, this method of tracking the z-position of fluorescent particles is only feasible for isotropic emitters and spherical micron-sized particles. Also with high numerical aperture oil immersion objectives, the change of radius in the under-focused images, where the focal plane of the objective is below the sample plane, is not symmetric with regard to the over-focused images, where the focal plane of the objective is above the sample plane, and is prone to serious spherical aberrations.

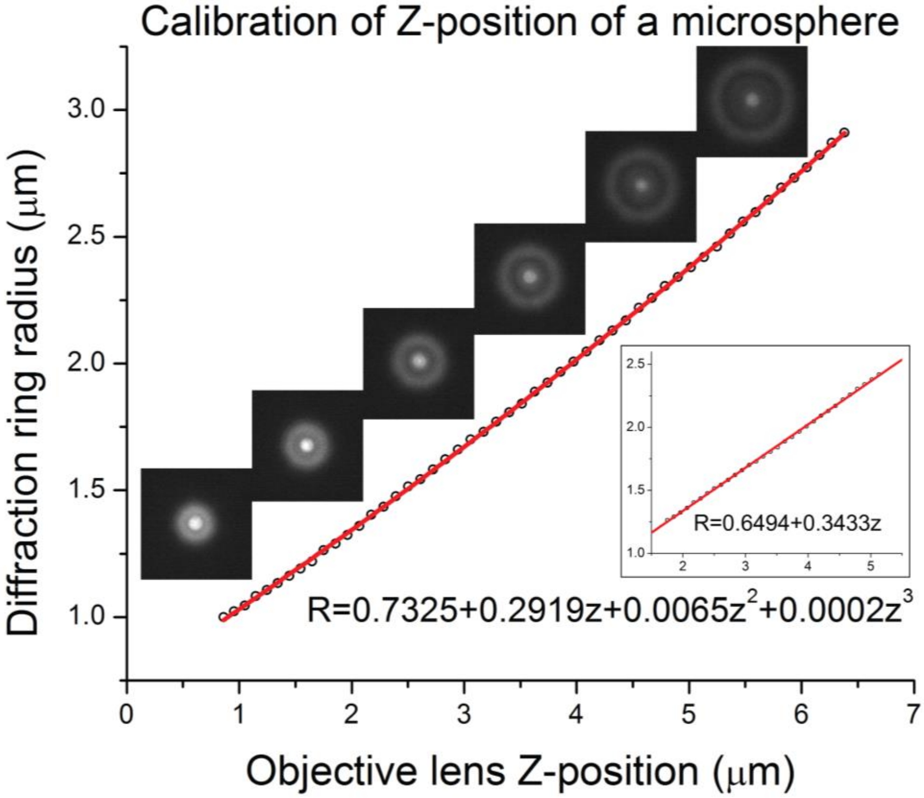

Figure 2.12 Z-position calibration of a fluorescent microsphere. A microsphere adsorbed to the bottom surface of the flow cell is placed slightly below the focal place of the microscope objective, and then the focal plane of the microscope objective is increasing shifted upward away from the microsphere using the piezoelectric focusing device. The radius of the ring pattern surrounding the centroid of the microsphere increases with the distance between the microsphere and the focal plane of the objective. The relationship between the radius of the ring caused by spherical aberration and diffraction is fitted to a polynomial function. Inset shows a linear approximation within a short distance displacement of several micrometers.

2.6 Conclusions

In summary, we designed a novel electromagnetic tweezers (eMT) system that is capable of independently generating a magnetic field with high gradient in the vicinity of the sample region, that is suitable for force application, and generating a uniform weak biasing magnetic field parallel to the sample plane, that is suitable for torque generation. The design was guided by simulation results of magnetic field distribution generated by solenoid coils with magnetic cores. The eMT was integrated into a microscope-based particle tracking system. The eMT features high-bandwidth control of the electric current applied to the solenoid coils, reaching above 3kHz at 800uH inductive load. It also achieved stable temperature maintenance by actively removing the heat generated by the current away from the experimental region, by utilizing an active PID-controlled cooling system, to prevent thermal drift of the mechanical components of the device and avoid temperature variance inflicted to biological samples. We also integrated a custom-designed piezoelectric system for positioning the microscope objective along its optical axis. The system can be used for tracking the vertical position of the fluorescent particles, achieving three-dimensional tracking of nano- and micro-sized particles. The eMT bridges the gap between the existing eMTs that are mainly used for force applications but are not able to generate a uniform field for constant torque application, and those that are capable of generating rotational motions on the magnetic particles but require either permanents magnets or integration of additional optical tweezers for force generation. The eMT is designed to be capable of independently controlling force and torque, allowing us to apply forces at biologically relevant scales, and in the meantime, confine angular orientation of superparamagnetic particles in a trap with low torsional stiffness, making the eMT suitable for torque application and measurement at biologically relevant scales.

2.7 Bibliography

1. Ziemann, F., Rädler, J. & Sackmann, E. Local measurements of viscoelastic moduli of entangled actin networks using an oscillating magnetic bead micro-rheometer. *Biophys. J.* **66,** 2210–2216 (1994).
2. Assi, F., Jenks, R., Yang, J., Love, C. & Prentiss, M. Massively parallel adhesion and reactivity measurements using simple and inexpensive magnetic tweezers. *J. Appl. Phys.* **92,** 5584–5586 (2002).
3. Barbic, M., Mock, J. J., Gray, A. P. & Schultz, S. Scanning probe electromagnetic tweezers. *Appl. Phys. Lett.* **79,** 1897–1899 (2001).
4. Bausch, A. R., Möller, W. & Sackmann, E. Measurement of Local Viscoelasticity and Forces in Living Cells by Magnetic Tweezers. *Biophys J* **76,** 573–579 (1999).
5. Gosse, C. & Croquette, V. Magnetic tweezers: Micromanipulation and force measurement at the molecular level. *Biophys J* **82,** 3314–3329 (2002).
6. Amblard, F., Yurke, B., Pargellis, A. & Leibler, S. A magnetic manipulator for studying local rheology and micromechanical properties of biological systems. *Rev. Sci. Instrum.* **67,** 818–827 (1996).
7. Sacconi, L. *et al.* Three-dimensional magneto-optic trap for micro-object manipulation. *Opt Lett* **26,** 1359–61 (2001).
8. Haber, C. & Wirtz, D. Magnetic tweezers for DNA micromanipulation. *Rev. Sci. Instrum.* **71,** 4561–4570 (2000).
9. Huang, H. *et al.* Three-dimensional cellular deformation analysis with a two-photon magnetic manipulator workstation. *Biophys J* **82,** 2211–23 (2002).
10. Subhankar Bedanta and Wolfgang Kleemann. Supermagnetism. *J. Phys. Appl. Phys.* **42,** 013001 (2009).
11. Bean, C. P. & Livingston, J. D. Superparamagnetism. *J. Appl. Phys.* **30,** S120–S129 (1959).
12. Vilfan, I. D., Lipfert, J., Koster, D. A., Lemay, S. G. & Dekker, N. H. in *Handbook of Single-Molecule Biophysics* 371–395 (Springer New York, 2009).

13. Strick, T. R., Allemand, J. F., Bensimon, D. & Croquette, V. Behavior of supercoiled DNA. *Biophys J* **74,** 2016–28 (1998).
14. Lipfert, J., Koster, D. A., Vilfan, I. D., Hage, S. & Dekker, N. H. Single-molecule magnetic tweezers studies of type IB topoisomerases. *Methods Mol Biol* **582,** 71–89 (2009).
15. Klaue, D. & Seidel, R. Torsional stiffness of single superparamagnetic microspheres in an external magnetic field. *Phys Rev Lett* **102,** 028302 (2009).
16. Gosse, C. & Croquette, V. Magnetic tweezers: Micromanipulation and force measurement at the molecular level. *Biophys J* **82,** 3314–3329 (2002).
17. Mosconi, F., Allemand, J. F. & Croquette, V. Soft magnetic tweezers: A proof of principle. *Rev. Sci. Instrum.* **82,** 034302–034302 (2011).
18. Lipfert, J., Kerssemakers, J. W., Jager, T. & Dekker, N. H. Magnetic torque tweezers: measuring torsional stiffness in DNA and RecA-DNA filaments. *Nat Methods* **7,** 977–80 (2010).
19. Janssen, X. J. A., Schellekens, A. J., van Ommering, K., van Ijzendoorn, L. J. & Prins, M. W. J. Controlled torque on superparamagnetic beads for functional biosensors. *Biosens. Bioelectron.* **24,** 1937–1941 (2009).
20. Fisher, J. K. *et al.* Magnetic force micromanipulation systems for the biological sciences. *Nano* **1,** 191–205 (2006).
21. Liu, R., Garcia-Manyes, S., Sarkar, A., Badilla, C. L. & Fernández, J. M. Mechanical Characterization of Protein L in the Low-Force Regime by Electromagnetic Tweezers/Evanescent Nanometry. *Biophys. J.* **96,** 3810–3821 (2009).
22. Oliver, P. M., Park, J. S. & Vezenov, D. Quantitative high-resolution sensing of DNA hybridization using magnetic tweezers with evanescent illumination. *Nanoscale* **3,** 581–591 (2011).
23. Bijamov, A., Shubitidze, F., Oliver, P. M. & Vezenov, D. V. Quantitative modeling of forces in electromagnetic tweezers. *J. Appl. Phys.* **108,** (2010).
24. De Vries, A. H., Krenn, B. E., van Driel, R. & Kanger, J. S. Micro magnetic tweezers for nanomanipulation inside live cells. *Biophys J* **88,** 2137–44 (2005).

25. Fonnum, G., Johansson, C., Molteberg, A., Mørup, S. & Aksnes, E. Characterisation of Dynabeads® by magnetization measurements and Mössbauer spectroscopy. *J. Magn. Magn. Mater.* **293,** 41–47 (2005).
26. Fernández-Suárez, M. & Ting, A. Y. Fluorescent probes for super-resolution imaging in living cells. *Nat. Rev. Mol. Cell Biol.* **9,** 929–943 (2008).
27. Huang, B., Jones, S. A., Brandenburg, B. & Zhuang, X. Whole-cell 3D STORM reveals interactions between cellular structures with nanometer-scale resolution. *Nat. Methods* **5,** 1047–1052 (2008).
28. Juette, M. F. *et al.* Three-dimensional sub–100 nm resolution fluorescence microscopy of thick samples. *Nat. Methods* **5,** 527–529 (2008).
29. Manley, S. *et al.* High-density mapping of single-molecule trajectories with photoactivated localization microscopy. *Nat. Methods* **5,** 155–157 (2008).
30. Andersson, S. B. & Sun, T. Linear optimal control for tracking a single fluorescent particle in a confocal microscope. *Appl. Phys. B* **94,** 403–409 (2009).
31. Cang, H., Wong, C. M., Xu, C. S., Rizvi, A. H. & Yang, H. Confocal three dimensional tracking of a single nanoparticle with concurrent spectroscopic readouts. *Appl. Phys. Lett.* **88, -** (2006).
32. Prabhat, P., Ram, S., Ward, E. S. & Ober, R. J. Simultaneous imaging of different focal planes in fluorescence microscopy for the study of cellular dynamics in three dimensions. *NanoBioscience IEEE Trans. On* **3,** 237–242 (2004).
33. Sun, Y., McKenna, J. D., Murray, J. M., Ostap, E. M. & Goldman, Y. E. Parallax: High Accuracy Three-Dimensional Single Molecule Tracking Using Split Images. *Nano Lett.* **9,** 2676–2682 (2009).
34. Toprak, E., Balci, H., Blehm, B. H. & Selvin, P. R. Three-Dimensional Particle Tracking via Bifocal Imaging. *Nano Lett.* **7,** 2043–2045 (2007).
35. Wu, M., Roberts, J. & Buckley, M. Three-dimensional fluorescent particle tracking at micron-scale using a single camera. *Exp. Fluids* **38,** 461–465 (2005).
36. Speidel, M., Jonáš, A. & Florin, E.-L. Three-dimensional tracking of fluorescent nanoparticles with subnanometer precision by use of off-focus imaging. *Opt. Lett.* **28,** 69–71 (2003).
37. Hecht, E. *Optics*. (Addison-Wesley, 2002).

38. Lipfert, J., Kerssemakers, J. J. W., Rojer, M. & Dekker, N. H. A method to track rotational motion for use in single-molecule biophysics. *Rev Sci Instrum* **82,** 103707 (2011).

Chapter 3

CHARACTERIZATION OF ELECTROMAGNETIC TWEEZERS WITH INDEPENDENT FORCE AND TORQUE CONTROL

In this chapter, I discuss the characterization of the capability of force and torque generation of the implemented electromagnetic tweezers. I first discuss the range of the forces that can be generated on superparamagnetic microspheres by the force tweezers consisting of a monopole, and the range of the modulation of trap torsional stiffness in the torque tweezers consisting of a set of quadrupoles. Then I describe a novel method for tracking the rotational motion of biomolecules using Janus bead, and its use in single-molecule biophysical studies. I use a DNA-tethered particle system to show that tension in the piconewton force range can be applied to the biomolecule under study and simultaneously the molecule can be twisted with torques in the piconewton-nanometer range. I demonstrate that the two components are independently controlled. At various force levels applied to the Janus bead, the trap torsional stiffness can be changed simply by varying the current magnitude applied to the quadrupole torque tweezers. The discussions and conclusions will be framed to show its use in biomechanical investigations using single molecule force spectroscopy, where the independent force and torque control is required to reveal novel understandings of DNA-protein interactions and DNA conformation dynamics.

3.1 Force Calibration of Monopole

To characterize the capability of force generation of the monopole, the monopole was placed in horizontal position in the vicinity of a capillary (5005-050, Vitrocom) with chamber cross-section of 500µm in width by 50µm in height, and wall-thickness of 50µm. The geometry of the experimental configuration is shown in Figure 3.1(a). Because the bead's velocity was on the order of µm/s, the Reynolds number did not exceed 10^{-5}. In such low Reynolds-number regime, the force calibration techniques for electromagnetic manipulators is commonly based upon Stokes equation where the velocity of magnetic beads pulled through a fluid of known viscosity is used to calculate the applied force[1]:

$$F = 6\pi\eta R v \ , \tag{3.5}$$

where η is the viscosity of the aqueous medium, R is the radius the beads, and v is the instantaneous velocity of the beads. The velocity can be determine by video microscopy[2,3]. When the monopole is excited by electric current, the MyOne beads (Invitrogen) with nominal diameter of 1µm are attracted toward the tip of the pole and their velocity increases when their position draws closer to the pole (Figure 3.1b). The position of the beads was tracked using video microscopy and their transverse velocity was calculated by dividing their displacement between two consecutive image frames by the time interval between the two frames.

The force applied to the beads at particular distances from the tip of the pole was calculated from velocity of the beads using Equation 3.1. Figure 3.1 (c) and (d) shows that force declines with the distance from the tip of monopole and increase linearly with the current. The force decay profile can be fitted to the equation derived from Equation 2.7:

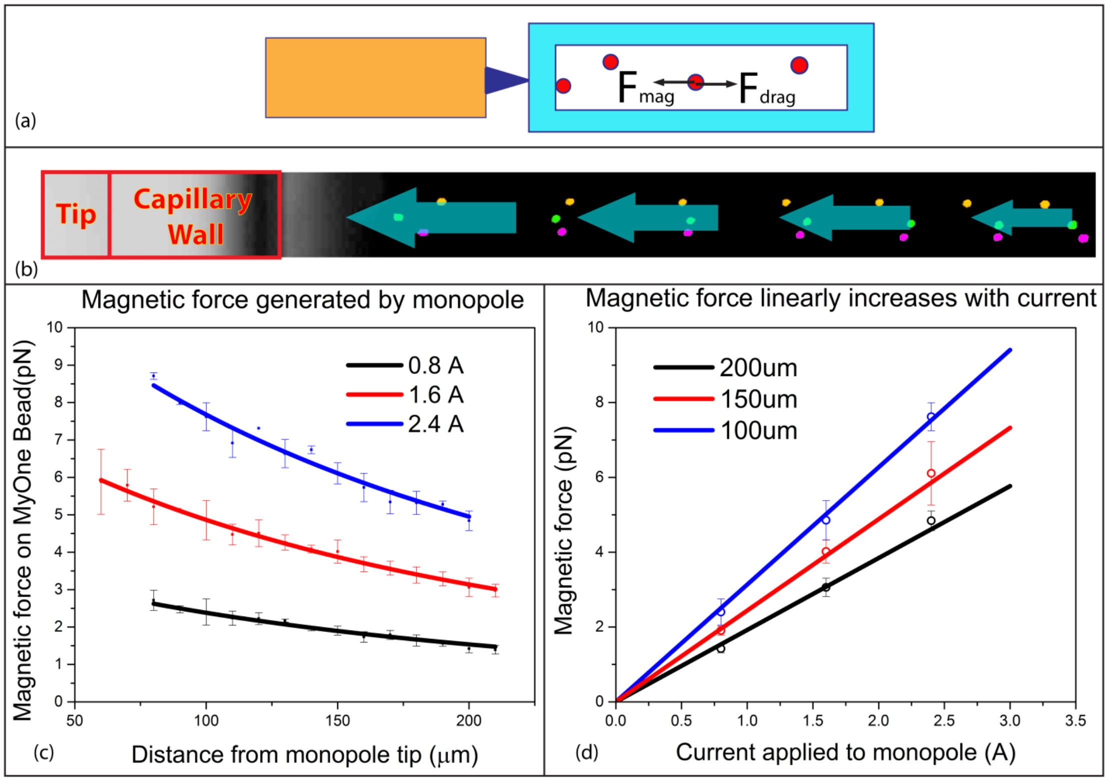

Figure 3.1 Calibration of the force applied to MyOne beads by monopole. (a) The schematic of the calibration of the force generated by force tweezers composed of the monopole. The monopole was placed in horizontal position in the vicinity of a capillary containing MyOne beads dissolves in aqueous solution. The pulling force from the monopole can be determined from the Stoke's drag formula. (b) A sample trace of MyOne beads attracted to the monopole tip by magnetic force. Seven frame excerpts of three beads (colored for clarity) are overlaid to show their positions at different time points. Their velocity increases when they are drawn closer to the tip of the monopole due to steeper field gradient. (c) The force generated by monopole force tweezer on MyOne beads decays with the distance from the end of monopole tip. (d) At a particular distance from the monopole tip, the force increases linearly with the current applied to the solenoid of the monopole.

$$F = \frac{F_0 \cdot I}{\left(\frac{z}{\delta} + 1\right)^p}. \tag{3.2}$$

The value of 2.68 is used for p, as determined in the Equation 2.7, fitting of simulation prediction, as the best fitting parameter for the exponent. With the fixated choice of exponent parameter, the fitting of the data to the equation returns a distance offset $\delta = 0.46\text{mm}$ and force scaling factor $\mathrm{F}_0 = 5.18 \pm 0.19\text{pN}$, with $\chi^2 < 0.01$ for all three curves. When 2.5A is applied to the monopole solenoid, the force generated on MyOne beads at $200\mu\text{m}$ away from the pole tip is about 4pN.

The measured force is nearly 3-fold less than the predicted force from simulation. There are several possible factors that could have contributed to this force estimation and calibration discrepancy. The slight difference in the parameter δ is mostly due to the slight geometric discrepancy of the machined tip compared to the simulated tip since the magnitude of the field strength and its gradient are sensitive to the radius of the tip-end and its smoothness. Such geometric discrepancy in the case of a *de facto* larger radius of the pole tip can cause an overestimation of force generation in the simulation compared to the measured force during calibration. Secondly, due to the geometric configuration of the calibration process, the vertical position of the monopole might have not been aligned perfectly with the capillary and the alignment was not able to be accurately measured from the two-dimensional image. Such misalignment could have resulted in an underestimation of the distance between the monopole tip and the beads' position, leading to an underestimation of the force applied to the bead at a fixed distance from the tip of the monopole. Furthermore, the variance in the magnetization of the beads could make the assumed magnetization value of MyOne beads greater than the actual value of the beads used in the calibration experiment, giving rise to an overestimation of the prediction of the force compared to the experimentally applicable force at a given magnetic field gradient.

Because the magnetization of beads scales roughly with their volume, beads of different sizes can be selected to meet the desired force requirement of a particular experiment. When M270 beads (Invitrogen) are chosen (saturation magnetization $\mathrm{m_{sat}} = 3.6 \times 10^{-13}\mathrm{A \cdot m^2}$)[4], an estimated 60pN of force can be generated under the same condition. Due to the standard deviation in the magnetization among the population of beads, ranging from ~30% to as large as ~70% for M280 beads according to previously reported studies[5,6], to achieve high accuracy in single molecule force spectroscopy measurements, calibration needs to be carried out on individual beads.

3.2 Calibration of Trap Torsional Stiffness

To calibrate the trap torsional stiffness of the quadrupole torque tweezers, we constrained the angular fluctuation of a pair of doublet formed by M270 beads (Invitrogen). We used bead doublet because the dipole moment of the two beads align with the magnetic field generated by the quadrupole and the rotation of the doublet is majorly confined in the xy-plane (sample plane). To avoid the random diffusion of the doublet outside of the field of view of the microscope over time, the doublet pair is tethered to the bottom of the sample chamber by a DNA molecule to constrain its translational displacement in the sample plane. The beads illuminated by parallel light source serve as spherical lenses, focusing the collimated light to a point below each bead, which appears as a bright spot in the image plane. These bright spots can be used to precisely track the lateral position of the beads. The tracking algorithm follows the previously described method[7] and was implemented in MATLAB (Mathworks). Briefly, as shown in upper panel of Figure 3.2, the bright field images acquired by CCD camera were normalized and the median of the global pixel values was subtracted to enhance the intensity peaks in the images. The local maxima were then found by greyscale dilation followed by selecting the pixels whose value does not change by the dilation[8]. Lastly, each local maximum was fitted to a 2D Gaussian function and its peak was used to determine the position of the bead centroid[9]:

$$I = A \cdot \exp\left[-\frac{(x-x_0)^2 + (y-y_0)^2}{B}\right] + C\,, \tag{3.2}$$

where (x_0, y_0) is the coordinate of the center of the emitter, and A, B and C are fitting parameters. The angular variance of the fluctuation decreases when trap stiffness increases and the trap stiffness can be calculated by Equation (2.4).

We show the dependence of the magnitude of angular fluctuation on the electric current applied to the quadrupole torque tweezers. The trap stiffness increases linearly with the current applied to the quadrupoles. When increasing the current applied through one diagonal pair of quadrupole from 0.1A to 0.4A, the trap torsional stiffness increases from tens to hundreds $\mathrm{pN\mu m/rad}$. The torsional stiffness k_{rot} of the system constructed by a superparamagnetic bead and external field can also be expressed by the equation (See Appendix in Ref 10):

$$k_{rot} = \frac{NVCBM}{C + BM}, \tag{3.3}$$

where N is the number of ferrite nanoparticles inside the bead, V is the nanoparticle volume, C is the crystalline anisotropy constant, M is the magnetization of the nanoparticles and B is the external magnetic field strength. Because the anisotropy and the magnetization of the bead is dependent on the volume of the bead, for MyOne beads, the trap stiffness is estimated to be tens of times weaker since they have smaller diameter. Such 10^0-10^2 $\mathrm{pN\mu m/rad}$ magnitude of torsional stiffness matches the torsional rigidity of some protein complexes[11] and cytoskeleton filaments[12,13]. When the monopole is switched on to apply force, the trap stiffness is expected to be further reduced by an order of

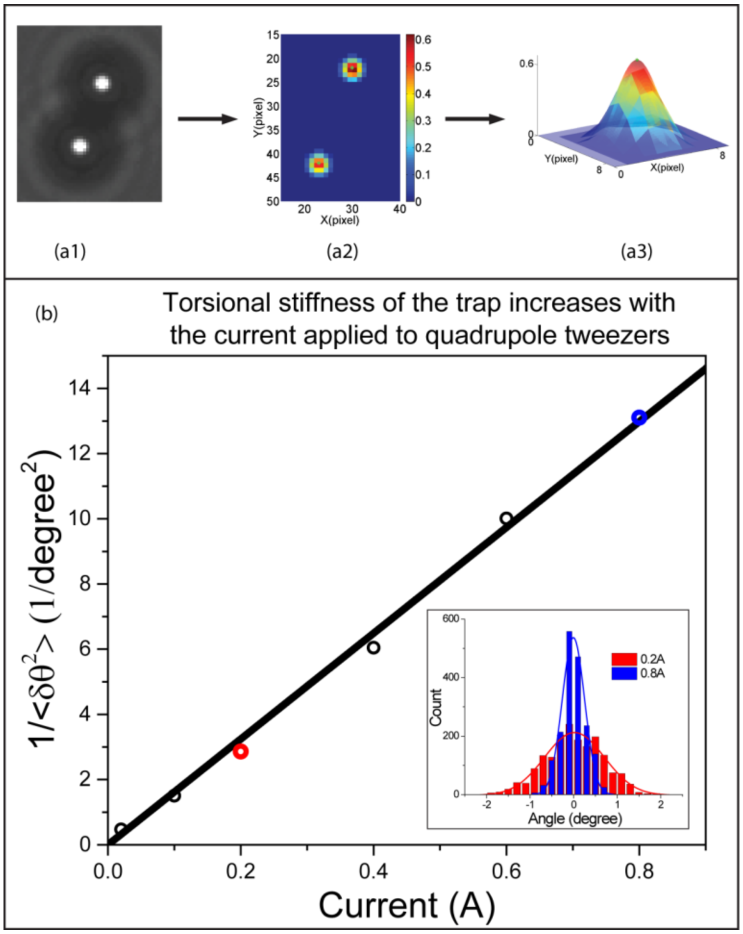

Figure 3.2 Characterization of the torsional stiffness of the quadrupole tweezers with a bead-doublet. The characterization is conducted by constraining the angular orientation of a pair of doublet of M270 beads. From the intensity profile of the bright-field images (a1), the centroid position of each bead forming the doublet is located by finding the local maxima of the image (a2). The localization of each center of the bead is refined by fitting to a Gaussian function (a3). (b)The angular fluctuation of a pair of M270 bead-doublet is measured to calculate torsional stiffness parameter of the quadrupole tweezers. The angular variance is calculate from the histogram of the angular trace of the fluctuation (inset). The inverse of the variance of angular diffusion, proportional to the trap stiffness, increases linearly with the current applied to the quadrupole torque tweezers.

magnitude, because the dipole moment is dominantly aligned to the vertical magnetic field generated by the monopole, resulting in a small component of dipole moment in xy-plane. Hence a trap torsional stiffness of 10-10^3 pNnm/rad, which matches the torsional stiffness of double-stranded DNA molecules[14] and some proteins[15,16], can still be reached even when a piconewton upward pulling force is required in the experiment.

3.3 Using Janus Bead to Track Rotational Motion

Rotational tracking is useful for the study of rotary motion in biological processes, e.g., molecular motion that results in DNA over- or under-winding, and rotational motion of ATP synthase and flagella of bacteria. A variety of methods have been used to detect the rotational motion. Some entail attaching fiducial non-magnetic beads to magnetic particles through low-efficiency bioconjugation[11,17,18], and some require more sophisticated nanofabrication processes for introducing asymmetry, such as in the case of nanorods[19]. A differential interference contrast (DIC) microscopy-based method was developed to detect the angular orientation of gold nanorods with size of ~25nm in width by ~75nm in length, but this method is difficult to implement with force and torque spectroscopy[20]. Furthermore, the methods that are based on bright-field microscopy and DIC microscopy can potentially interfere with the detection of labeled nucleic acids and proteins that usually rely on fluorescent microscopy. We used asymmetrically coated, fluorescent beads to facilitate tracking the angular orientation of the molecule. Such beads are frequently referred to as Janus beads, named after the double-faced Roman god, because when a partial, metallic coating is applied to one side of the fluorescent beads, half of the bead is covered by metal, while the other half maintains the original polystyrene or silica surface that is usually activated by chemical moieties for further bioconjugation. Janus bead has been used as efficient and unique optical probes to study biological interactions or conduct rheological measurements in confined space[21]. Kopelman’s group used the blinking on-and-off property of this type of optical nanoprobes that emit fluorescence anisotropically, dependent on magnetic modulation, to characterize the viscoelastic properties or microenvironments[22–26]. The frequency of the flickering of the particles is related to their rotational diffusion, which is dependent on the viscous drag that the particles experience. Such strategy can potentially be used to create devices ranging from precise nanoviscosimeters to nanothermometers. Choi and coworker used Janus particles as chemical nanosensors to study chemical attraction and biochemical forces by the incorporation of highly selective receptor sites or magnetic coatings on one side of the particles[27]. However, using Janus particle to study the rotational motion of biomolecules has not been explored.

We fabricated our Janus beads by depositing a thin layer (~50nm) of aluminum on to half of the bead surface of 2μm diameter fluorescent superparamagnetic microspheres (Spherotech Inc.) using physical vapor deposition (PVD)[28]. We purchased carboxylated microspheres as these moieties on the bead surface can be readily activated for further bioconjugation. When observed under fluorescent microscope, the emitted light from the uncoated part of the Janus bead can be collected by the microscope objective, while that from the coated half is blocked by the metal coating, giving an appearance of the shape of a crescent moon. To track the angular orientation of a Janus bead rotating around the z-axis, we approximate the fluorescent crescent of the bead as an ellipse and track either its major or its minor axis. When a Janus bead rotates, the angular displacement of the major axis of the ellipse is tracked to determine the rotation angle of the crescent, thus the angular orientation of the Janus bead is inferred (Figure 3.4 inset). The angular orientation of the major and minor axes of the ellipse can be determined by fitting the acquired image of the crescent to an asymmetric 2D Gaussian function:

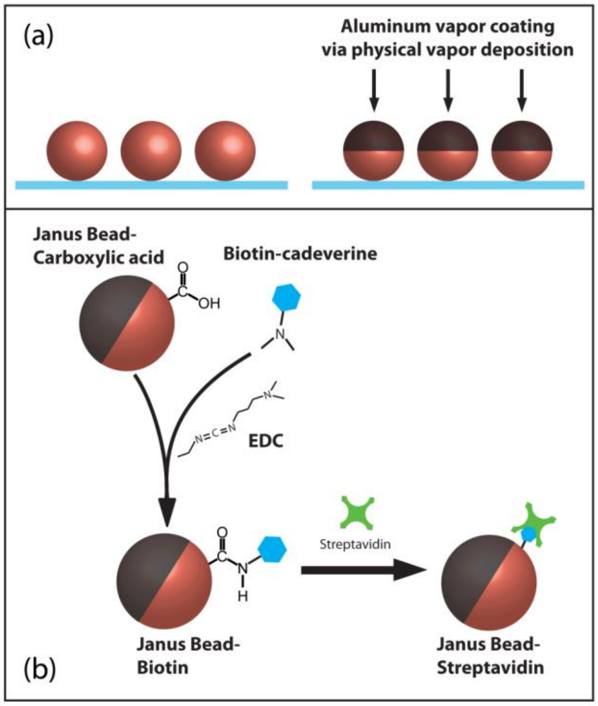

Figure 3.3 Fabrication and functionalization of Janus beads. (a) Fabrication of Janus beads. The Janus bead was fabricated by depositing a thin layer (~50nm) of aluminum on to half of the bead surface of 2μm diameter fluorescent superparamagnetic microspheres whose surface was activated by carboxyl-moities. (b) Functionalization of Janus bead by streptavidin. The carboxylic acid moieties on the uncoated surface are conjugated to biotin-cadeverine using carbodiimide compounds, EDC. Biotinylated Janus bead is further functionalized by streptavidin through biotin-streptavidin bioconjugation.

$$I = A \cdot \exp\left\{-\left[\frac{(x-x_0)\cos\theta-(y-y_0)\sin\theta}{B}\right]^2-\left[\frac{(x-x_0)\sin\theta+(y-y_0)\cos\theta}{C}\right]^2\right\}+D, \quad (3.4)$$

where fitting parameter A is the amplitude of the Gaussian distribution, B and C are width of the major and minor axes of the ellipse, D is the background offset of the image, and θ is the angular orientation of the fitted ellipse. The fitting algorithm was implemented in Labivew (National Instruments) by using Levenberg-Marquardt method.

To verify the angular tracking routine, we pulled and rotated a DNA-tethered Janus bead in the electromagnetic tweezers by using monopole force tweezers to apply an upward pulling force and using quadrupole torque tweezers to generating a rotating magnetic field. The DNA molecules that are labeled on one end by biotin moieties and on the other end by digoxigenin moieties were constructed by molecular cloning methods similar to previously described[29]. Briefly, 8kilo-base pair double-stranded DNA molecules (contour length

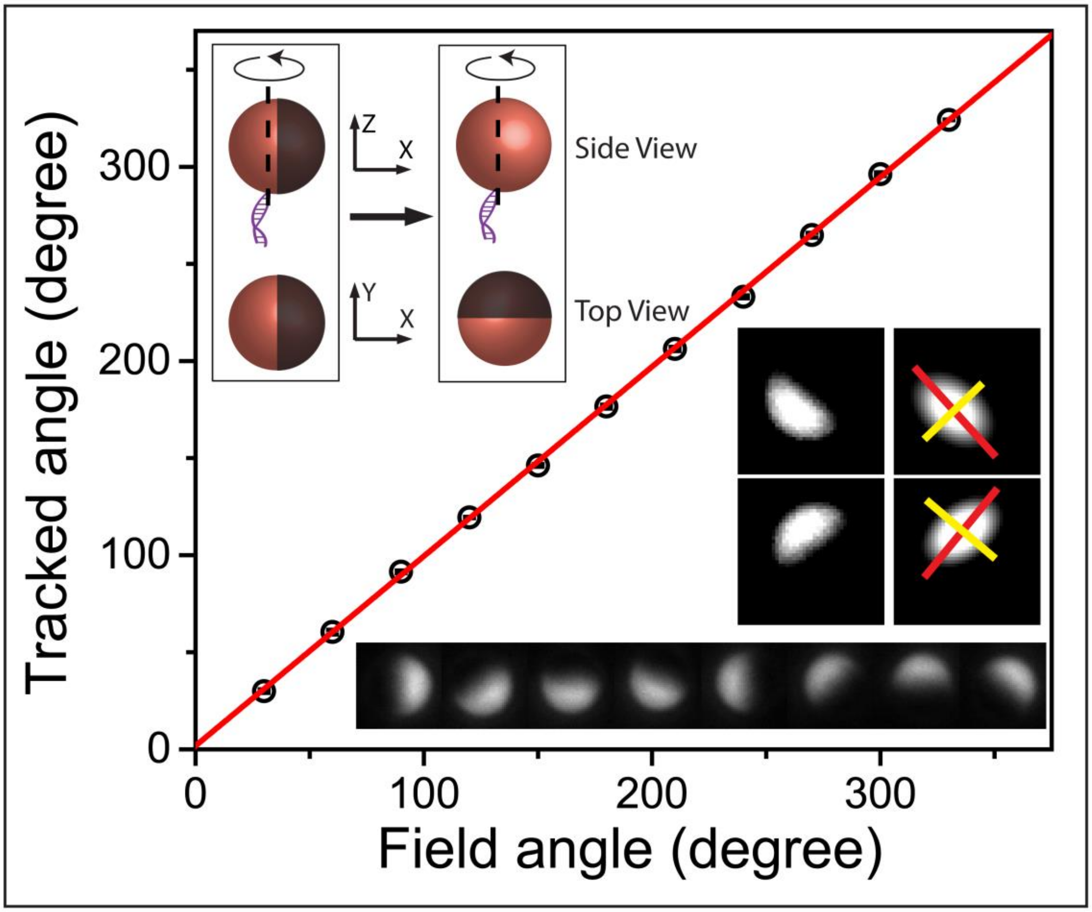

Figure 3.4 Using Janus bead for detecting rotational motion about optical axis. A DNA-tethered Janus bead is rotated by the quadrupole torque tweezers around z-axis and the rotation is dominantly confined in xy-plane. The bead is observed using epi-fluorescent microscopy. The bright phase of the crescent moon shape of the Janus particle is approximated to be ellipse whose intensity is fitted to 2D Gaussian distribution. The angular orientation is fitted as the parameter of the angular displacement between the major (labeled in red) axis of the ellipse and a fixed reference axis.

~2.7μm) were ligated on one end to an 800bp biotin-labeled segment and on the other end to an 800bp digoxigenin-labeled (Dig) segment. The Janus beads were biotinylated by using NHS as crosslinker to conjugate biotin-x-cadaverine (Life Technologies) to the carboxylate groups on the uncoated surface[30], and were then coated with streptavidin (Invitrogen) through biotin-streptavidin specific binding. The reaction chamber was constructed by bonding two pieces of cover glass by a paraffin film. The glass surfaces of the chamber were coated with anti-digoxigenin antibody (anti-Dig) through non-specific adsorption. The DNA-bead complexes were then attached to the bottom surface of the chamber through Dig/anti-Dig specific binding. We pulled the DNA upward until close to its contour length and then rotated the Janus bead about z-axis at specified angle steps. To orient the field generated by the quadrupole torque tweezers at a specific angle Φ, the current configuration applied to the quadrupole follows that $I = I_0 \cos \Phi$ is applied to one diagonal pair of poles and $I = I_0 \sin \Phi$ to the other pair. The tracked mean angle of a DNA-tethered Janus bead rotated by the quadrupole is in accordance with the applied field angle (Figure 3.4).

The angular rotation of Janus beads around the axis contained in xy-plane can also be quantified by the crescent phase change. As an example shown in Figure 7b, in the case where the dipole moment of the DNA-tethered Janus bead pointed from the center of the uncoated half to the center of the metal-coated half, when we gradually switched the magnetic polarity of the monopole from S to N, the metal-coating gradually blocks more fluorescent light emitted by the bead, causing a gradual decay in the total intensity of fluorescent image of the Janus bead. This shares the similarity to the blinking property of the Janus beads during rotational diffusion that made them useful biosensors, as mentioned above. The intensity profile normalized to the maximum value was empirically fitted to an equation similar to the Lorentzian peak function, $Int = [A(I + 0.2)^2 + 1]^{-1}$, where I is the current applied to the monopole and A is the fitting parameter, with A = 97.5 ± 4.2 in Figure 3.5. This intensity profile following the Janus bead rotating from the waxing phase to waning phase about the axis contained in the sample plane, combined with the method

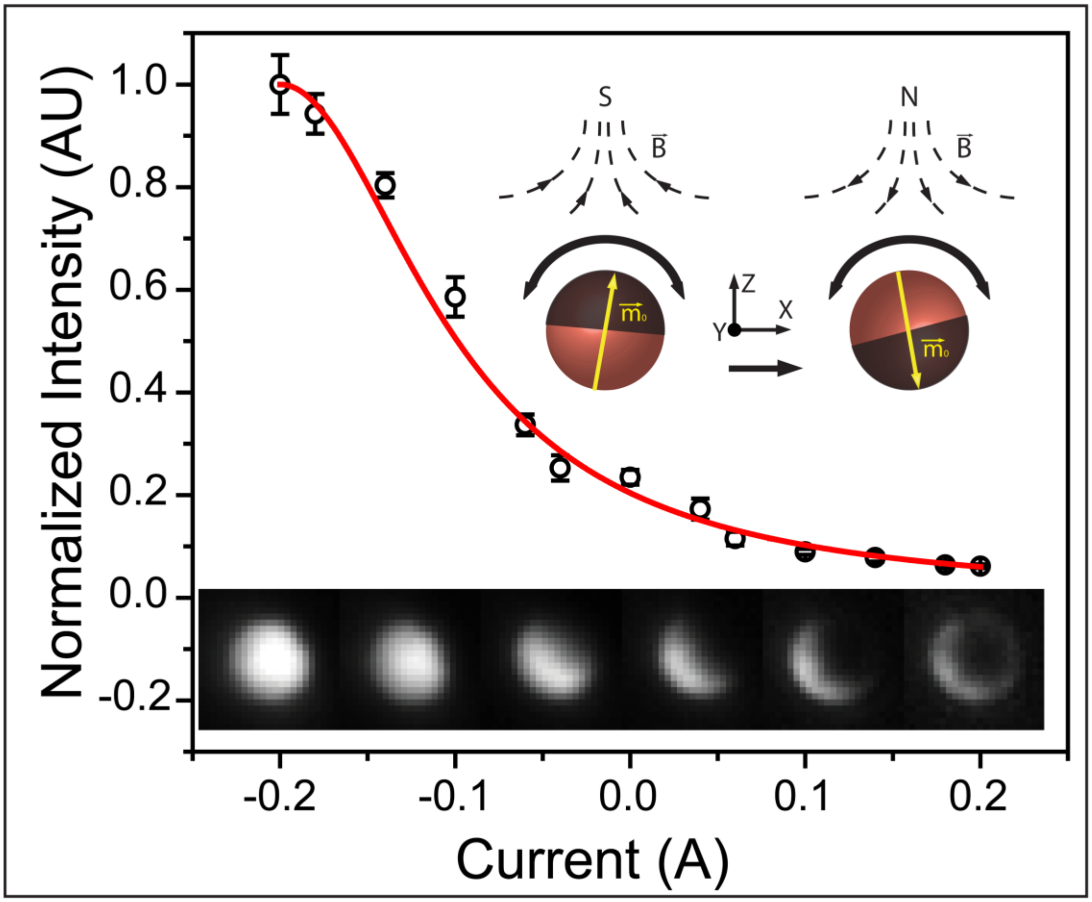

Figure 3.5 Magnetically-controlled intensity modulation of Janus beads for detecting rotational motion. A DNA-tethered Janus bead is rotated around an axis in the sample plane (y-axis) by changing the field strength magnitude of the monopole. By changing the direction of the current applied to the monopole, the dipole moment reorients 180 degrees. Following the rotation, the aluminum cap increasingly blocks the emitted light resulting in a decrease in the total fluorescent intensity of the bead imaged on the CCD camera.

described above for tracking the angular rotation about optical axis, can be applied to a wide range of studies involving quantification of the rotation dynamics of bead-attached biopolymers in 3D, providing dynamical information of all three rotational degrees of freedom.

3.4 Independent Control of Force and Torque

Finally, to demonstrate the decoupling of the force and torque control, we show that when a different magnitude of force is applied by the monopole tweezer to the biomolecule, the trap torsional stiffness can be controlled simply by applying different magnitude of current in the quadrupole. To experimentally demonstrate this we constructed a DNA-tethered bead configuration as described above. We estimate the force generated by the monopole on the Janus bead by first measuring the force-extension response of a DNA molecule attached to an uncoated fluorescent bead, the same stock of bead used for fabricating Jane bead. When the fluorescent bead is not in the focal plane of the microscope objective, spherical aberrations and diffraction give rise to ring patterns around the bead[31]. The z-position of the bead was calibrated by the radius of the ring pattern when the bead was placed at different height below the focal plane follow previous methods[32,33]. When we increase the electric current applied to the monopole, the mean z-position of the bead was measured to determine the extension of the DNA. The extension response of the DNA to the increasing current is in close agreement to the relationship predicted by the worm-like chain model (Figure 3.6b inset)[34,35]. From the force-extension profile, the force was estimated to range from tens of femtonewtons to several piconewtons and followed approximately ~1 pN/A linear relationship with the current applied to the monopole. To measure the independent torsional stiffness controlled by the quadrupole

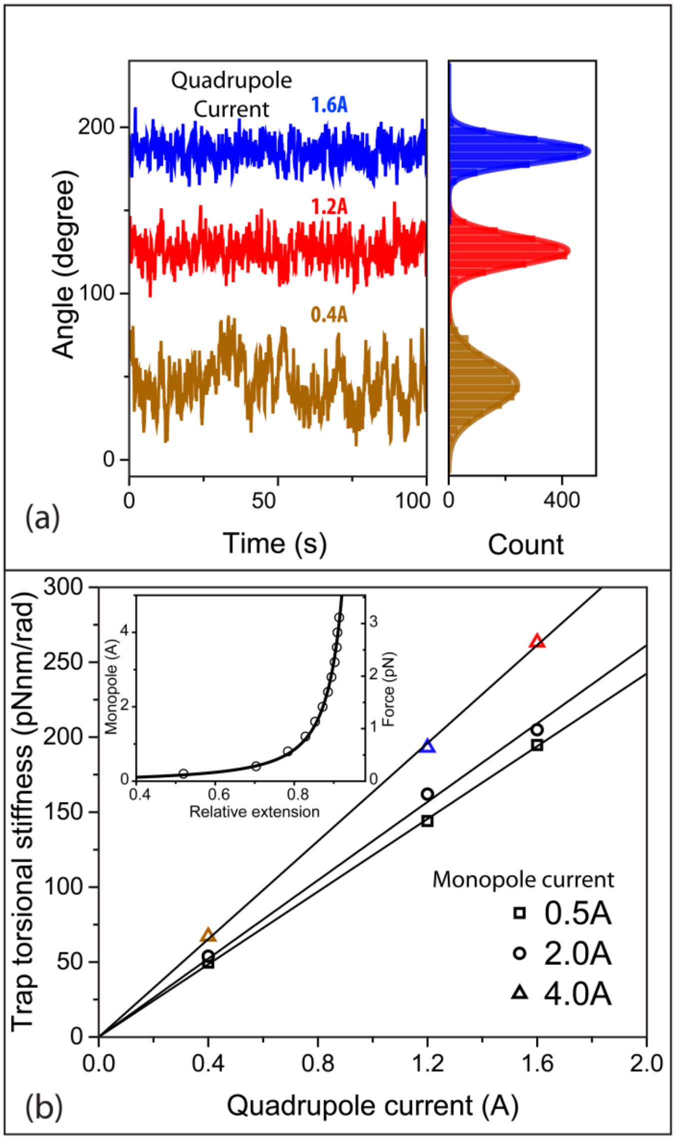

Figure 3.6 Trap torsional stiffness of the quadrupole tweezers is decoupled from the force applied to the superparamagnetic Janus bead. A DNA molecule is pulled upward in z-direction by the monopole and its extension response is measured when the current applied to monopole tweezer is increased (b inset). (a) At a constant force, when different magnitudes of current are applied to the quadrupoles, the measured angular variance of the thermal fluctuation of Janus bead around z-axis decreases. (b) The trap torsional stiffness calculated from the angular variance increases linearly with the current applied to the quadrupole tweezers.

tweezers at various force levels, we measured the angular variance of the Janus bead attached to the DNA molecule under different magnitude of tension. At forces ranging from a fraction of a piconewton to several piconewtons, the current in the quadrupole was increased from 0.4A to 1.6A, and the corresponding trap torsional stiffness was calculated from the variance of the angular fluctuation of the DNA-tethered Janus bead according to Equation (2.4). With increasing current applied to quadrupole, the angular variance of the thermal fluctuation decreases, as illustrated by the increasingly narrower Gaussian distribution fitted to the histogram of angular trace of the Janus bead under thermal fluctuation (Figure 3.6 a). The resultant trap torsional stiffness at different force level increased linearly with the current applied to the quadrupole tweezers and was decoupled from the tensile force applied to the DNA (Figure 3.6 b).

3.5 Conclusions

In summary, we have designed and implemented novel electromagnetic tweezers that are capable of independently controlling the stretching force and torsional trap stiffness when manipulating superparamagnetic microspheres. The decoupling of force and torque generation is achieved by combing an electromagnetic monopole that produces a strong magnetic field gradient above the sample for force generation, and a set of quadruples that produces a weak biasing rotating field in the sample plane for torque generation. We demonstrated the independent force and torque control flexibility by applying the tweezers to single-molecule experiments by attaching a Janus bead to DNA molecules. We showed that the tweezers is capable of applying piconewton-range of force on fluorescent superparamagnetic microspheres with diameter of 2μm. At different force levels, the trap torsional stiffness can be tuned to match the torsional mechanics of a wide range of biopolymers, from DNA[36,37], small proteins, to protein complexes and filaments[11,38,39]. We estimate that when using the microspheres with diameters of 2.7μm and 4.5μm that were used in previous studies[40,41], forces on the order of 10^2 pN to nanonewtons can be applied to the conjugated biomolecules under study. We noticed that the force applicable to commercially available fluorescent superparamagnetic microspheres is approximately an order of magnitude lower than that applicable to the non-fluorescent microspheres of the same size. We speculate that this is mainly caused by the lower concentration of iron oxide powder that is integrated into the microsphere, possibly due to the fluorescent dye molecules occupying available space in the microsphere matrix. Improved fabrication methods that allows integrating larger amount of superparamagnetic nanoparticles into microspheres without compromising fluorescent intensity will allow a wider range of force that can be applied to the microspheres. Furthermore, the capability of applying larger magnitude of force to microspheres with smaller diameter is desirable in achieving higher bandwidth of control and detection of the motion of microspheres, since the time resolution to detect changes in their angular orientation can be improved to the third power with respect to the decrease in bead diameter[17,41].

We also developed a novel method for tracking the angular motion of the biopolymers using Janus bead. The tracking routine proves feasible to provide information of rotational dynamics of the biopolymer in three-dimensional space. This method avoids the requirement of attaching fluorescent[18] or non-fluorescent fiduciary particles[17] to force probes to create geometry asymmetry for angular detection and simplifies the steps for experiment preparation. By using this tracking method to detect angular diffusion of Janus beads or analyzing their rotatory motion driven by electromagnetic tweezers, local rheological properties and torques can be investigated on the scale of microns to tens of nanometers[23,24]. In the system where the motion of the Janus bead is dominated by the rotation about an axis perpendicular to the optical axis of the microscope, because the rotation is directly related to the total fluorescent intensity of the Janus bead, as shown above where a Janus bead was rotated about the axis parallel to the sample plane, the determination of angular orientation can be simplified by intensity mapping, making the implementation of optoelectronic device for detecting angular motion feasible. This configuration can be explored in a variety of biological studies, for example, the investigation of the transcription process along DNA molecule where DNA is horizontally oriented[42–44].

Our fully electromagnetic tweezers allows enhancement to the bandwidth of control, as well as accurate sensing of force and torque generated by biomolecules and living cells if fast feedback loop is implemented. We envision that with the flexibility to apply force and torque in a decoupled manner, it can be used in a variety of experiments to study biophysical properties of biomolecules and understand mechanics of intracellular environment, for example, local rheological property and shear moduli in cytosol and nucleus[45–47].

3.6 Experimental Section

DNA construct

An 8 kilo-base pair DNA piece with 800 base pair biotinylated DNA ligated to one end and digoxigenin-labeled DNA to the other end was used in all the DNA-tethered particle assays. 8 kilo-base pair of DNA piece was amplified from plasmid pAR1219 (Sigma) by PCR with forward primer incorporating an AgeI restriction site and reverse primer incorporating an NheI restriction site. Biotin- and digoxigenin-labeled DNA segments were generated by amplifying an 800 base pair segment in pRSET-EmGFP

(Life Technologies) vector by PCR with either biotin-16-dUTP or digoxigenin-11-dUTP (Roche Applied Science) supplemented to the dNTP mixture. Biotin-labeled segment has an XmaI site close to one end and digoxigenin-labeled segment has an XbaI site close to one end. The DNA segments were digested by corresponding restriction enzymes. The three segments were then ligated by T4 ligase. In the ligation procedure, four restriction enzymes were added to the ligation mixture to reduce the self-ligation of individual segments and increase the ligation yield of the DNA piece with biotin- and digoxigenin-labeled handles on each end. The DNA with two handles on both sides is purified by gel extraction using QIAquick Gel Extraction Kit (Qiagen). All restriction enzymes were purchased from New English Biolabs.

DNA stretching assay

A flow chamber was constructed from microscope cover glasses with paraffin film as spacer in between. Two No. 1 (thickness of approximately 170μm), $60\text{mm} \times 22\text{mm}$ microscope cover glasses (Fisher scientific) were used for the chamber. Both cover glasses were cleaned by acid wash and silanized by 3-aminopropyltriethoxysilane. In one cover glass, two holes of ~2mm diameter were drilled along center axis parallel to the long side, with ~30mm separation. In each hole, one Tygon tubing (Saint-Gobain) segment of length ~25mm was inserted, extending a couple of millimeters through the hole, and fixated by applying general purpose 5-minute epoxy (Thorlabs) on the side of insertion. After the epoxy hardened, the small segments extending through the hole on the side without epoxy were cut by a razor. On the other cover glass, a thin layer of 1% nitrocellulose dissolved in amyl acetate was deposited by pipetting and then dry in air. A $35\text{mm} \times 5\text{mm}$ slit window was cut out of a piece of $60\text{mm} \times 22\text{mm}$ Parafilm, and then the Parafilm was sandwiched between the cover glass having tubings attached, and the cover glass treated by nitrocellulose, with nitrocellulose treated side facing the chamber. The Parafilm both serves as a spacer and provides a space for flow chamber.

The DNA stretching assay was carried out in a similar manner as described[40,41]. The flow chamber was incubated with 50μg/ml anti-digoxigenin antibody (Roche Applied Science) dissolved in PBS buffer (137 mM NaCl, 2.7 mM KCl,10 mM Na_2HPO_4, 2 mM KH_2PO_4, pH 7.4) overnight. The surface of the cover glass was then passivated by flowing in 2mg/ml bovine serum albumin (BSA) in PBS buffer and incubated for 45 minutes. To conjugate the biotin-labeled end of DNA to the microsphere, DNA was incubated with Janus bead or uncoated microsphere functionalized by streptavidin in PBS buffer for 30 minutes in a microcentrifuge tube with end-to-end rotation to avoid deposition of the microspheres by gravity. The DNA was diluted so that each Janus bead or uncoated microsphere would statistically have only one or fewer DNA conjugated to the surface. Then DNA-microsphere mixture was introduced into the flow chamber and was incubated for 30 minutes to allow attachment of DNA-tethered particles to the anti-digoxigenin coated surface. Janus beads or uncoated microspheres that were not tethered to the surface were washed out by PBS buffer.

Fabrication and functionalization of Janus particle

Fluorescently-labeled superparamagnetic microspheres (2μm in diameter) were dispersed in ethanol and spread on a glass surface by pipetting. The glass surface was tilted from horizontal position by about 10° angle to facilitate forming a monolayer of microspheres on the surface. The sample slide was dried in air. Then the sample slide was put into an E-beam evaporator using small point sources and long throw distances, to enhance the directionality of deposition and reduce the heat introduced to the substrate. Aluminum vapor deposition was performed in high vacuum, so the vaporized aluminum moves in a nearly straight line from the source to the target, thereby coating only one hemisphere of the particles and leaving the other hemisphere intact. The slide was put into a container wrapped in aluminum foil, and can be preserved in a 4ºC refrigerator very well over a long period of time. The coated Janus beads can be removed from the slide at any point using a paintbrush and resuspended in PBS buffer or 25mM 2-(N-morpholino)ethanesulfonic acid (MES) dissolved in deionized water (pH6) in a microcentrifuge tube.

To functionalize the Janus beads with streptavidin for attachment to biotinylated DNA molecule, carboxylate group on the surface (Spherotech) were conjugated to biotin-x-cadaverine (Life Technologies, B1596) by using carbodiimide compounds, 1-ethyl-3-(-3-dimethylaminopropyl) carbodiimide hydrochloride (EDC) (Pierce, 22980) mediated reaction. The reaction was quenched by glycine. Then the beads were washed by setting the microcentrifuge tube on a strong magnet. The superparamagnetic beads were attracted to the bottom of the tube and the supernatant was aspirated before the beads were resuspended in MES solution again. The wash step was repeated at least 3 times. Biotinylated beads were distributed into aliquots and stored in 4ºC refrigerator. They tend to remain stable and functional till further conjugation. To conjugate Janus beads with streptavidin, the biotinylated Janus beads were incubated with streptavidin (Invitrogen, S-888) for 2 hours with end-to-end rotation to avoid deposition of the microspheres by gravity. Then the beads were washed in PBS buffer using the aforementioned method during biotinylation step.

3.7 Bibliography

1. Batchelor, G. K. *An Introduction to Fluid Dynamics*. (Cambridge University Press, 2000).
2. Crocker, J. C. & Grier, D. G. Methods of Digital Video Microscopy for Colloidal Studies. *J. Colloid Interface Sci.* **179,** 298–310 (1996).
3. Kreizer, M., Ratner, D. & Liberzon, A. Real-time image processing for particle tracking velocimetry. *Exp. Fluids* **48,** 105–110 (2010).
4. Fonnum, G., Johansson, C., Molteberg, A., Mørup, S. & Aksnes, E. Characterisation of Dynabeads® by magnetization measurements and Mössbauer spectroscopy. *J. Magn. Magn. Mater.* **293,** 41–47 (2005).
5. Xu, J. *et al.* Simultaneous, single particle, magnetization and size measurements of micron sized, magnetic particles. *J. Magn. Magn. Mater.* **324,** 4189–4199 (2012).
6. Baselt, D. R. *et al.* A biosensor based on magnetoresistance technology. *Biosens. Bioelectron.* **13,** 731–739 (1998).
7. Sbalzarini, I. F. & Koumoutsakos, P. Feature point tracking and trajectory analysis for video imaging in cell biology. *J. Struct. Biol.* **151,** 182–195 (2005).
8. Jain, A. K. *Fundamentals of Digital Image Processing*. (Prentice Hall, 1989).
9. Cheezum, M. K., Walker, W. F. & Guilford, W. H. Quantitative comparison of algorithms for tracking single fluorescent particles. *Biophys J* **81,** 2378–88 (2001).
10. Normanno, D., Capitanio, M. & Pavone, F. S. Spin absorption, windmill, and magneto-optic effects in optical angular momentum transfer. *Phys. Rev. A* **70, -** (2004).
11. Janssen, X. J. A. *et al.* Torsion Stiffness of a Protein Pair Determined by Magnetic Particles. *Biophys J* **100,** 2262–2267 (2011).
12. Tsuda, Y., Yasutake, H., Ishijima, A. & Yanagida, T. Torsional rigidity of single actin filaments and actin–actin bond breaking force under torsion measured directly by in vitro micromanipulation. *Proc. Natl. Acad. Sci.* **93,** 12937–12942 (1996).
13. Deriu, M. A. *et al.* Anisotropic elastic network modeling of entire microtubules. *Biophys. J.* **99,** 2190–2199 (2010).
14. Lipfert, J., Kerssemakers, J. W., Jager, T. & Dekker, N. H. Magnetic torque tweezers: measuring torsional stiffness in DNA and RecA-DNA filaments. *Nat Methods* **7,** 977–80 (2010).

15. Sielaff, H. *et al.* Domain compliance and elastic power transmission in rotary F_0F_1-ATPase. *Proc. Natl. Acad. Sci.* **105,** 17760–17765 (2008).
16. Gutierrez-Medina, B., Fehr, A. N. & Block, S. M. Direct measurements of kinesin torsional properties reveal flexible domains and occasional stalk reversals during stepping. *Proc Natl Acad Sci* **106,** 17007–12 (2009).
17. Lipfert, J., Kerssemakers, J. J. W., Rojer, M. & Dekker, N. H. A method to track rotational motion for use in single-molecule biophysics. *Rev. Sci. Instrum.* **82,** (2011).
18. Harada, Y. *et al.* Direct observation of DNA rotation during transcription by Escherichia coli RNA polymerase. *Nature* **409,** 113–5 (2001).
19. Celedon, A. *et al.* Magnetic tweezers measurement of single molecule torque. *Nano Lett* **9,** 1720–5 (2009).
20. Ha, J. W., Sun, W., Wang, G. & Fang, N. Differential interference contrast polarization anisotropy for tracking rotational dynamics of gold nanorods. *Chem. Commun.* **47,** 7743–7745 (2011).
21. Walther, A. & Müller, A. H. E. Janus particles. *Soft Matter* **4,** 663–668 (2008).
22. McNaughton, B. H. *et al.* Magnetic confinement of Brownian rotation to a single axis and application to Janus and cluster microparticles. *Appl. Phys. Lett.* **97,** (2010).
23. Behrend, C. J., Anker, J. N., McNaughton, B. H. & Kopelman, R. Microrheology with modulated optical nanoprobes (MOONs). *J. Magn. Magn. Mater.* **293,** 663–670 (2005).
24. Behrend, C. J., Anker, J. N. & Kopelman, R. Brownian modulated optical nanoprobes. *Appl. Phys. Lett.* **84,** 154–156 (2004).
25. Anker, J. N. & Kopelman, R. Magnetically modulated optical nanoprobes. *Appl. Phys. Lett.* **82,** 1102–1104 (2003).
26. Behrend, C. J. *et al.* Metal-capped Brownian and magnetically modulated optical nanoprobes (MOONs): Micromechanics in chemical and biological microenvironments. *J. Phys. Chem. B* **108,** 10408–10414 (2004).
27. Choi, J., Zhao, Y., Zhang, D., Chien, S. & Lo, Y.-H. Patterned Fluorescent Particles as Nanoprobes for the Investigation of Molecular Interactions. *Nano Lett.* **3,** 995–1000 (2003).

28. Sinn, I. *et al.* Magnetically uniform and tunable Janus particles. *Appl. Phys. Lett.* **98,** (2011).
29. Lipfert, J., Koster, D. A., Vilfan, I. D., Hage, S. & Dekker, N. H. Single-molecule magnetic tweezers studies of type IB topoisomerases. *Methods Mol Biol* **582,** 71–89 (2009).
30. Hermanson, G. T. *Bioconjugate Techniques*. (Academic Press, 2010).
31. Born, M. & Wolf, E. *Principles of Optics: Electromagnetic Theory of Propagation, Interference and Diffraction of Light*. (Cambridge University Press, 1999).
32. Wu, M., Roberts, J. & Buckley, M. Three-dimensional fluorescent particle tracking at micron-scale using a single camera. *Exp. Fluids* **38,** 461–465 (2005).
33. Speidel, M., Jonáš, A. & Florin, E.-L. Three-dimensional tracking of fluorescent nanoparticles with subnanometer precision by use of off-focus imaging. *Opt. Lett.* **28,** 69–71 (2003).
34. Bouchiat, C. *et al.* Estimating the persistence length of a worm-like chain molecule from force-extension measurements. *Biophys J* **76,** 409–13 (1999).
35. Smith, S. B., Finzi, L. & Bustamante, C. Direct mechanical measurements of the elasticity of single DNA molecules by using magnetic beads. *Science* **258,** 1122–6 (1992).
36. Janssen, X. J. A. *et al.* Electromagnetic Torque Tweezers: A Versatile Approach for Measurement of Single-Molecule Twist and Torque. *Nano Lett.* **12,** 3634–3639 (2012).
37. Mosconi, F., Allemand, J. F. & Croquette, V. Soft magnetic tweezers: A proof of principle. *Rev. Sci. Instrum.* **82,** 034302–034302 (2011).
38. Pänke, O., Cherepanov, D. A., Gumbiowski, K., Engelbrecht, S. & Junge, W. Viscoelastic dynamics of actin filaments coupled to rotary F-ATPase: angular torque profile of the enzyme. *Biophys. J.* **81,** 1220–1233 (2001).
39. Okuno, D., Iino, R. & Noji, H. Stiffness of gamma subunit of F(1)-ATPase. *Eur. Biophys. J. Biophys. Lett.* **39,** 1589–1596 (2010).
40. Strick, T. R., Allemand, J. F., Bensimon, D. & Croquette, V. Behavior of supercoiled DNA. *Biophys J* **74,** 2016–28 (1998).

41. Lipfert, J., Wiggin, M., Kerssemakers, J. W. J., Pedaci, F. & Dekker, N. H. Freely orbiting magnetic tweezers to directly monitor changes in the twist of nucleic acids. *Nat Commun* **2,** 439 (2011).
42. Visnapuu, M.-L., Fazio, T., Wind, S. & Greene, E. C. Parallel arrays of geometric nanowells for assembling curtains of DNA with controlled lateral dispersion. *Langmuir* **24,** 11293–11299 (2008).
43. Finkelstein, I. J., Visnapuu, M. L. & Greene, E. C. Single-molecule imaging reveals mechanisms of protein disruption by a DNA translocase. *Nature* **468,** 983–7 (2010).
44. Wang, F. & Greene, E. C. Single-Molecule Studies of Transcription: From One RNA Polymerase at a Time to the Gene Expression Profile of a Cell. *Mech. Transcr.* **412,** 814–831 (2011).
45. Lavelle, C. Forces and torques in the nucleus: chromatin under mechanical constraints. *Biochem Cell Biol* **87,** 307–22 (2009).
46. Satcher, R. L. & Dewey, C. F. Theoretical estimates of mechanical properties of the endothelial cell cytoskeleton. *Biophys. J.* **71,** 109–118 (1996).
47. Canetta, E., Duperray, A., Leyrat, A. & Verdier, C. Measuring cell viscoelastic properties using a force-spectrometer: Influence of protein-cytoplasm interactions. *Biorheology* **42,** 321–333 (2005).

Chapter 4

OBLIQUE DARK-FIELD SCATTERING OF OPTICALLY ANISOTROPIC MICROSPHERES FOR DETECTING ROTATIONAL MOTION

In this chapter, I will present the design and implementation of a novel method that enables us to directly record the angular displacement of particles undergoing rotational motion by using asymmetric illumination of optically anisotropic beads. The method is implemented by illuminating a partially metal-coated bead with a laser beam coupled into the back side of a microscope objective. The laser beam illuminating beads placed in the sample plane is oriented at an oblique angle to form an asymmetric illumination and the back-scattered light from beads is collected by an optical system using dark-field. I will discuss the principle of scattering of uncoated and partially-coated microspheres using this asymmetric illumination method based on the geometric ray tracing supported by optical simulation. Then I will show that by using an optoelectronic system to detect scattering signal of a Janus bead, the method is able to map angular displacements of the bead to the electrical signal and therefore can be used to determine the angular displacement of the biological molecule when conjugated to the bead. This method obviates image acquisition and image processing procedures commonly used in previous studies[1–3], and it has the potential to significantly enhance the bandwidth of detection. I will conclude with a discussion of the usage of this method in a range of biophysical measurements including magnetic trapping and tethered particle motion.

4.1 Background

Rotational tracking is useful for studying micro-rheological properties of materials, as well as rotary motion in biological processes, e.g., ATP synthesis accomplished by ATP synthase to provide energy for the cell[4,5], the rotation of flagella to propel the locomotion of bacteria[6,7], and DNA going through winding and unwinding[8,9]. A variety of methods have been used to detect the rotational motion. Most methods require attaching fiducial beads to force probes using bioconjugation to introduce asymmetry[1,2,10], and some require more sophisticated nanofabrication processes, such as in the case of nanorods[3]. What is shared among these methods is that the post-processing of the images of the particles is required to detect the asymmetry in the images. Fluorescent particles with diameters of tens to hundreds of nanometers have been used to attach to the force probes as fiducial bead, and the positions of these fluorescent particles were tracked to indicate the angular orientation of the proteins or nucleic acids under study[2,10]. In these studies, fluorescent images of the fiducially attached beads were acquired using fluorescence microscopy and the centers of the fluorescently labeled fiducial beads in the images were localized by position tracking algorithms[11].

Aside from the low-efficiency of bioconjugation required for attaching fiducial beads to force probes, there are two additional major drawbacks in the implementation of this type of rotation tracking method. First, the use of fluorescence microscopy for detecting the fiducial beads requires part of the available wavelength range and additional optical filters in the path of the fluorescence microscope and precludes detecting other biological reagents that are often observed using fluorescence microscopy. This shortcoming is shared by methods that use bright-field for detecting rotation of microspheres[12], and detection of angular orientation of gold nanorods using dark-field[13,14] and differential interference contrast microscopies[15,16], when the wavelength required overlaps those of the fluorescence measurements. Secondly, post-processing of images is often time-consuming, which is particularly a problem for algorithms involving complicated image fitting routines that have a high demand of computational power[17,18]. In contrast to the methods for detecting rotation motion, position tracking methods based on electrical signals that use lateral-effect photodiodes[19,20] or quadrant photodiodes[21,22] have been developed to detect the lateral position of particles[23]. These methods do not require acquisition of images of particles by a camera. They typically have higher bandwidth than image-based methods which makes them suitable tools for real-time detection, analysis as well as control, since closed-loop feedback is more convenient to be implemented in these systems.

We have developed a novel methodology that enables us to directly record the angular displacement of particles undergoing rotational motion by using asymmetric illumination of optically anisotropic beads. In this method, we are using the Janus beads described in Chapter 3, which are optically anisotropic particles, as probes for detecting angular motion. Janus beads are microspheres with a thin, partial, metallic coating applied to one side, while the other half maintains the original polystyrene or silica surface. We use an optoelectronic system to detect a scattering signal from these bead which enables direct high-speed measurement of the angular displacement of the bead. I will show that this method is able to map angular displacements to electrical signal and can be used to determine the angular displacement of the biological molecule when conjugated to the Janus bead. This method obviates image acquisition and image processing procedures commonly used in previous studies, and it has the potential to significantly enhance the bandwidth of detection.

4.2 Design and Implementation of the Oblique Dark-field Scattering System

As outlined above, the ability of the oblique dark-field scattering system (ODFS) to detect the angular orientation of a microsphere is based on the asymmetry in the illumination incident on the microsphere and the optical anisotropy introduced to the microsphere in Janus particles about the optical axis of the imaging system. The asymmetric illumination is designed so that a beam of light can be shed on to the particle with an angular deviation from the central optical axis of the microscope. This is achieved by a scheme resembling the optical path of the excitation laser beam used in objective-type total internal reflection fluorescence microscopy[24,25], but without causing the total internal reflection at the glass-water interface of the flow chamber. To illuminate a microsphere obliquely, a beam with a diameter of approximately 10 µm is coupled into the microscope objective by directing the beam parallel to the optical axis of the microscope objective with a distance offset from the central axis. The beam is focused at the back focal plane of the objective at a position a couple of millimeters from the center. The beam is then collimated by the lenses in the objective and exits the objective obliquely, forming an angle with respect to the central optical axis. This collimated beam goes through the focal point of the objective to illuminate the sample placed along the optical axis, and the distance of the

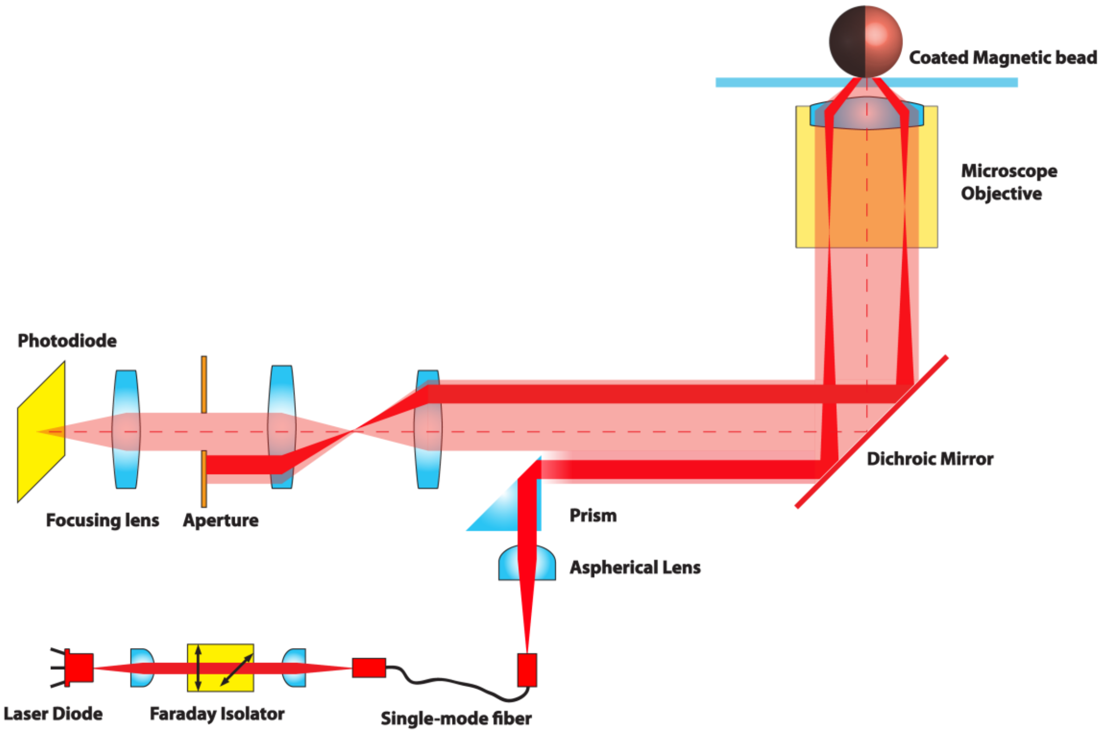

Figure 4.1 Schematic of the oblique dark-field scattering system for detecting rotation of Janus beads. The illuminating light (bright red) emitted from a laser diode with nominal wavelength of 785nm is coupled into a single-mode fiber. A Faraday isolator is placed in the coupling optics to reduce back-reflection. At the other end of the optical fiber, the light is converged by an aspherical lens to be focused at the back focal plane of the microscope objective at a point millimeters away from the optical axis of the objective. The illuminating light exits the objective forming an angle with respect to the vertical axis without total internal reflection at the glass-water interface of the flow chamber. The scattered light (shaded light red) from the sample is collected by a photodiode, while the illuminating light reflected at the glass surfaces of the flow chamber that enters into the imaging system is blocked by an aperture from being collected by the photodiode.

beam from the central axis determines the angle of the collimated beam for illumination. This distance offset is set to a sufficiently small value so that the exiting angle of the collimated beam is below the critical angle required for creating total internal reflection, but large enough to produce sufficient asymmetry about the optical axis for scattering. To image only the scattered light, an imaging system resembling dark-field microscopy is used[26]. To block the illuminating light reflected at the glass surfaces of the flow chamber, an aperture is integrated into the imaging system to block the light at high N.A. and only allow the light below a set N.A. to be collected. The diameter of the aperture is adjusted to determine the N.A. for light collection, and should be set to allow maximal scattered light through while blocking out the reflected illuminating light.

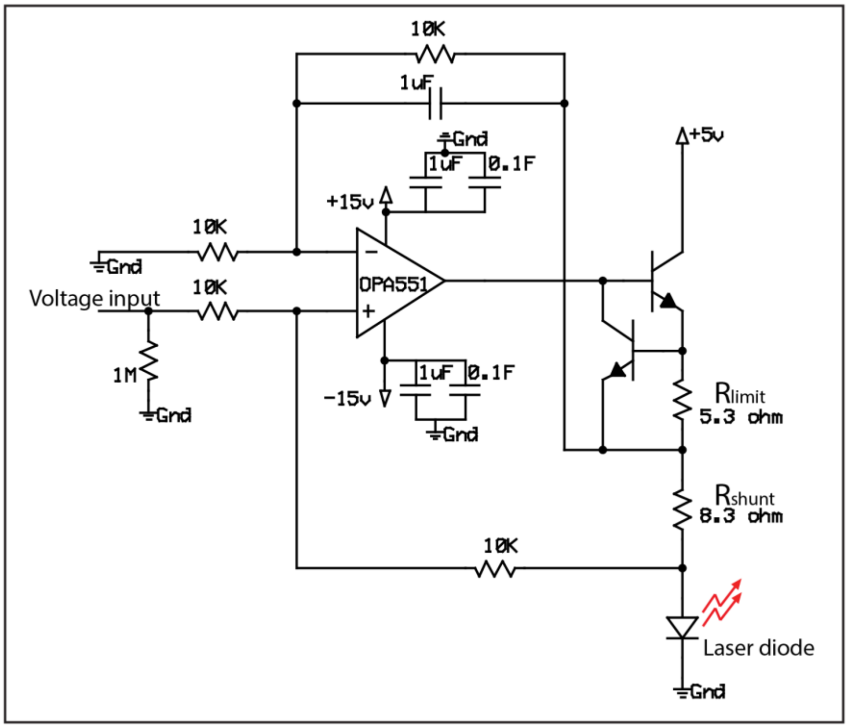

Figure 4.2 Driver circuit for laser diode. The driver circuit serves as a voltage-to-current converter for laser diode and outputs a current through the laser diode that is proportionate to the voltage input. The value of R_{shunt} can be tuned to change the gain of the circuit. The value of R_{limit} can be tuned to change the maximum current allowed to pass through the laser diode to prevent damage.

The design of the oblique dark-field scattering system is illustrated in Figure 4.1. The illuminating light emitted from a laser diode with nominal wavelength of 785nm is coupled into a single-mode fiber. A Faraday isolator is placed in the coupling optics to reduce back-reflection. At the other end of the optical fiber, the light is converged by an aspherical lens and coupled into the microscope by a prism through total internal reflection. The position of the aspherical lens along the optical axis is set so that the beam is focused at the back focal plane of the microscope objective. Then the beam is directed into the microscope objective by a narrow-band dichroic mirror that is designed to reflect only the wavelength close to that of the laser diode. The position and angle of the illumination beam is adjusted by an two-axis positioner to which the fiber is attached and the prism mounted on a tip-tilting plate, so that the beam is parallel to the optical axis of the microscope objective and the focal point of the beam is positioned to a point millimeters away from the optical axis of the objective. The beam is collimated when exiting the objective into the sample plane, forming an angle with respect to the vertical axis without total internal reflection at the glass-water interface of the flow chamber, with the center position of the beam positioned closed to the front focal point of the objective. The light scattered from the sample is collected by a photodiode, while the illuminating light reflected at the glass surfaces of the flow chamber that enters into the imaging system is blocked by an aperture and thus not collected by the photodiode.

4.3 Oblique Dark-field Scattering of Microspheres

Scattering of light on a microscopic sphere can be calculated by Mie theory[27], but for practical reason, we used geometrical ray tracing to understand the trajectory of the illuminating light after it was scattered on a microsphere due to localized non-uniformities in the medium through which they pass[28]. The geometric optics approach has been used to compute the angular distribution of scattered light involving interactions of a plane electromagnetic wave with a particle much larger than the incident wavelength[29], and the errors associated with the geometrical ray tracing compared to the Mie theory for perfect spheres with diameters close to the wavelength have been characterized[30]. This approach is based on the simplifying assumption that the light beam may be thought of as consisting of separate localized rays that travel along straight-line paths[31]. In the model we used, we also simplified the quantitative analysis by assuming that the intensity distribution of the incident light across the scattering cross-section area was uniform and the incident light was unpolarized. The angular distribution of the incidence and refraction of the light passing through a boundary between two different isotropic media, specifically in our case, the boundary between aqueous solution and the medium of which the microsphere is composed, is described by Snell's law[32]:

$$\frac{n_1}{n_2} = \frac{sin\,\theta_t}{sin\,\theta_i}, \tag{4.1}$$

where n_1 is the refractive index of the medium through which the light propagates before it encounters the boundary, n_2 is that after it encounters the boundary, θ_i is the angle between the direction of the incident light and that of the normal vector of the interface surface, or the angle of incidence, and θ_t is the angle of refraction (Figure 4.3a). In the process of scattering of a light beam with uniform intensity by a polystyrene or silica bead in aqueous solution, the incident light $\hat{e}_0$ propagates through the aqueous solution until it encounters the surface of the bead. Part of the light is reflected at the boundary ê1, and part of the light penetrates into the bead as refracted light, ê2. The refracted light, ê2, propagates

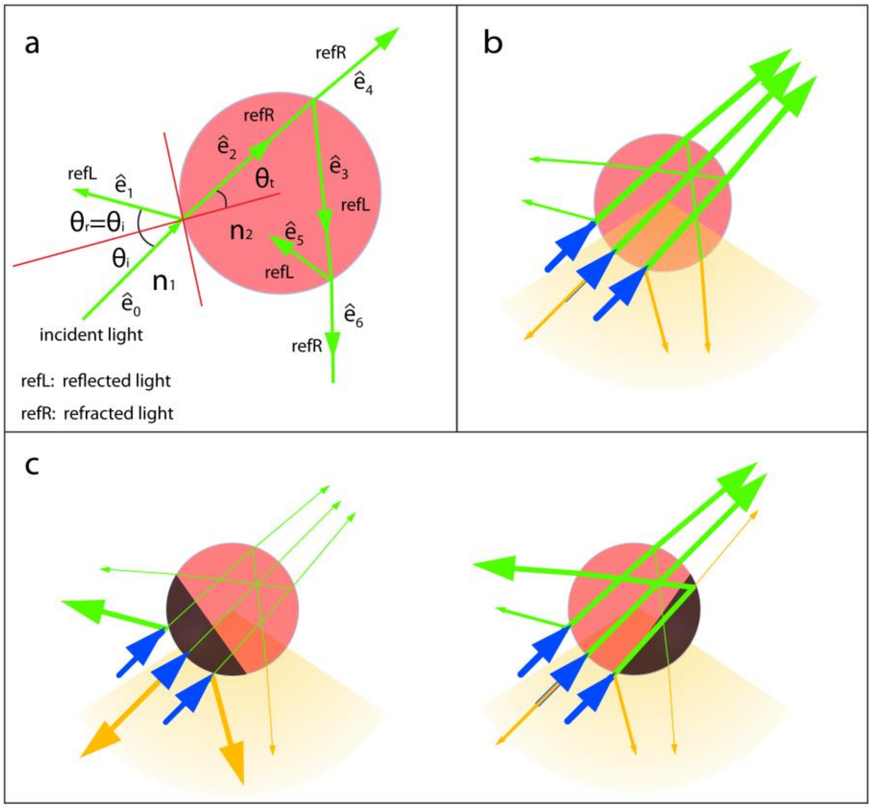

Figure 4.3 Geometric ray tracing model for oblique dark-field scattering of uncoated and coated microspheres. (a) An illustrative geometry for a ray-by-ray geometric optics approach for light scattering by a sphere. The annotation of angles and refractive indices are consistent with those used in the Snell's equation (main text). (b) Light scattered by an uncoated sphere. Incident illuminating light (blue arrows) refracts and reflects at the boundary between the microsphere and surrounding medium. The scattered light is collected by an imaging system of certain numerical aperture (orange fan-shaped area). Part of the scattered light enters the collectable angle (orange arrows), contributing to the scattering image of the bead, while the rest of the scattered light (green) falls out of the collectable angle of the imaging system. (c) Light scattered by a Janus bead and collected by a fixed numerical aperture. When the coating is oriented to an angle at which the scattering cross-section is large, more light is reflected into the angle that corresponds to the numerical aperture of the imaging system (large orange arrows), while less light can be collected when the Janus bead is reoriented to reduce the scattering cross-section (small orange arrows).

through the bead until it encounters the opposite surface of the bead and a fraction of it internally reflects on the interface, as $\hat{e}_3$, while another fraction refracts and exits the bead, as $\hat{e}_4$. The internally reflected light $\hat{e}_3$ repeats the reflection and refraction again when it encounters another interface, shown as $\hat{e}_5$ and $\hat{e}_6$ respectively (Figure 4.3a).

When a microsphere is not coated, due to the higher refractive index of the polystyrene or silica material in the microsphere, the light converges when it propagates through the bead and is focused to a smaller area at the rear surface of the bead relative to the light source. To get a deeper understanding of the effect of asymmetric illumination and dark-field imaging system on the image formation of the uncoated polystyrene or silica bead, we conducted a simulation to identify the subset of the surface boundary of a bead at which the reflected or refracted light can be collected by the dark-field imaging system given a certain numerical aperture (N.A.). The simulation was conducted in MATLAB (The Mathworks Inc.) based on geometric ray tracing, with the simplifying assumptions that the intensity of illuminating electromagnetic wave was uniform and unpolarized,. The simulation distinguished the rays that fell out of the N.A. and were not collected by the imaging system (colored green in Figure 4.3b) from the rays that fell within the N.A. and were collected by the imaging system (colored orange in Figure 4.3b). Then the rays that fell within the N.A. were back traced to determine the boundary surface area of the bead from which the rays were either reflected or refracted. The resultant boundary surface area with rays collected by the imaging system were presumed to appear as bright spots as the bead was imaged by the dark-field imaging system. The geometric ray tracing to predict the trajectory of light scattered on the bead was conducted to the 3rd order reflection and refraction, namely $\hat{e}_5$ and $\hat{e}_6$ (Figure 4.3a), with higher order reflection and refraction not taken into consideration. Figure 4.3b illustrates the geometric ray tracing model used in the simulation. The incident light (blue) is set to form a 45° angle with regard to the optical axis of the imaging system, and the N.A. is set to 0.8 (shaded orange cone-shaped area), which is an approximate estimate of the corresponding aperture in the dark-field imaging system (Figure 4.1). The refractive index of surrounding medium was set to that of water, 1.33, and the refractive index of the bead material was set to sweep of range, including that of a polystyrene bead[33], 1.58, and that of a silica bead, 1.45, at wavelength of 785nm.

The simulation result shows that there are two parts of bead surface from which the reflected light falls into the N.A. of the imaging system (Figure 4.4a). For clarity, the area facing the illuminating light where predominantly the external reflection ($\hat{e}_1$ in Figure 4.2a) was collected by the imaging system was colored in magenta, and the area further away from the illumination light where predominantly the refracted light ($\hat{e}_6$ in Figure 4.2a) of the internal reflection ($\hat{e}_3$ in Figure 4.2a) was collected by the imaging system (Figure 4.4b) was colored in green. To predict the intensity of these area in the image, the intensity of reflected and refracted light was calculated following Fresnel equations[32], normalized to the incident light:

$$R_s = |\frac{n_1 \cos\theta_i - n_2 \cos\theta_t}{n_1 \cos\theta_i + n_2 \cos\theta_t}|^2 , \tag{4.2}$$

$$R_p = |\frac{n_1 \cos\theta_t - n_2 \cos\theta_i}{n_1 \cos\theta_t + n_2 \cos\theta_i}|^2 , \tag{4.3}$$

$$R = \frac{R_s + R_p}{2} , \tag{4.4}$$

$$T = 1 - R , \tag{4.5}$$

where R_s is the reflectance for s-polarized light, R_p is the reflectance for p-polarized light, R is the reflectance of the unpolarized incident light, containing an equal mix of s- and p-

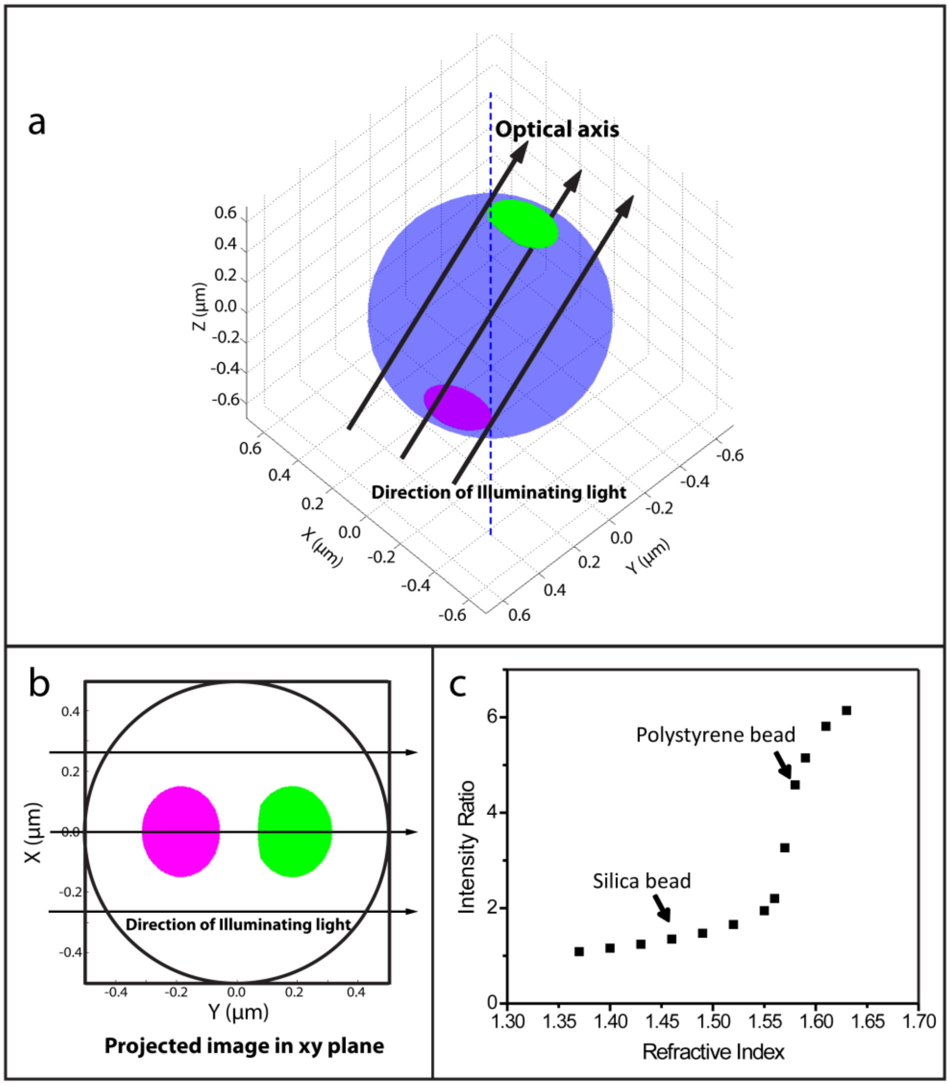

Figure 4.4 Simulation of oblique dark-field scattering of a microsphere. (a) Simulation of the scattering image of a polystyrene bead. The illumination is uniform in the direction indicated by the arrows. Corresponding to the aperture in the dark-field imaging system, the numeric aperture (N.A.) in the simulation is 0.8. The image is simulated by geometric ray tracing (Figure 4.2a) of an uncoated paramagnetic bead. The colored areas represent the parts of bead surface from which the reflected light falls into the NA of the imaging system. (b) 2D projection of the simulation in xy-plane. (c) The intensity of the light is calculated from the reflectance and transmittance of unpolarized light as predicted by the Fresnel equations.

polarizations, and T is the transmittance. For an uncoated polystyrene bead with refractive index of 1.58, the simulation predicts that the integrated intensity of the area facing away from the incident light (green) is 4.6 times larger than the area facing toward the light (magenta), while for a silica bead with refractive index of 1.45, the ratio is about 1.3 (Figure 4.4c). The higher intensity of the area facing away from the incident light is mainly due to the focusing effect of the bead that functions as a spheric lens. This prediction is consistent with the experimental observation of 2.9-μm diameter silica bead (Figure 4.5a), 1-μm diameter polystyrene beads (Figure 4.5b).

When a microsphere is partially coated with a thin layer of metal coating, the metal coating back-scatters the light to a greater extent than the polystyrene or silica, effectively serving as a mirror, and reduces the amount of light passing through. This results in a higher intensity of the reflected light when it is reflected on the surface of the metal coating and is collected by the imaging optical components in the oblique dark-field scattering system. As the direction of the illumination is asymmetric about the axis around which the Janus bead rotates, changes in the orientation of the metallic coating lead to corresponding changes in the effective area of the metallic scattering of the illumination light. When the coating is oriented at an angle where the scattering cross-section is large, more light is reflected into the angle that corresponds to the N.A. of imaging system, giving rise to an increase in the intensity in the image of the bead (Figure 4.3c, indicated by the bigger orange arrows). When the coating is oriented at an angle where the scattering cross-section is small, less scattered light can be collected by the given N.A. of the imaging system resulting in a decrease in the intensity in the image of the bead (Figure 4.3d, indicated by smaller orange arrows). To experimentally verify the above interpretation, a TMR (tetramethylrhodamine)-streptavidin conjugated Janus bead, fabricated from a 2.8-μm diameter M270 superparamagnetic bead (Invitrogen), is rotated about the optical axis of

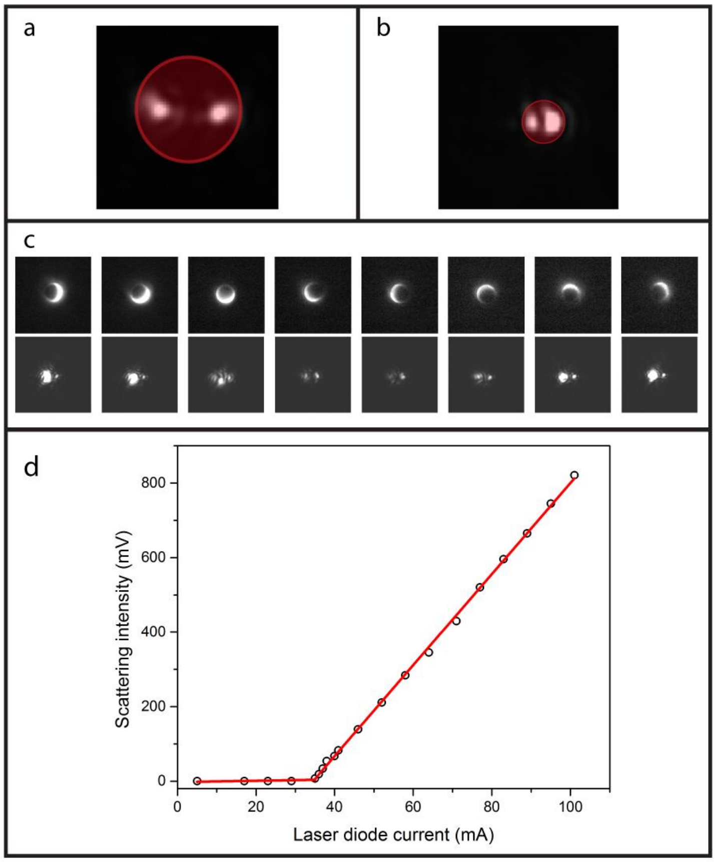

Figure 4.5 Images of uncoated and coated microspheres observed using oblique dark-field scattering and their linear intensity output controlled by the laser diode intensity. A 2.9 μm diameter silica bead (a) and a 1 μm diameter polystyrene bead (b) are imaged using oblique dark-field scattering system. The shaded areas enclosed by red circles indicate the position of the beads. The two bright areas in each bead were consisted with the simulation prediction (Figure 4.4). (c) The intensity of the asymmetric dark-field scattering depends on the angular orientation between the aluminum coating and the axis of illumination. The top row shows images of the TMR-streptavidin-conjugated Janus bead fabricated from a 2.8μm diameter M270 super-paramagnetic bead recorded using epi-fluorescence. In the bottom row the scattering images of the same particle at the corresponding phase angle are depicted. The illuminating light is coupled into the microscope objective and incidental onto the bead from the left in all images. The bead is attached to the substrate and rotated via a mechanical rotation stage.

the microscope objective, using a custom-designed rotation stage, the intensity of the scattering images changes in correspondence to the phase change of the bead. The intensity profile is sensitive to the position of the coating on the bead undergoing rotation. The position of the coating relative to the rotation axis is similar to that depicted in the Figure 4.3c and Figure 4.3d. We observed that when the upper hemisphere of the bead was enclosed by the metal coating, and the coating is rotated to an orientation facing away from the incident illumination light, it internally reflects back most of the light ($\hat{e}_3$ in Figure 4.3a). In such cases, under the condition that the refracted light ($\hat{e}_5$ in Figure 4.3a) was also within the collectable angle of the imaging system without being blocked by the coating, the overall intensity was brighter when the coating faced away from the illuminating light than when the coating faced toward the illuminating light, giving rise to a second peak in one period of rotation. At a given angle, the intensity of the bead increases linearly with the intensity of laser diode and can be tuned by current output of the driver circuit for the laser diode (Figure 4.4d).

To demonstrate its potential use in the biological studies, we tethered a TMR-streptavidin-conjugated Janus bead, fabricated from a 2.8-μm diameter M270 superparamagnetic bead, to a biotin-BSA molecule and observed its rotation by using the electromagnetic tweezers system described in the previous two chapters (Figure 4.6). The experiment was conducted in a similar manner to the DNA-tethered assay described in Chapter 3. In brief, BSA was conjugated to biotin-x-cadaverine (Life Technologies, B1596) by using carbodiimide compound-mediated reaction (detailed in experimental section in Chapter 3). Biotin-BSA was adsorbed to the glass substrate in the flow chamber and then the surface was passivated by 1mg/ml casein. TMR-streptavidin-conjugated

Janus bead was flown into the flow chamber to conjugate to biotin-BSA molecules, and unbound beads were washed out of the chamber by PBS buffer. The quadrupole

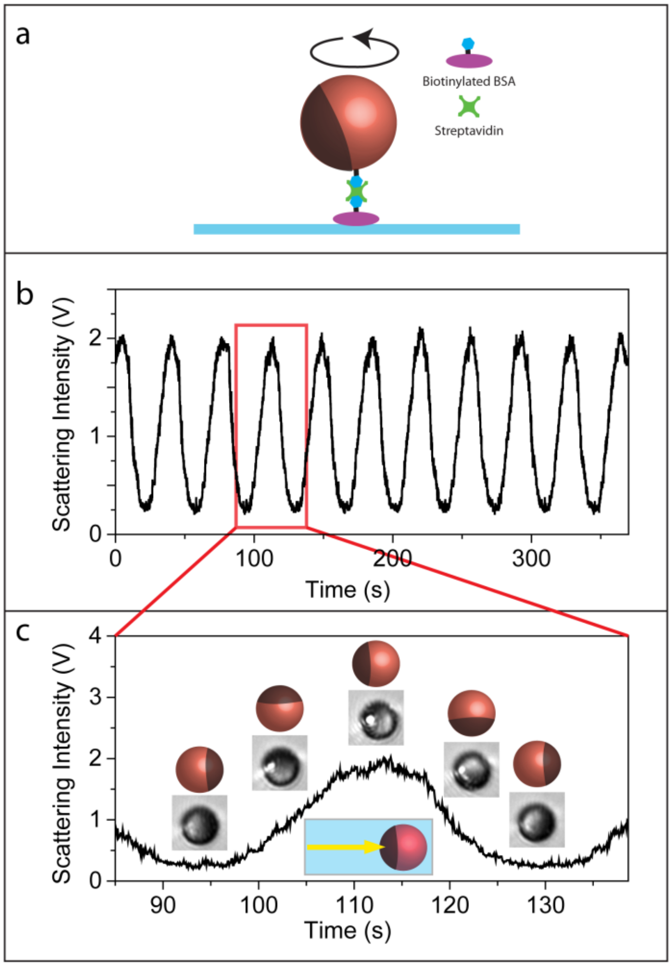

Figure 4.6 Using oblique dark-field scattering to detect rotational motion of single molecules. (a) The illustrative of using oblique dark-field scattering of a Janus bead to detect the rotary motion. The Janus bead is continuously rotated by electromagnetic tweezers. (b) Time trace of the scattering intensity collected by the photodiode. The intensity of the bead displays periodic in-phase change in correspondence with the angular orientation of the bead undergoing rotation. (c) A zoom-in of the time trace showing approximately one period of rotation. The bright-field images collected by the microscope show that the intensity of the bead reached maximum when the metal-coating faced toward the illuminating light and reached minimum when the metal-coating faced away from the illuminating light. The illuminating light is directed toward right (yellow arrow) in the 2D projection, sharing a configuration resembling Figure 4.3c.

electromagnetic torque tweezers were turned on to apply continuous, slowly rotating motion to the conjugated superparamagnetic bead. The result showed that the dark-field scattering intensity of the bead collected by the photodiode displayed periodic, in-phase changes corresponding to the angular orientation of the bead undergoing rotation. The bright-field image collected by the microscope tube lens showed that the intensity of the bead reached maximum when the metal-coating faced toward the illuminating light, reflecting most of the light into the collecting aperture of the imaging system. The intensity reached a minimum when the metal-coating faced away from the illuminating light, letting most energy of the light pass through the relatively transparent medium in the superparamagnetic bead without significant scattering within the collectible angle of the imaging system.

4.4 Conclusions

In summary, we have developed a method that enables us to directly record the angular displacement of particles undergoing rotational motion by using asymmetric illumination of optically anisotropic beads. When combined with an optoelectronic system to detect the scattering signal of the illuminated beads, this direct mapping of angular displacements of the Janus bead to the electrical signal in the oblique dark-field scattering method obviates image acquisition and image processing procedures commonly used in previous studies, and it has the potential to significantly enhance the bandwidth of detection. The use of the near infrared wavelength for illumination also leaves the optical paths intact for fluorescence microscopy, allowing the method to be used in combination with the normal fluorescence for study fluorescently labeled biological molecules. When the Janus bead is conjugated to biological molecules such as proteins and nucleic acids, the oblique dark-field scattering can be used to determine the angular displacement of the biological molecule. The potential implementation of this rotational tracking method in combination with electromagnetic tweezers can possibly allow one to extract high bandwidth torsional mechanical properties and dynamics of molecules such as nucleic acids, such as double-stranded DNA molecules, or proteins, such as ATP synthases. When further combined with fluorescence microscopy, this instrument can potentially allow one to study the effect of torsional stress applied to proteins or nucleic acid on the kinetic property of biological processes, such as ATP synthesis rate in ATP synthase[34–37] or DNA tracking motors translocating along DNA molecules[38–40].

4.5 Bibliography

1. Lipfert, J., Kerssemakers, J. J. W., Rojer, M. & Dekker, N. H. A method to track rotational motion for use in single-molecule biophysics. *Rev. Sci. Instrum.* **82,** (2011).
2. Janssen, X. J. A. *et al.* Torsion Stiffness of a Protein Pair Determined by Magnetic Particles. *Biophys J* **100,** 2262–2267 (2011).
3. Celedon, A. *et al.* Magnetic tweezers measurement of single molecule torque. *Nano Lett* **9,** 1720–5 (2009).
4. Yoshida, M., Muneyuki, E. & Hisabori, T. ATP synthase — a marvellous rotary engine of the cell. *Nat. Rev. Mol. Cell Biol.* **2,** 669–677 (2001).
5. Stock, D., Gibbons, C., Arechaga, I., Leslie, A. G. & Walker, J. E. The rotary mechanism of ATP synthase. *Curr. Opin. Struct. Biol.* **10,** 672–679 (2000).
6. Sowa, Y. *et al.* Direct observation of steps in rotation of the bacterial flagellar motor. *Nature* **437,** 916–919 (2005).
7. Sowa, Y. & Berry, R. M. The Rotary Bacterial Flagellar Motor. *Compr. Biophys. Vol 8 Bioenerg.* (2011).
8. Bates, A. D. & Maxwell, A. *DNA Topology*. (OUP Oxford, 2005).
9. Doering, C., Ermentrout, B. & Oster, G. Rotary DNA motors. *Biophys. J.* **69,** 2256–2267 (1995).

10. Harada, Y. *et al.* Direct observation of DNA rotation during transcription by Escherichia coli RNA polymerase. *Nature* **409,** 113–5 (2001).
11. Cheezum, M. K., Walker, W. F. & Guilford, W. H. Quantitative comparison of algorithms for tracking single fluorescent particles. *Biophys J* **81,** 2378–88 (2001).
12. Lipfert, J., Kerssemakers, J. J. W., Rojer, M. & Dekker, N. H. A method to track rotational motion for use in single-molecule biophysics. *Rev Sci Instrum* **82,** 103707 (2011).
13. Sönnichsen, C. & Alivisatos, A. P. Gold Nanorods as Novel Nonbleaching Plasmon-Based Orientation Sensors for Polarized Single-Particle Microscopy. *Nano Lett.* **5,** 301–304 (2005).
14. Enoki, S. *et al.* High-Speed Angle-Resolved Imaging of a Single Gold Nanorod with Microsecond Temporal Resolution and One-Degree Angle Precision. *Anal. Chem.* **87,** 2079–2086 (2015).
15. Wang, G., Sun, W., Luo, Y. & Fang, N. Resolving Rotational Motions of Nano-objects in Engineered Environments and Live Cells with Gold Nanorods and Differential Interference Contrast Microscopy. *J. Am. Chem. Soc.* **132,** 16417–16422 (2010).
16. Gu, Y., Sun, W., Wang, G. & Fang, N. Single Particle Orientation and Rotation Tracking Discloses Distinctive Rotational Dynamics of Drug Delivery Vectors on Live Cell Membranes. *J. Am. Chem. Soc.* **133,** 5720–5723 (2011).
17. Sonka, M., Hlavac, V. & Boyle, R. *Image Processing, Analysis, and Machine Vision*. (Cengage Learning, 2014).
18. Anthony, S. M. & Granick, S. Image Analysis with Rapid and Accurate Two-Dimensional Gaussian Fitting. *Langmuir* **25,** 8152–8160 (2009).
19. Rioux, M. & Domey, J. Lateral effect photo-diode - a new technique to obtain position signals. *Appl. Opt.* **21,** 3618–3619 (1982).
20. Smith, S. B., Cui, Y. & Bustamante, C. Overstretching B-DNA: the elastic response of individual double-stranded and single-stranded DNA molecules. *Science* **271,** 795–9 (1996).
21. Svoboda, K., Schmidt, C. F., Schnapp, B. J. & Block, S. M. Direct observation of kinesin stepping by optical trapping interferometry. *Nature* **365,** 721–7 (1993).

22. Allersma, M. W., Gittes, F., deCastro, M. J., Stewart, R. J. & Schmidt, C. F. Two-dimensional tracking of ncd motility by back focal plane interferometry. *Biophys J* **74,** 1074–85 (1998).
23. Visscher, K., Gross, S. P. & Block, S. M. Construction of multiple-beam optical traps with nanometer-resolution position sensing. *IEEE J. Sel. Top. Quantum Electron.* **2,** 1066–1076 (1996).
24. Schneckenburger, H. Total internal reflection fluorescence microscopy: technical innovations and novel applications. *Curr. Opin. Biotechnol.* **16,** 13–18 (2005).
25. Axelrod, D., Thompson, N. L. & Burghardt, T. P. Total internal reflection fluorescent microscopy. *J. Microsc.* **129,** 19–28 (1983).
26. Spencer, M. *Fundamentals of Light Microscopy*. (CUP Archive, 1982).
27. Bohren, C. F. & Huffman, D. R. *Absorption and Scattering of Light by Small Particles*. (John Wiley & Sons, 2008).
28. Hulst, H. C. van de. *Light Scattering by Small Particles*. (Courier Corporation, 2012).
29. Yu, H., Shen, J. & Wei, Y. Geometrical optics approximation for light scattering by absorbing spherical particles. *J. Quant. Spectrosc. Radiat. Transf.* **110,** 1178–1189 (2009).
30. Ungut, A., Grehan, G. & Gouesbet, G. Comparisons between geometrical optics and Lorenz-Mie theory. *Appl. Opt.* **20,** 2911–2918 (1981).
31. Liou, K. N., Takano, Y. & Yang, P. On geometric optics and surface waves for light scattering by spheres. *J. Quant. Spectrosc. Radiat. Transf.* **111,** 1980–1989 (2010).
32. Hecht, E. *Optics*. (Addison-Wesley, 2002).
33. Ma, X. *et al.* Determination of complex refractive index of polystyrene microspheres from 370 to 1610 nm. *Phys. Med. Biol.* **48,** 4165 (2003).
34. Deckers-Hebestreit, G. & Altendorf, K. The F_0F_1-type ATP synthases of bacteria: structure and function of the F_0 complex. *Annu. Rev. Microbiol.* **50,** 791–824 (1996).
35. Martin, J., Hudson, J., Hornung, T. & Frasch, W. D. Fo-driven Rotation in the ATP synthase Direction Against the Force of F1ATPase in the F_0F_1 ATP synthase. *J. Biol. Chem.* jbc.M115.646430 (2015).

36. Pänke, O., Cherepanov, D. A., Gumbiowski, K., Engelbrecht, S. & Junge, W. Viscoelastic dynamics of actin filaments coupled to rotary F-ATPase: angular torque profile of the enzyme. *Biophys. J.* **81,** 1220–1233 (2001).
37. Ma, W. & Schulten, K. Mechanism of Substrate Translocation by a Ring-Shaped ATPase Motor at Millisecond Resolution. *J. Am. Chem. Soc.* **137,** 3031–3040 (2015).
38. Ma, J., Bai, L. & Wang, M. D. Transcription Under Torsion. *Science* **340,** 1580–1583 (2013).
39. Skinner, G. M., Baumann, C. G., Quinn, D. M., Molloy, J. E. & Hoggett, J. G. Promoter binding, initiation, and elongation by bacteriophage T7 RNA polymerase. A single-molecule view of the transcription cycle. *J Biol Chem* **279,** 3239–44 (2004).
40. Lebel, P., Basu, A., Oberstrass, F. C., Tretter, E. M. & Bryant, Z. Gold rotor bead tracking for high-speed measurements of DNA twist, torque and extension. *Nat Meth* (2014).

Chapter 5

A NOVEL DUAL-COLOR BIFOCAL IMAGING SYSTEM FOR SINGLE-MOLECULE STUDIES

In this chapter, I will present the design and implementation of a novel dual-color bifocal imaging system that is capable of acquiring two spectrally distinct images that are either spatially identical or focal-shifted with respect to each other. This was achieved by splitting an image into two channels according to their distinct emission spectra and independently focusing both images simultaneously onto a single CCD camera. I will first give an overview of the existing methods and commercially available equipment that are intended to achieve similar goals and their limitations. Then I will present the optical path design and mechanical implementation of the device. The sub-pixel registration and ultra-low relative mechanical drift between the two channels will be characterized. The dual-color imaging feature will be demonstrated by imaging biomolecules labeled with spectrally different dyes and the bifocal imaging feature will be presented by focusing two separate channels on micro-/nano-spheres at different focal planes. Discussions and conclusions will be framed to show the potential use of this device in single-molecule fluorescence microscopy.

5.1 Introduction

Dual-color fluorescence microscopy advanced our understanding about cellular and molecular dynamics[1–3], protein co-localization[4], and protein-protein interaction[5,6]. The capability of monitoring two different dyes at the same time with high spatial resolution is required in a variety of applications. For example, in FRET (Förster resonance energy transfer) measurements, a powerful tool to investigate the dynamics of macromolecular machines by detecting nanoscale conformational changes as well as binding events, the intensity of a pair of donor and acceptor fluorophores are measured simultaneously. FRET is based on an interaction occurring between two fluorophores in close proximity (10-90 Å), where excited-state energy from a donor fluorophore is partially transferred to a nearby acceptor through non-radiative dipole–dipole coupling, leading to fluorescence emission of the acceptor accompanied by partial quenching of the donor, resulting in an intensity decrease of donor fluorophore and an intensity increase of acceptor fluorophore[7–9]. The efficiency of this energy transfer is inversely proportional to the sixth power of the distance between donor and acceptor, making FRET extremely sensitive to small changes in distance.

In general dual-color imaging methods image the sample that contains two spectrally different fluorophores separately by splitting the emitted signal according to their wavelength into two channels, and then focusing these two channels separately on to the same camera or two different cameras. This simultaneous visualization of two spectrally distinct wavelengths emitted from a sample is usually achieved by chromatically split emitted beam into two components by dichroic mirrors. Kinosita et al. implemented dual-color imaging system by inserting dichroic mirrors internally within a microscope between a microscope objective and a microscope tube lens to split two wavelengths and then use the single tube lens to image two wavelengths onto the same CCD camera[2]. Prabhat et al. split the emitted light collimated by the microscope objective into two paths and in each path used a separate tube lens and a camera to image each distinct wavelength[10].

Multifocal plane microscopy is a related technique that uses a mechanically resembling design. This method has the capability of three-dimension particle tracking. Several multifocal designs have been developed and implemented to study dynamics of recycling pathway of protein receptor[11], vesicles in living adipocytes[12], and phagocytosed nanospheres[13] *in vivo*. In a bifocal imaging device, the image is split into two pathways with different effective path length to create two images with relative focal shift with respect to each other. Toprak et al. used spherical aberration and diffraction in the out-of-focus image of fluorescent particles that give rise to the ring patterns around particles to track the z-position of the particles[13]. Sun et al split an image into two channels by a pair of closely spaced, nearly parallel mirrors placed at a plane that is conjugate to the objective back focal plane, and translates the change in z-position to a relative lateral shift in the two images of two corresponding channels[12].

Combining bifocal imaging with dual-color imaging, presents the opportunity to acquire spectrally distinct images without the drawbacks of commercial dual-color imaging systems. What is in common between the dual-color imaging and bifocal-plane imaging methods is that, in both methods, one needs to determine the spatial relationship between the two images in two separate channels either in focused and defocused form. Thus, the implementation of the simultaneous dual-color and bifocal imaging with the capability of focusing spectrally and spatially distinguished images onto the same CCD camera remains challenging and has yet to be developed. We developed a novel device that combines the dual-color imaging and bifocal imaging methods to achieve truly simultaneous dual-color and bifocal-plane imaging (DBI) with a single CCD camera. We demonstrate that two spatially identical images with distinct emission spectra are able to be simultaneously acquired by a single camera, while the two channels can be independently and continuously focused. This guarantees that events recorded on the two channels concur to the time resolution limited by the CCD camera. Diffraction limited applications such as protein co-localization are very sensitive to the registration between the two channels, and newly developed microscopy methodologies such as super-resolution imaging based on stochastic optical reconstruction typically require long-period acquisition. Therefore, channel-registration and long-term relative drift between the two channels are important to the accuracy and applicability of the instrument to biological studies. With our stable mechanical design, we demonstrate that sub-pixel registration and long-term drift between the two channels can be achieved in this DBI, and we show its application to biophysical studies.

5.2 Design and Implementation of the Dual-color Bifocal Imaging System

A dual-color bifocal imaging device allows the simultaneous visualization of two different wavelengths emitted from a sample and allows manipulation of focus in each channel independently. For high temporal fidelity in the observation of dynamic processes, it is best to image the two wavelengths on two halves of the same CCD chip. On the other hand, for high spatial fidelity, it is required that the two images can be accurately aligned with each other[14]. An essential requirement is that the two wavelengths be properly focused with minimal optical aberrations. For example, two wavelength components are

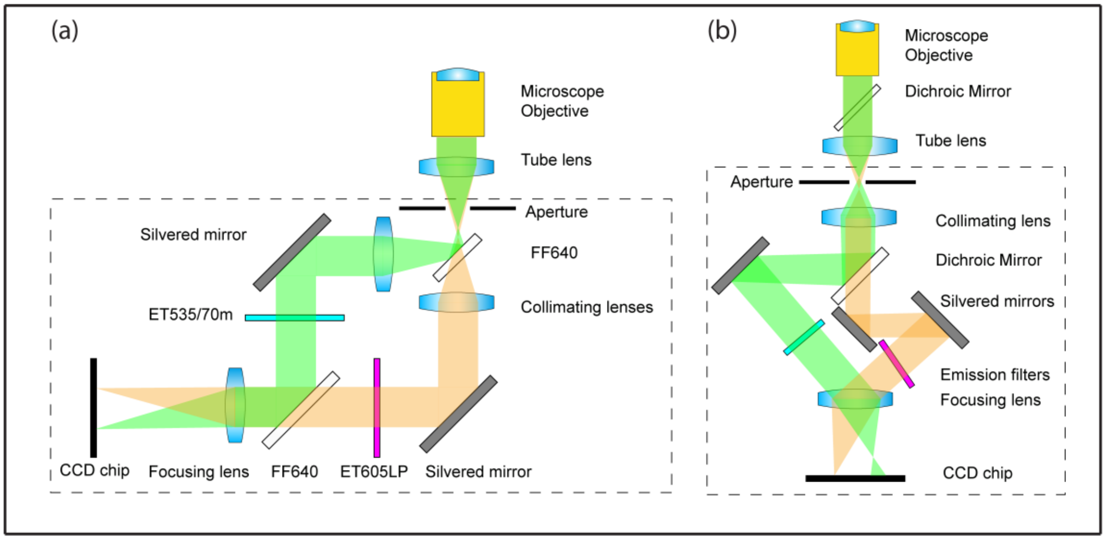

Figure 5.1 Schematic comparison of the dual-color bifocal imaging systems. (a) Schematic of the customized dual-color imaging system with the capability of independently adjusting the focus of two channels. Two images with distinct spectra are split by a dichroic mirror and then independently collimated by two collimating lenses. The lateral position of two collimating lenses can be adjusted separately so that the two images are independently placed at the focal planes of their respective collimating lenses with high precision. The focusing lens focuses two images onto the two halves of the CCD chip, resulting in two focused images on both channels. (b) The schematic of a commercial dual-color imaging system with one collimating lens and one focusing lens shared by both color-channels. The focus of the two images in the two channels cannot be independently adjusted. Schematics are adapted from Dr. Kaul's dissertation (Ref 14).

usually subject to the chromatic aberration in a microscope optical system when using a high numerical aperture (N.A.) objective lens, which is commonly employed in objective-type total internal reflection fluorescence microscope (TIRFM), resulting in an offset between the focal planes of corresponding wavelengths along the optical axis before they enter the externally implemented dual-color imaging device (Figure 5.1 b). For example, commercial devices such as the DV2 multichannel imaging system (Photometrics Inc.) use a single collimating lens placed behind the focal plane of the microscope tube lens to collimate the emitted light. This single collimating lens is not able to accommodate both wavelengths due to the offset between the focal planes of the two wavelengths, resulting in the compromise in the simultaneous collimation of both wavelength components. This error in collimation gives rise to either a convergence in the shorter wavelength or a divergence in the longer wavelength, leading to a slightly out-of-focus image of one wavelength when the other wavelength is in focus on the CCD camera.

In our DBI, fluorescent light emitted from the sample and imaged by the microscope is shuttered by an aperture composed of two blades. The aperture is placed in the focal plane of the microscope tube lens, allowing only part of the image collected by the microscope that corresponds to the area of half of the CCD chip of the camera to enter the DBI optical system. The partially-shuttered image is split by an imaging-flat dichroic beamsplitter (FF640, Semrock Inc.) into two images with distinct spectra, and then independently collimated by two collimating lenses (Figure 5.1 a). The position of these two collimating lenses can be adjusted separately along optical axis so that the two spectrally distinct images are independently placed at the focal planes of their respective collimating lenses with high precision. After this, the two wavelength components are reflected into the right position using silvered mirrors. In the long-wavelength channel the collimated light passes through emission filter ET605LP (Chroma Technology Corp), and in the short-wavelength channel, the light passes through emission filter ET535/70m (Chroma Technology Corp). Then the collimated light beams in the two channels are combined by a second common dichroic beamsplitter. Finally, a focusing lens focuses the collimated light onto the two halves of a CCD chip, resulting in two focused images on a single CCD camera.

All the optical components were housed in a light-tight aluminum chamber that can be mounted under a microscope optical table (Figure 5.2). The components that mount the dichroic mirrors, silvered mirrors and lenses were modularized to facilitate the convenient access to and the potential exchange of the optical components without major disassembly

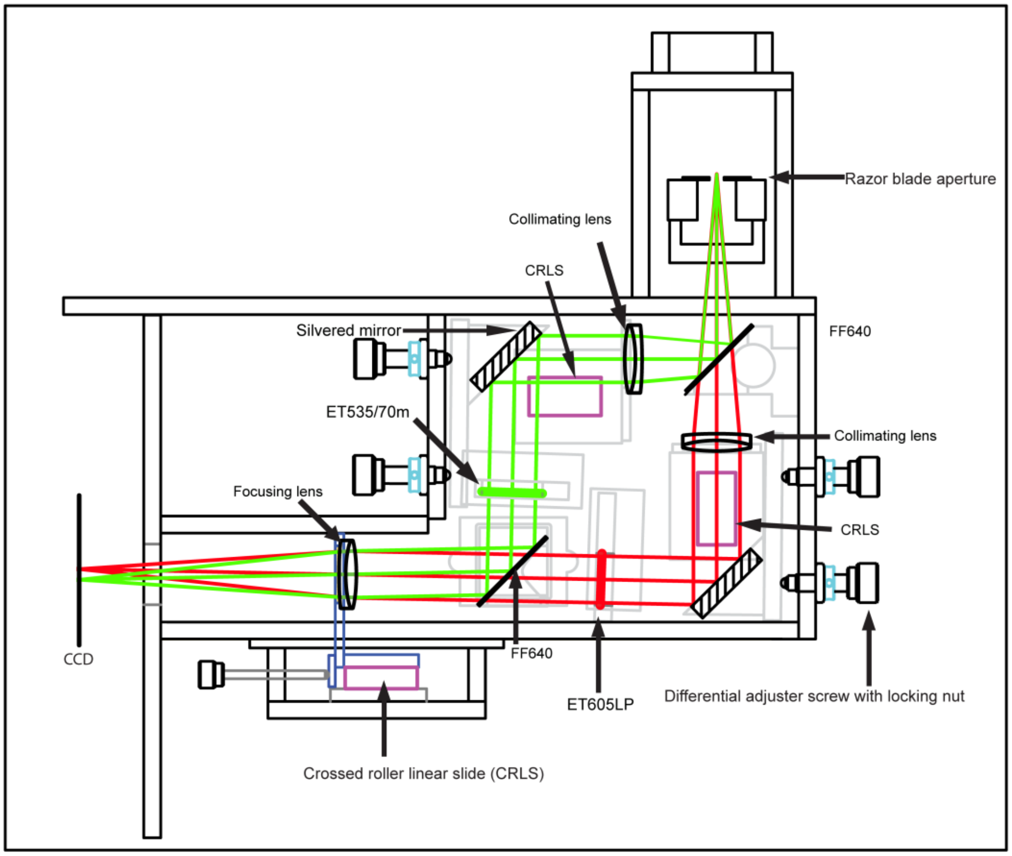

Figure 5.2 Mechanical drawing of the dual-color bifocal imaging system with ray tracing Zmax simulation. An aperture consisting of two razor blades are placed at a plane conjugate to the image plane of the microscope system. The image is split by a dichroic beamsplitter (FF640) into two images with distinct spectra and then independently collimated by two collimating lenses mounted on a crossed roller linear slide assemblies (colored magenta). The angle of the silvered mirrors can be adjusted by a tip-tilt mechanism based on the motion of three differential adjuster screws. The focusing lens focuses two images onto the two halves of the CCD chip, resulting in two focused images in both channels. The ray tracing simulated optical path of longer-wavelength is colored in red, and that of the shorter wavelength is colored in green.

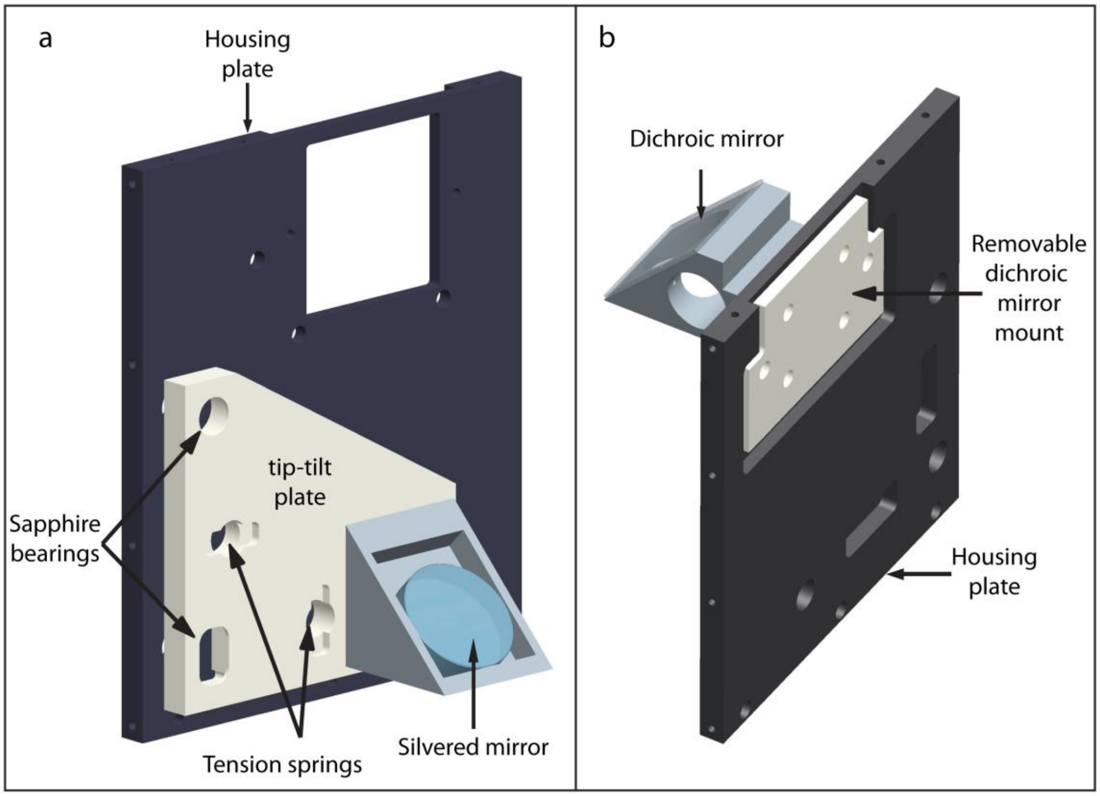

Figure 5.3 Mechanical designs of tip-tilt mechanism for silvered mirror adjustment and dichroic mirror holder. (a) Tip-tilt adjustment mechanism for silvered mirrors. The angle of the silvered mirrors can be adjusted by adjusting the position and angle of the tip-tilt plate, via the motion of three differential adjuster screws that are located at the three apical points of a triangle. The screws push on the sapphire bearings against two extension springs behind the tip-tilt plate. Position of two sapphire bearings are indicated in the figure, and the third one is behind the holder of the silvered mirror. (b) Removable mount holding the dichroic mirror is positioned against the housing plate with dowel pins to ensure repeatable mounting. The modularized design facilitates the exchange of the dichroic mirror when a different beamsplitter for a different wavelength is needed.

of the whole device (detailed in Ref 14). The collimating lens of each channel is mounted on a crossed roller linear slide (CRLS) assembly (RDA-1, Del-Tron Precision, Inc.) and its position can be adjusted along the optical axis by a 100TPI micrometer adjuster (F19SS150, Thorlabs Inc.). The angle of the silvered mirrors can be adjusted by a tip-tilt mechanism based on the motion of three differential adjuster screws (DAS110, Thorlabs

Inc.), located at three apical points of a triangle shape, pushing on sapphire bearings against two extension springs behind the tip-tilt. Each differential adjuster screw has a fine adjustment mechanism that enables a displacement of 25 µm/rev. The stiff tension springs that pull the mounting plate of silver mirrors against the adjuster screws improve the mechanical stability and reduce long-term drift of the silver mirrors. Removable mounts holding the two dichroic beam splitters are positioned against the housing chamber with dowel pins as kinematic stops to ensure repeatable mounting. If desired, new dichroic beam-splitters for a different pair of wavelengths can conveniently be switched out in this style of modular assembly. The emission filters can also be switched out in a similar fashion.

5.3 Mechanical Characterization of the Dual-color Bifocal Imaging System

We quantified the registration by measuring the position of 250nm beads whose emission spectra overlap with those of both channels. The image of the beads is split by DBI into two chromatically distinguished images placed side by side on the same CCD chip (Figure 2a). Registration between the two channels is evaluated by measuring the difference in x- and y- coordinates for the same bead in two separate channels. The position of each bead is calculated as the peak position of the 2D Gaussian function fitted to the bead intensity profile (Figure 2b). The offset is calculated as the difference between the positions of the Gaussian peak of each bead in two channels. As shown in Figure 2d, an offset of less than one pixel (64.5nm) between the two channels for both x and y coordinates demonstrates excellent registration of the two channels in our imaging system. We also evaluated the registration by calculating the affine transformation matrix that maps

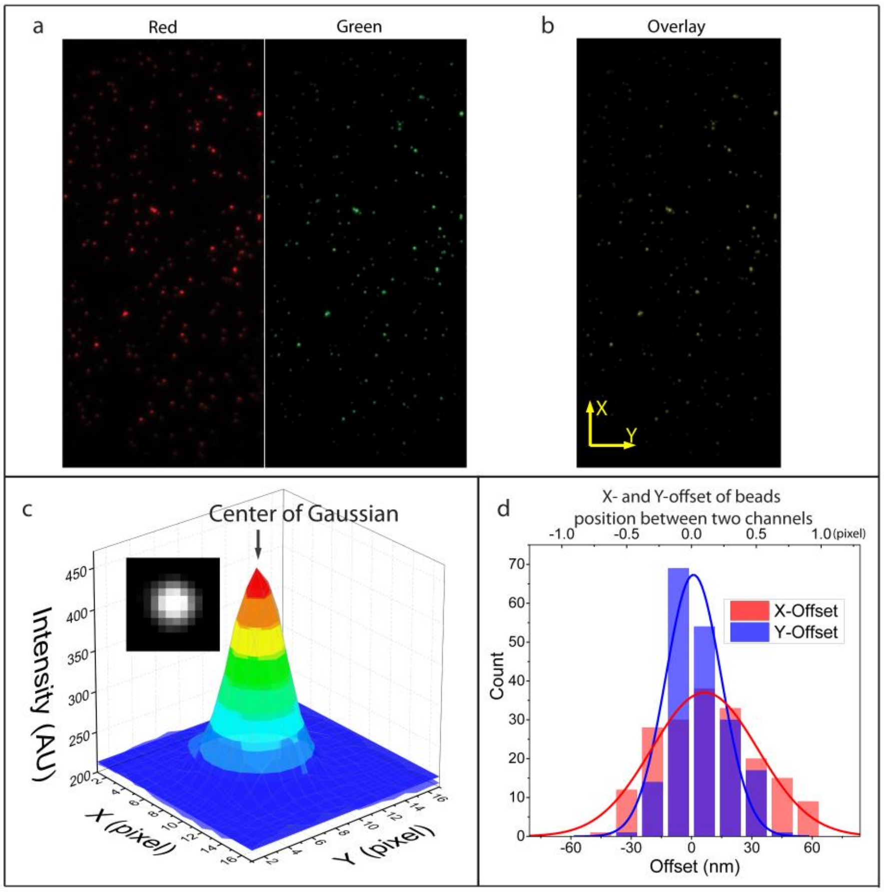

Figure 5.4 Customized dual-color imaging system allows sub-pixel registration between two channels. (a) Sub-pixel registration between two channels is achieved by imaging fluorescent, 250nm beads with emission spectra overlapping in both channels. The long-wavelength spectrum of the image is focused on one half of the CCD chip of the camera (beads pseudocolored in red), and the short-wavelength spectrum of the image is focused on the other half of the CCD chip (beads pseudo-colored in green). (b) Two halves of the image acquired by CCD camera are overlaid. The beads in two channels precisely overlap with each other to demonstrate the images in two channels are registered with each other with high precision. (c) Inset is a sample of a cropped bead image captured by the CCD camera. A Gaussian function is fitted to the bead's intensity profile, shown as a mesh overlay in the plot. The center of the Gaussian function determines the position of the bead. (d) A histogram of the translational offset of the same bead's position between two channels shows sub-pixel registration between two channels.

the two-dimensional coordinates of the beads in bottom channel (x,y) into top channel (u,v) by:

$$\begin{bmatrix} u \\ v \\ 1 \end{bmatrix} = A \begin{bmatrix} x \\ y \\ 1 \end{bmatrix} = TRS \begin{bmatrix} x \\ y \\ 1 \end{bmatrix} = \begin{bmatrix} a & b & c \\ d & e & f \\ 0 & 0 & 1 \end{bmatrix} \begin{bmatrix} x \\ y \\ 1 \end{bmatrix},$$

where matrix A is the affine matrix that maps bead coordinates. If we only consider translation (T), rotation (R) and scaling factor (S), rotation and scaling factor is convolved into RS matrix:

$$RS = \begin{bmatrix} a & b \\ d & e \end{bmatrix} = \begin{bmatrix} 0.99907 & 0.00153 \\ -0.00057 & 0.99949 \end{bmatrix}.$$

The resulting matrix is very close to an identity matrix. It shows that the two images are well registered to each other to sub-pixel accuracy. We noticed that choosing dichroic beamsplitters of imaging-flat flatness-grade is essential for image registration accuracy (nominal radius of curvature ~100 meters; information provided by Semrock Inc.). The standard-flat (~6 meters) or laser-flat (~30 meters) beamsplitters lead to nearly an order of magnitude of worsened relative distortion between two channels. Ultimately, further improvement of registration can be achieved by computational methods such as local weighted mean mapping[15,16]. Despite improvements in image registration can be achieved by computational methods, mechanical drifting can still cause misalignment between the two channels over long-period recording. We characterized long-term drift of the system. The relative shift due to mechanical and thermal drifting between two channels over a time-period of 6 hours is ~30nm and remains a fraction of one pixel in our imaging system. This drift is less than the commercial dual-imaging systems that use gear knobs for adjusting reflective mirrors instead of the tip-tilt mechanism presented above that uses tensional

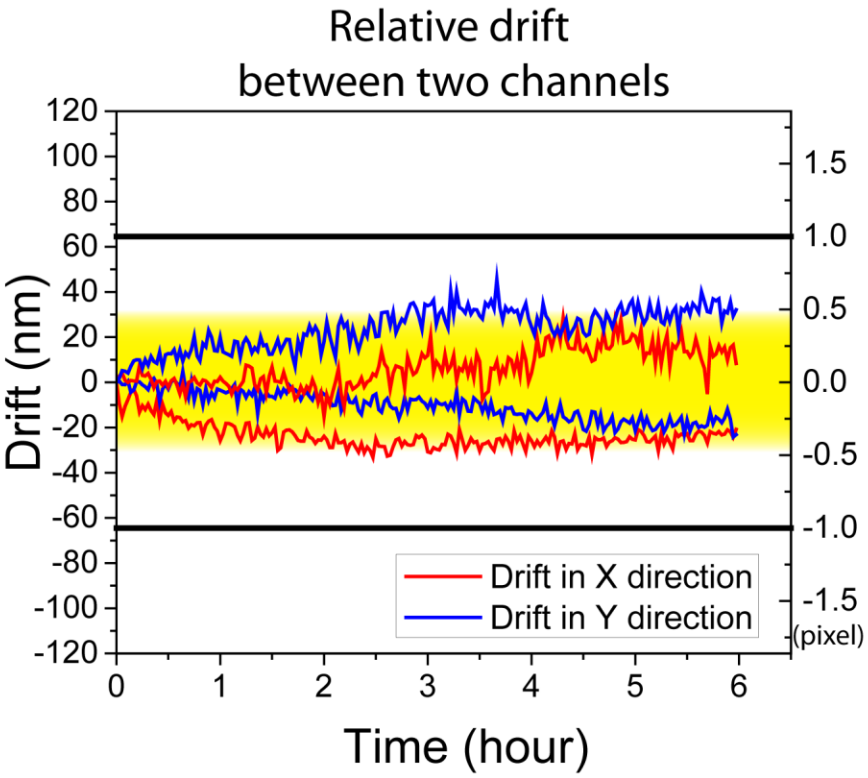

Figure 5.5 Long-term relative drift between the two channels. Long-term relative drift between the two channels shows subpixel drifts on the order of hours.

spring with high stiffness combined with fine adjustment screws to improve mechanical stability.

5.4 Characterization of the Dual-Color Bifocal Imaging System

To demonstrate the dual-color imaging feature of our DBI, we conducted a microtubule-kinesin binding assay. Microtubules are a component of the cytoskeleton and found through the cytoplasm. They are 25nm-diameter, long hollow tubular assemblies of protofilaments formed by the polymerization of a dimer of two globular proteins, α- and β- tubulin, in the presence of guanosine triphosphate (GTP)[17,18]. They are involved in maintaining the structure of the cell as well as make up the internal structure of cilia and flagella. They are essential to many cellular processes including providing platforms for intracellular transport, where they are involved in the movement of secretory vesicles,

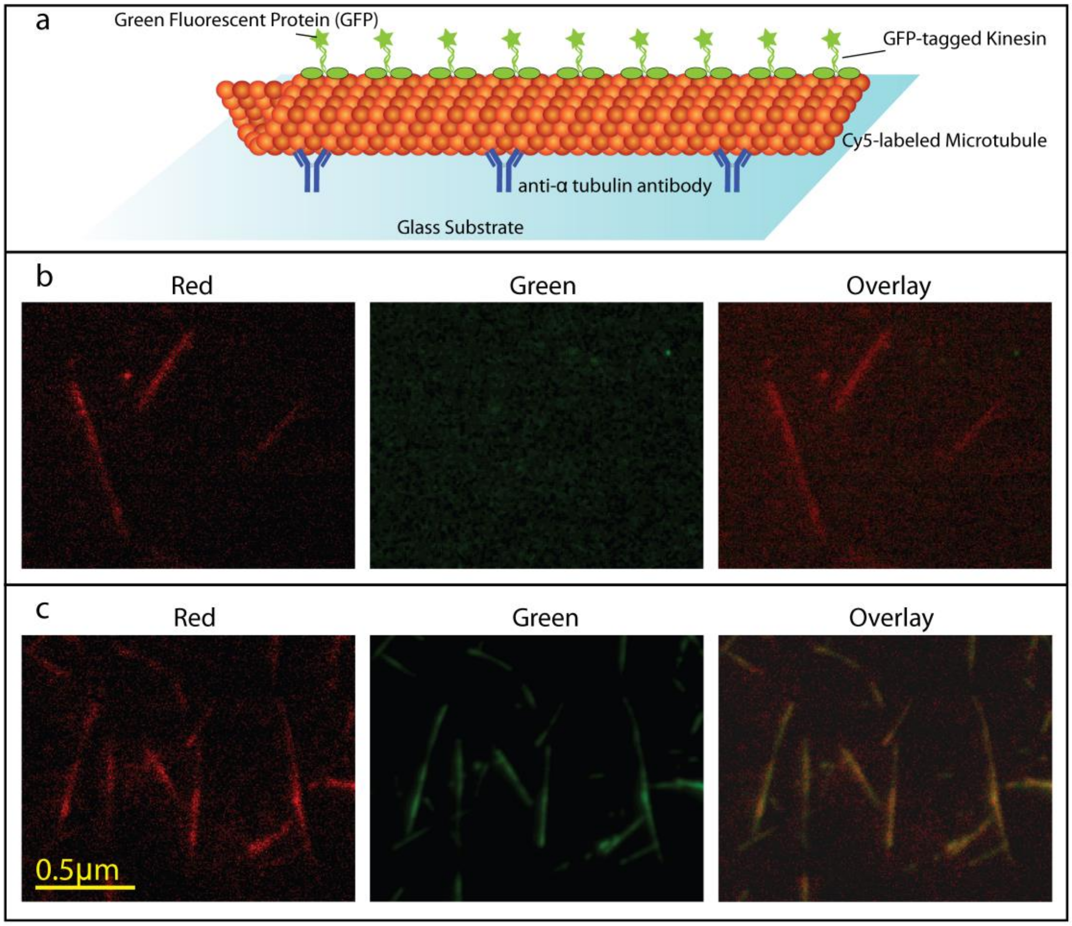

Figure 5.6 Simultaneous imaging of two spectrally distinct dyes demonstrated by a microtubule-kinesin binding assay. (a) Schematic of a microtubule-kinesin binding assay. Cy-5 labeled microtubules are attached to anti-α tubulin antibodies adsorbed on the glass substrate. GFP-labeled kinesin are then introduced to specifically bind to the microtubules in the presence of AMPPNP. (b) Before GFP-tagged kinesin is introduced into the assay chamber, Cy-5 labeled microtubules alone (pseudo-colored in red) can be visualized in the long-wavelength channel (Red). The spectrum of the Cy-5 dye is cut off in the short-wavelength channel (Green). The overlay of the two channels shows only the presence of microtubules. (c) After GFP-tagged kinesin is introduced into the chamber, microtubules are still imaged only in long-wavelength channel (Red). The GFP-kinesins bind to microtubules in the presence of AMPPNP and are imaged only in the short-wavelength channel (Green). An overlay of the two images shows accurate registration and simultaneous focus of the two channels.

organelles, and intracellular macromolecular assemblies. They are also essential to cell division, where they are involed in chromosome sepearation, and are the major components of mitotic spindles, which are used to separate eukaryotic chromosomes[19–21]. Kinesins are nanoscopic motor proteins that support several cellular functions including mitosis, meiosis and transport of cellular cargo[22]. In the presence of adenosine triphosphate (ATP), kinesins walk along microtubules with 8nm steps[23,24]. ATP powers the stepping motion of kinesin. The chemical energy derived from the hydrolysis of ATP in the ATPase domain of kinesin is converted to mechanical work as the motor molecule steps along the microtubule protofilament. In the presence of adenosine 5'-(β,γ-imido)triphosphate (AMPPNP), an ATP analogue, kinesins are locked in position on microtubules when they bind to microtubules[25,26] (Figure 3 a). In the assay, before GFP-kinesins were flowed into the reaction chamber, Cy-5 labeled microtubules were only visible in the long-wavelength channel and no distinctive features were visible in the short-wavelength channel (Figure 3 b-d). After GFP-kinesins were introduced into the chamber, the shape of microtubules became visible in the short-wavelength channel due to the coating of GFP-kinesins bound on these microtubules (Figure 3 e-g). An overlay of the images from the two separate channels showed that the images were well registered with each other and each spectrally distinct image was in focus.

We applied the DBI to a DNA-stretching experiment to demonstrate the usefulness of its bifocal imaging feature in single-molecule force spectroscopy. Mechanical processes and properties play an important role in most biological processes. A range of instruments has been developed for direct and precise measurements of forces and torques applied by biomolecules ranging from proteins to nucleic acids[27–29]. Magnetic tweezers (MT) have been used to study the mechanical property and conformation dynamics of DNA and protein-DNA interaction[30–33]. In all MT experiments, a superparamagnetic bead is conjugated to the biomolecule of interest to serve as a force handle, and a magnetic field is applied to the bead that imparts stretching and twisting forces to the molecule. To report the tensional and torsional statuses of the molecule, either the magnetic bead or an additional rotor bead is imaged and its translational and angular positions are measured[34-37]. However, in the experiments using rotor beads as reporters and in those studying protein-DNA interactions, only the rotor bead or the magnetic bead was monitored while proteins under study were not tracked in real time, partly because they usually lie on different planes along the optical path and cannot be focused at the same time in conventional microscope imaging system. This limitation has been overcome in our DBI design wherein both the magnetic bead and the biomolecule, can be monitored simultaneously in different planes.

In the DNA-stretching assay, a DNA molecule was tethered to a magnetic bead on one end and fixed to the substrate at the other. A small polystyrene bead with a diameter of 250nm was adsorbed to the glass surface via non-specific adsorption as reference for the z-position along the optical axis. When there is no force applied on the bead, the DNA's extension is close to zero due to entropic force and the attached magnetic bead is close to the glass surface (Figure 5.7a). When a sufficiently large magnetic field gradient is applied above the sample region, pulling the big, magnetic bead upward, the extension of the DNA molecule reaches close to its contour length (2.7μm for the given DNA construct of 8 kb pairs). The z-displacement of the big bead from the glass surface corresponds to the contour length (Figure 5.7b). In the absence of applied force, both channels are focused on the small bead, leaving the big bead only slightly out of focus as it hovers near the glass

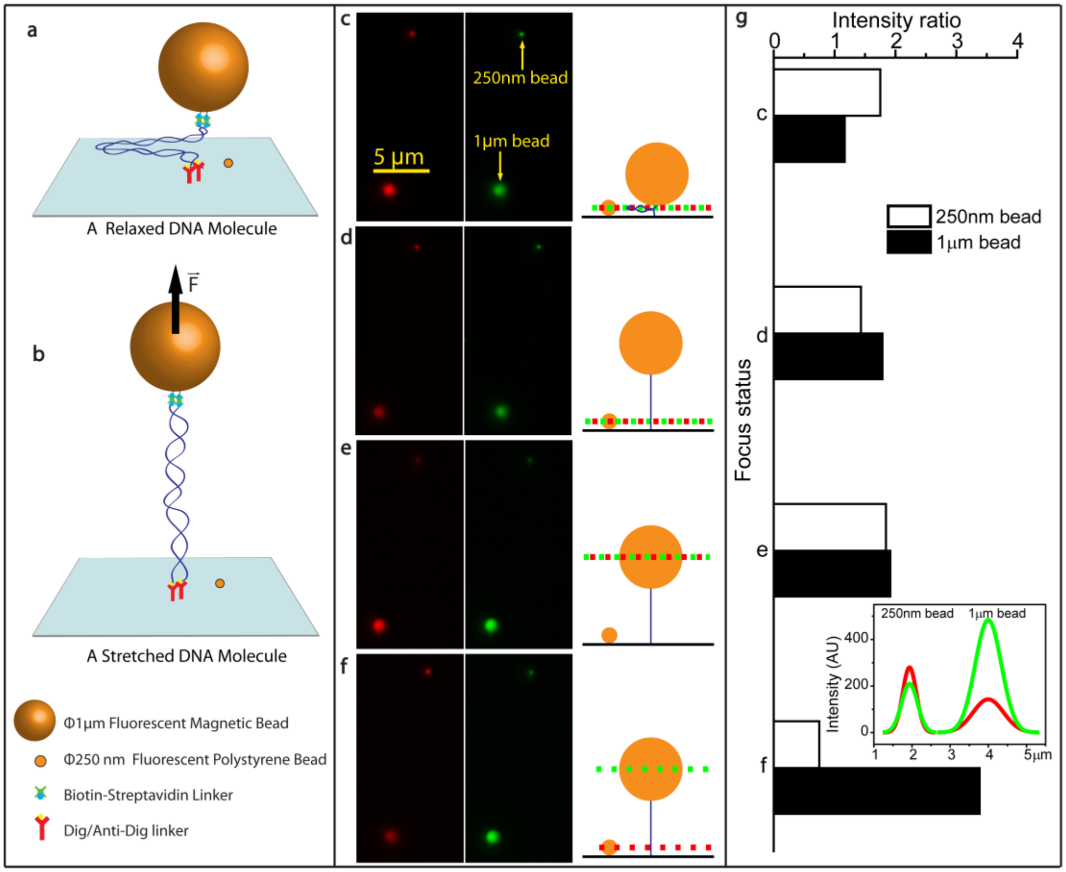

Figure 5.7 Independent focusing capability of two channels as demonstrated by the DNA tethered particle assay. A specially designed DNA construct was attached on one end to the surface of a microscope cover glass, and the other end to a 1μm superparamagnetic fluorescent bead. A 250nm non-magnetic polystyrene bead was non-specifically adsorbed to the glass surface. The 1μm bead was close to the glass surface when no force was applied (a) and was raised by DNA's contour length when the DNA was stretched (b). At different DNA stretching lengths, the two collimating lenses in the two channels were adjusted independently to image different planes in the sample (c-f). Red and green dashed lines indicate correspondingly pseudo-colored planes focused on to the camera in the two channels. In (g), (g) The intensity ratio between green and red channels for the 1μm bead and 250 nm bead at four different DNA-stretching and channel-focusing scenarios (c-f). As an example, the inset figure shows the Gaussian profiles (1D projection of the 2D Gaussian fitting) used to calculate peak intensity in scenario (f).

surface (Figure 5.7c). After a force is applied to pull the big bead upward until the DNA is extended to its contour length, the big bead shifts further out of focus. The collimating lens for the short-wavelength channel can be focused on the big bead (pseudo-colored in green), so two beads at different heights are focused on the CCD chip simultaneously. Alternatively, the plane where the big bead is can be first brought into focus by adjusting the position of the microscope objective, after which the two collimating lenses can be independently adjusted to generate an image where two beads at different heights are focused on the CCD chip simultaneously. In four different DNA-stretching and channel-focusing scenarios, the degree of focus is quantified by fitting the bead intensity profile to a 2D Gaussian distribution (Figure 5.7g inset) and the intensity ratio is calculated by dividing the Gaussian amplitude in the short-wavelength channel by that measured in the long-wavelength channel (Figure 5.7g). A similar intensity ratio for the big and small beads in cases (c), (d) and (e) indicates that both channels are focused to the same sample plane. In case (f), a low intensity ratio for the small bead and a high ratio for big bead show that the two beads are located at different sample planes and are in focus independently in two separate channels.

5.5 Conclusions

We designed and implemented a novel optical system capable of simultaneously imaging spectrally distinct and focally shifted images in the same sample with a single CCD camera. The two separate channels are globally well registered with each other within about 50nm across an area of about 70µm x 35µm, and the long-term mechanical drift between the two channels is below ~30nm over a period of 6 hours. To demonstrate the dual-color imaging feature and the bifocal imaging feature of our device, we conducted two different biological experiments. A kinesin-microtubule binding assay was performed to show that the two channels can separately image two spectrally distinct species of dyes or fluorescent proteins with high registration accuracy. We also performed a DNA-tethered particle assay to simultaneously focus one channel on the force probe and the other channel on a reporter bead located on a different focal plane. Flexibility and stability in the optical and mechanical features of our DBI system make it highly advantageous for performing a diverse range of single-molecule FRET experiments[38–40], and dual-color super-resolution measurements when combined with photoactivated localization microscopy[41]. When integrated with single-molecule force spectroscopy[29,42,43], such as optical tweezers[44–46] or magnetic tweezers[47–50], our DBI can be used to study the influence of direct force and torque applied to DNA molecule on the kinetics of DNA binding proteins, for example, RNA polymerase involved in transcription[51–54] or DNA helicase involved in DNA replication[55–57]. When the device is integrated into TIRFM with proper calibration of fluorescence intensity of particles with respect to their distance from the glass surface, the device can also potentially be used to track three-dimensional motion of microspheres, quantum dots and nanoparticles endocytosed into cells for studies of cellular transport and embryonic cell development[58–60], while simultaneously imaging fluorescently labeled proteins involved in these biological processes in the cell[61,62].

5.6 Experimental Section

Characterization of the registration and long-term mechanical drift

The registration and long-term drift were analyzed by imaging samples using a 100x magnification, high numerical aperture (NA=1.45) microscope objective. All images were acquired by Hamamatsu ORCA-ER camera (nominal CCD cell size 6.45µm). To characterize the accuracy of registration between the two channels, 200nm diameter Nile red beads (Spherotech) were diluted in PBS buffer and flown into a sealed flow chamber.

The flow chamber was constructed as described in Section 3.6. The emission spectrum of Nile Red beads spans over that of both channels so the same bead can be visualized through both channels simultaneously. The beads were nonspecifically adsorbed on the cover glass. To image the beads, we excited them with a 488nm laser using objective total internal reflection microscopy (TIRFM). The two channels were aligned by adjusting the differential adjuster screws (Figure 5.2) and their positions were determined in real-time using a customized Labview algorithm (National Instruments). The center of each bead was calculated by fitting the point-spread function of the bead to a Gaussian function[63] using Equation 3.2.

To evaluate the long-term drift of the two channels with respect to each other, we used bright-field microscopy to image 500nm polystyrene beads deposited in the sample chamber in a similar manner because fluorescent beads suffer from the limitation of a short time scale for photo-bleaching. A cross-correlation function calculates the displacement of the beads between an image $I_{xy}$to a kernel $K_{xy}$of a successive image, where I_{xy} and K_{xy} are the intensity profile of the images[64]. To calculate the x displacement, we summed the image columns to obtain its x-profile, $I_x(i) = \sum_{y=0}^{n} I_{iy}$, and then subtracted the mean from the profile $I'_x(i) = I_x(i) - \overline{I_x(i)}$. The mean-subtracted profile of the kernel image $K'_x(i)$ was calculated accordingly. The cross-correlation between $I'_x(i)$ and $K'_x(i)$ was performed in Fourier space to increase computational efficiency[65]:

$$C_{xx} = IFFT(FFT(I'_x(i)) * \overline{FFT(K'_x(i))}) \, . \qquad (3.2)$$

Following common practice, the peak of the cross-correlation was then fitted to a parabola function and the displacement in x direction was derived from the peak of the parabola fitting function. Displacement in the y direction was calculated analogously (Figure 5.4).

Cy5-Microtubule and GFP-Kinesin binding assay

GFP-labeled motor protein drosophila kinesin1 with his-tag was expressed (plasmid as a generous gift from Prof. W. Hancock, Pennsylvania State University)[66] and purified by Ni-affinity chromatography using Ni-NTA supferflow resins (Qiagen) as described previously[67,68]. Tubulins were prepared from bovine brains as described[69], and labeled with Cy-5 dye (GE Healthcare, PA15101) following the tubulin conjugation protocol[70] with minor modification. Microtubules were polymerized from a mixture of Cy-5 labeled tubulins and unlabeled tubulins (labeled:unlabeled 1:1) in BRB80 buffer (80mM PIPES, 1mM $MgCl_2$, 1mM EGTA, pH6.8) supplemented with 4mM $MgCl_2$ and 1mM GTP. The mixture was incubated at 37°C for 20 minutes and polymerized microtubules were stabilized with 20μM taxol. For the binding assay, the flow chamber was prepared as above. Microtubules were immobilized on the coverslip by sequentially flowing through protein A (Sigma-Aldrich, P7837) and anti-α tubulin antibody (Sigma-Aldrich, T6074), followed by 0.1mg/ml of microtubules. During each step, incubation lasted for 20 minutes and extra proteins were washed out with 5 chamber volumes of BRB80 buffer supplemented with 10uM taxol. Lastly, kinesins in BRB80 buffer supplemented with 10μM taxol and 1mM adenosine 5'-(β,γ-imido)triphosphate (AMP-PNP) were introduced into the chamber. The sample was visualized in TIRFM.

5.7 Bibliography

1. Schuster, M., Lipowsky, R., Assmann, M.-A., Lenz, P. & Steinberg, G. Transient binding of dynein controls bidirectional long-range motility of early endosomes. *Proc. Natl. Acad. Sci.* **108,** 3618–3623 (2011).
2. Kinosita, K. *et al.* Dual-view microscopy with a single camera: real-time imaging of molecular orientations and calcium. *J. Cell Biol.* **115,** 67–73 (1991).

3. Steinberg, G. *et al.* Motor-driven motility of fungal nuclear pores organizes chromosomes and fosters nucleocytoplasmic transport. *J. Cell Biol.* **198,** 343–355 (2012).
4. Koyama-Honda, I. *et al.* Fluorescence Imaging for Monitoring the Colocalization of Two Single Molecules in Living Cells. *Biophys. J.* **88,** 2126–2136
5. Feinstein, T. N. *et al.* Noncanonical control of vasopressin receptor type 2 signaling by retromer and arrestin. *J. Biol. Chem.* (2013).
6. Degtyar, V., Hafez, I. M., Bray, C. & Zucker, R. S. Dance of the SNAREs: Assembly and Rearrangements Detected with FRET at Neuronal Synapses. *J. Neurosci.* **33,** 5507–5523 (2013).
7. Förster, T. Zwischenmolekulare Energiewanderung und Fluoreszenz. *Ann. Phys.* **437,** 55–75 (1948).
8. Helms, V. *Principles of Computational Cell Biology*. (Wiley, 2008).
9. Harris, D. C. *Quantitative Chemical Analysis*. (Macmillan, 2010).
10. Prabhat, P., Ram, S., Ward, E. S. & Ober, R. J. Simultaneous imaging of different focal planes in fluorescence microscopy for the study of cellular dynamics in three dimensions. *NanoBioscience IEEE Trans. On* **3,** 237–242 (2004).
11. Prabhat, P. *et al.* Elucidation of intracellular recycling pathways leading to exocytosis of the Fc receptor, FcRn, by using multifocal plane microscopy. *Proc. Natl. Acad. Sci.* **104,** 5889–5894 (2007).
12. Sun, Y., McKenna, J. D., Murray, J. M., Ostap, E. M. & Goldman, Y. E. Parallax: High Accuracy Three-Dimensional Single Molecule Tracking Using Split Images. *Nano Lett.* **9,** 2676–2682 (2009).
13. Toprak, E., Balci, H., Blehm, B. H. & Selvin, P. R. Three-Dimensional Particle Tracking via Bifocal Imaging. *Nano Lett.* **7,** 2043–2045 (2007).
14. Kaul, N. The effect of tubulin acetylation and detyrosination on the in vitro motility of kinesin-1. (University of Michigan, 2012).
15. Goshtasby, A. A. *2-D and 3-D Image Registration: for Medical, Remote Sensing, and Industrial Applications*. (John Wiley & Sons, 2005).
16. Goshtasby, A. Image registration by local approximation methods. *Image Vis. Comput.* **6,** 255–261 (1988).

17. Erickson, H. P. The Structure and Assembly of Microtubules. *Ann. N. Y. Acad. Sci.* **253,** 60–77 (1975).
18. Stephens, R. E. & Edds, K. T. Microtubules: structure, chemistry, and function. *Physiol. Rev.* **56,** 709–777 (1976).
19. Vale, R. D. Intracellular transport using microtubule-based motors. *Annu. Rev. Cell Biol.* **3,** 347–378 (1987).
20. Hoyt, M. A., Totis, L. & Roberts, B. T. S. cerevisiae genes required for cell cycle arrest in response to loss of microtubule function. *Cell* **66,** 507–517 (1991).
21. *Microtubule Dynamics - Methods and Protocols*.
22. Alberts, B., Wilson, J. H. & Hunt, T. *Molecular biology of the cell*. (Garland Science, 2008).
23. Svoboda, K., Schmidt, C. F., Schnapp, B. J. & Block, S. M. Direct observation of kinesin stepping by optical trapping interferometry. *Nature* **365,** 721–7 (1993).
24. Schnitzer, M. J. & Block, S. M. Kinesin hydrolyses one ATP per 8-nm step. *Nature* **388,** 386–90 (1997).
25. Rice, S. *et al.* A structural change in the kinesin motor protein that drives motility. *Nature* **402,** 778–784 (1999).
26. Block, S. M., Goldstein, L. S. & Schnapp, B. J. Bead movement by single kinesin molecules studied with optical tweezers. *Nature* **348,** 348–52 (1990).
27. Moffitt, J. R., Chemla, Y. R., Smith, S. B. & Bustamante, C. Recent advances in optical tweezers. *Annu Rev Biochem* **77,** 205–28 (2008).
28. De Vlaminck, I. & Dekker, C. Recent advances in magnetic tweezers. *Annu. Rev. Biophys.* **41,** (2012).
29. Neuman, K. C., Lionnet, T. & Allemand, J. F. Single-molecule micromanipulation techniques. *Annu. Rev. Mater. Res.* **37,** 33–67 (2007).
30. Strick, T. R., Allemand, J. F., Bensimon, D. & Croquette, V. Behavior of supercoiled DNA. *Biophys J* **74,** 2016–28 (1998).
31. Vilfan, I. D., Lipfert, J., Koster, D. A., Lemay, S. G. & Dekker, N. H. in *Handbook of Single-Molecule Biophysics* 371–395 (Springer New York, 2009).

32. Lipfert, J., Koster, D. A., Vilfan, I. D., Hage, S. & Dekker, N. H. Single-molecule magnetic tweezers studies of type IB topoisomerases. *Methods Mol Biol* **582,** 71–89 (2009).
33. Bancaud, A. *et al.* Structural plasticity of single chromatin fibers revealed by torsional manipulation. *Nat Struct Mol Biol* **13,** 444–50 (2006).
34. Bryant, Z. *et al.* Structural transitions and elasticity from torque measurements on DNA. *Nature* **424,** 338–41 (2003).
35. Oberstrass, F. C., Fernandes, L. E. & Bryant, Z. Torque measurements reveal sequence-specific cooperative transitions in supercoiled DNA. *Proc. Natl. Acad. Sci.* **109,** 6106–6111 (2012).
36. Lipfert, J., Kerssemakers, J. J. W., Rojer, M. & Dekker, N. H. A method to track rotational motion for use in single-molecule biophysics. *Rev Sci Instrum* **82,** 103707 (2011).
37. Janssen, X. J. A. *et al.* Electromagnetic Torque Tweezers: A Versatile Approach for Measurement of Single-Molecule Twist and Torque. *Nano Lett.* **12,** 3634–3639 (2012).
38. Lee, S.-J. *et al.* Dynamic look at DNA unwinding by a replicative helicase. *Proc. Natl. Acad. Sci.* **111,** E827–E835 (2014).
39. Blanchard, S. C., Gonzalez, R. L., Kim, H. D., Chu, S. & Puglisi, J. D. tRNA selection and kinetic proofreading in translation. *Nat. Struct. Mol. Biol.* **11,** 1008–1014 (2004).
40. Zhuang, X. *et al.* A Single-Molecule Study of RNA Catalysis and Folding. *Science* **288,** 2048–2051 (2000).
41. Shroff, H. *et al.* Dual-color superresolution imaging of genetically expressed probes within individual adhesion complexes. *Proc. Natl. Acad. Sci.* **104,** 20308–20313 (2007).
42. Neuman, K. C. & Nagy, A. Single-molecule force spectroscopy: optical tweezers, magnetic tweezers and atomic force microscopy. *Nat Methods* **5,** 491–505 (2008).
43. Lavelle, C. Forces and torques in the nucleus: chromatin under mechanical constraints. *Biochem Cell Biol* **87,** 307–22 (2009).
44. La Porta, A. & Wang, M. D. Optical torque wrench: angular trapping, rotation, and torque detection of quartz microparticles. *Phys Rev Lett* **92,** 190801 (2004).

45. Wang, M. D. *et al.* Force and velocity measured for single molecules of RNA polymerase. *Science* **282,** 902–7 (1998).
46. Wang, M. D., Yin, H., Landick, R., Gelles, J. & Block, S. M. Stretching DNA with optical tweezers. *Biophys J* **72,** 1335–46 (1997).
47. Strick, T. R., Allemand, J. F., Bensimon, D. & Croquette, V. Behavior of supercoiled DNA. *Biophys J* **74,** 2016–28 (1998).
48. Lipfert, J., Kerssemakers, J. W., Jager, T. & Dekker, N. H. Magnetic torque tweezers: measuring torsional stiffness in DNA and RecA-DNA filaments. *Nat Methods* **7,** 977–80 (2010).
49. Gore, J. *et al.* Mechanochemical analysis of DNA gyrase using rotor bead tracking. *Nature* **439,** 100–4 (2006).
50. Lipfert, J., Koster, D. A., Vilfan, I. D., Hage, S. & Dekker, N. H. Single-molecule magnetic tweezers studies of type IB topoisomerases. *Methods Mol Biol* **582,** 71–89 (2009).
51. Revyakin, A., Ebright, R. H. & Strick, T. R. Promoter unwinding and promoter clearance by RNA polymerase: detection by single-molecule DNA nanomanipulation. *Proc Natl Acad Sci* **101,** 4776–80 (2004).
52. Revyakin, A., Liu, C., Ebright, R. H. & Strick, T. R. Abortive initiation and productive initiation by RNA polymerase involve DNA scrunching. *Science* **314,** 1139–43 (2006).
53. Ma, J., Bai, L. & Wang, M. D. Transcription Under Torsion. *Science* **340,** 1580–1583 (2013).
54. Harada, Y. *et al.* Direct observation of DNA rotation during transcription by Escherichia coli RNA polymerase. *Nature* **409,** 113–5 (2001).
55. Lionnet, T., Spiering, M. M., Benkovic, S. J., Bensimon, D. & Croquette, V. Real-time observation of bacteriophage T4 gp41 helicase reveals an unwinding mechanism. *Proc Natl Acad Sci* **104,** 19790–19795 (2007).
56. Yu, J., Cheng, W., Bustamante, C. & Oster, G. Coupling translocation with nucleic acid unwinding by NS3 helicase. *J Mol Biol* **404,** 439–55 (2010).
57. Klaue, D. *et al.* Fork sensing and strand switching control antagonistic activities of RecQ helicases. *Nat Commun* **4,** (2013).

58. Blumberg, S., Gajraj, A., Pennington, M. W. & Meiners, J.-C. Three-Dimensional Characterization of Tethered Microspheres by Total Internal Reflection Fluorescence Microscopy. *Biophys. J.* **89,** 1272–1281 (2005).
59. Ruthardt, N., Lamb, D. C. & Brauchle, C. Single-particle Tracking as a Quantitative Microscopy-based Approach to Unravel Cell Entry Mechanisms of Viruses and Pharmaceutical Nanoparticles. *Mol Ther* **19,** 1199–1211 (2011).
60. Liu, L., Woolf, A., Rodriguez, A. W. & Capasso, F. Absolute position total internal reflection microscopy with an optical tweezer. *Proc. Natl. Acad. Sci.* **111,** E5609–E5615 (2014).
61. Li, C. H., Bai, L., Li, D. D., Xia, S. & Xu, T. Dynamic tracking and mobility analysis of single GLUT4 storage vesicle in live 3T3-L1 cells. *Cell Res.* **14,** 480–486 (2004).
62. Olveczky, B. P., Periasamy, N. & Verkman, A. S. Mapping fluorophore distributions in three dimensions by quantitative multiple angle-total internal reflection fluorescence microscopy. *Biophys. J.* **73,** 2836–2847 (1997).
63. Anderson, C. M., Georgiou, G. N., Morrison, I. E., Stevenson, G. V. & Cherry, R. J. Tracking of cell surface receptors by fluorescence digital imaging microscopy using a charge-coupled device camera. Low-density lipoprotein and influenza virus receptor mobility at 4 degrees C. *J. Cell Sci.* **101 (Pt 2),** 415–425 (1992).
64. Gelles, J., Schnapp, B. & Sheetz, M. Tracking kinesin-driven movements with nanometre-scale precision. *Nature* **331,** 450–453 (1988).
65. Van Loenhout, M. T. J., Kerssemakers, J. W. J., De Vlaminck, I. & Dekker, C. Non-Bias-Limited Tracking of Spherical Particles, Enabling Nanometer Resolution at Low Magnification. *Biophys. J.* **102,** 2362–2371 (2012).
66. Shastry, S. & Hancock, W. O. Neck linker length determines the degree of processivity in kinesin-1 and kinesin-2 motors. *Curr Biol* **20,** 939–43 (2010).
67. Walter, W. J., Beránek, V., Fischermeier, E. & Diez, S. Tubulin Acetylation Alone Does Not Affect Kinesin-1 Velocity and Run Length In Vitro. *PLoS ONE* **7,** e42218 (2012).
68. Case, R. B., Pierce, D. W., Hom-Booher, N., Hart, C. L. & Vale, R. D. The directional preference of kinesin motors is specified by an element outside of the motor catalytic domain. *Cell* **90,** 959–966 (1997).

69. Mitchison, T. & Kirschner, M. Microtubule assembly nucleated by isolated centrosomes. *Nature* **312,** 232–237 (1984).
70. Peloquin, J., Komarova, Y. & Borisy, G. Conjugation of fluorophores to tubulin. *Nat. Methods* **2,** (2005).

Chapter 6

CONCLUSIONS AND FUTURE WORK

The work presented in this thesis is directed towards combining two powerful tools in single-molecule biophysical investigations, force spectroscopy and fluorescence imaging. I believe that the progress made in both methodologies in a single instrument offers new opportunities to study biological processes beyond the temporal and spatial resolution achievable with previous approaches. The instrumentation presented in this work is also sufficiently flexible to integrate further functionalities to meet specific experimental needs. I will discuss prospective studies allowed by these instrumentations as well as potential further technical advancement.

6.1 Conclusions and Future work

Single molecule force spectroscopy and single molecule fluorescence microscopy have both evolved in the past several decades and become extremely powerful tools for studying molecular mechanisms in biophysical researches and materials science[1–3]. The work presented in this thesis presented a platform through which force/torque spectroscopy and fluorescence microscopy can be combined to explore undiscovered knowledge about biological processes that are beyond the capability of either methodology when adopted alone. The development of the electromagnetic tweezers (eMT) with the capability of independent force and torque control, described in chapter 2 and chapter 3, offers the control with more flexibility in manipulating the mechanics of the biomolecules under study. The implementation of the high-bandwidth control circuitry and active temperature regulation may allow the eMT system to be operated in both force/torque-clamp and force/torque ramp modes, which has been a challenge in the conventional magnetic tweezers based on permanent magnets. The development of the oblique dark-field scattering system (ODFS), described in chapter 4, allows tracking rotational motion of biomolecules via electrical signals acquired by optoelectronic devices, allowing angular detection with higher bandwidth and without high computational demands of digital image processing required by image based detection methods. Furthermore, the method does not interfere with the biological fluorescence detection, allowing the system to be integrated into fluorescence microscopy without compromising the detection of fluorescently labeled biomolecules. The development of the dual-color bifocal imaging system (DBI), described in chapter 5, allows recording of two chromatically distinguished fluorescent species truly simultaneously using a single CCD camera, with the aberration inherited from the microscope optical system minimized. The independent adjustment of focus of the device in two separate channels also gives the system the capability of detecting fluorescently labeled molecules independently from monitoring the mechanical states when the force probe is located at a different sample plane.

When these three components are integrated together, the magnetic trapping platform described in this thesis makes possible simultaneous force/torque spectroscopy and fluorescence imaging, allowing one to apply force and torque to biomolecules and monitor their torsional status simultaneously with the fluorescence particle tracking and FRET measurements for investigating the dynamics of the spatial distribution of biomolecules and the kinetics of their interaction (Figure 6.1). This integral system has the potential to allow a variety of novel investigations to address a wide range of essential

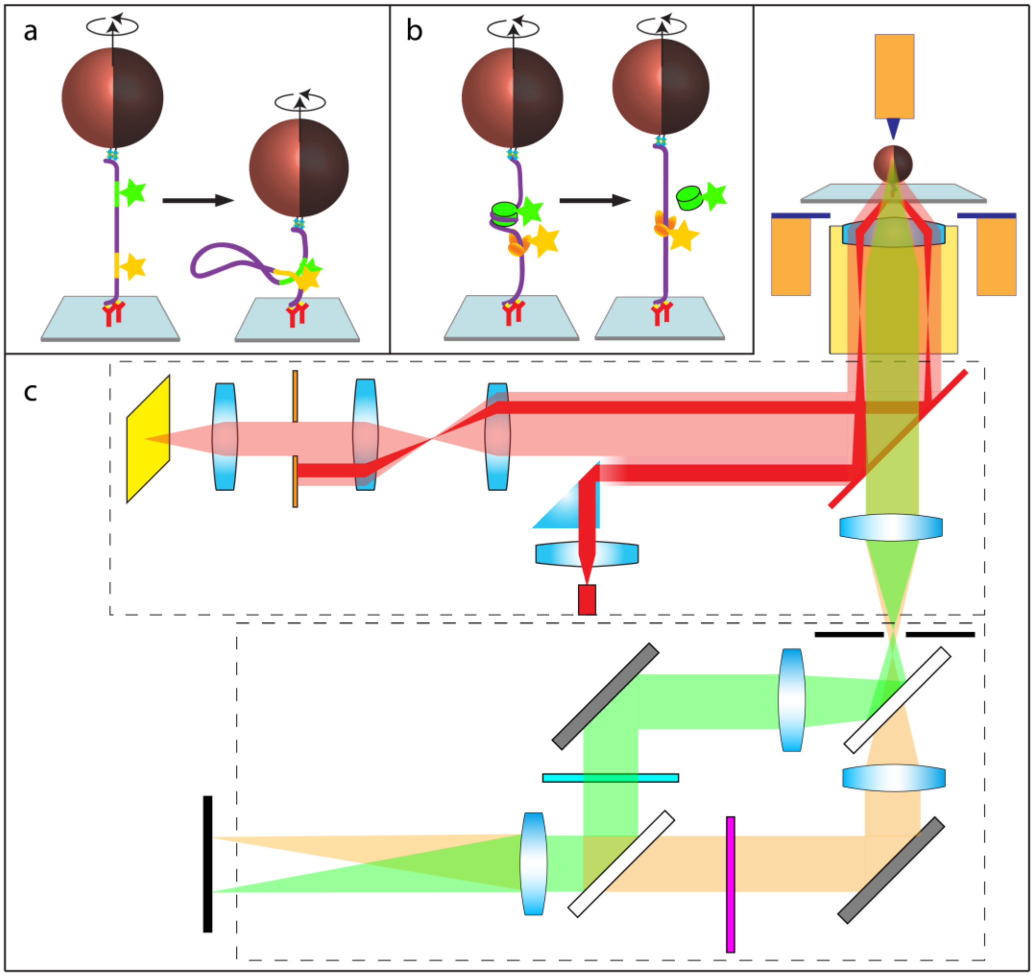

Figure 6.1 Prospective investigations of biological processes using combination of force spectroscopy and fluorescence microscopy. (a) A prospective study to investigate the dynamics of the interaction between enhancer and promotor regions of a DNA molecule. (b) A prospective study to investigate the interaction between a RNAP translocating along a DNA molecule during transcription and a nucleosome assem. In both experiments, the supercoiling status and tension in the DNA molecule are controlled by eMT and its torsional status is monitored by ODFS. DNA segments and biomolecules under study are labeled by fluorescent dye molecules. (c) Integral magnetic trapping platform composed of eMT, ODFS, and DBI integrated into a epifluorescence microscope.

biological questions. For example, the system can be used to study the dependence of interaction dynamics between enhancer and promoter on the mechanical status of the DNA molecule (Figure 6.1 a). Enhancers are regulatory elements in a DNA sequence that can activate gene transcription by communicating with a promoter, often over a considerable distance. They stimulate transcription by recruiting tissue-specific transcription factors, RNAP and other co-factors involved in transcriptional activation[4–6]. A favored model for enhancer-mediated activation of gene transcription is that enhancers are brought into proximity with promoters, and that this interaction is necessary for recruiting the transcriptional machinery[7,8]. Recently it has been shown that such interaction are dependent on the intrinsic structure and topology of DNA, which is in turn related to the mechanical properties of the DNA molecule[9,10]. I believe that the required mechanical analysis of DNA can be advanced in the integral system described above. Another example is to study the interaction between the RNAP and nucleosome barriers that RNAP has to overcome during transcription in eukaryotic cells (Figure 6.1b). During transcription in nucleus, RNAP must transcribe genes in the chromatin environment *in vivo* where DNA is packaged as chromatin, a nucleoprotein complex composed of repeating nucleosomes with DNA wrapped around them[11,12]. Both the kinetics of the translocation of RNAP along DNA during transcription and the association dynamics of nucleosomes to DNA are related to the tensional and torsional status of the template DNA molecule[13–17]. If the histones in the nucleosomes and RNAP are both fluorescently labeled, through FRET measurements, the kinetic information of the interaction between RNAP and nucleosomes during their encounter can be revealed. This method can further be applied to study histones with post translational modifications such as acetylation, methylation, and phosphorylation, to potentially improve our understanding on the epigenetic modification on gene regulations[18–22].

There are scenarios where high temporal and spatial resolution of control and detection of biological processes prove to be challenging. For example, during the investigation of the dependence of enzymatic reaction kinetics on the mechanical properties of the involved biomolecules, such as the relation between the elongation rate of RNAP during transcription and the torsion stored in the template DNA molecule, or that between the rate of ATP hydrolysis in ATP synthases and the torque applied to the synthases, the torsion/tension-clamp to maintain the constant mechanical condition is desired. To conduct such experiments where active feedback is required, it remains challenging to implement the closed-loop control in real time to match the biological reaction rates in natural conditions. The hydrodynamic force experienced by force probes of micron size, which is orders of magnitude larger than that experienced by the biomolecules under study, may compromise the temporal resolution of the observable steps in the reaction pathway, hiding transient events important to understanding enzymatic reactions under *in vivo* conditions. There is a need to develop novel types of force probes, possibly requiring composition of new materials, which have sizes compatible with the biomolecules and suitable for desired experimental bandwidth, yet at the same time allow application of sufficiently strong force and torsional stress to the biomolecules under study. Another challenge encountered in the implementation of combining magnetic trapping and fluorescence imaging is the auto-fluorescence of magnetic force probes resulting in background fluorescence that interferes with fluorescence detection of fluorescently labeled biomolecules of interest. In past works this issue was usually addressed by using long molecular spacers combined with TIRFM to place the force probe completely outside of the penetration depth of the evanescent field of TIRFM[10,23,24]. To avoid the interference between the fluorescence emitted from the force probes and that from fluorescently-labeled biomolecules for the purpose of accommodating a wider range of experiment schemes, beads with a narrow fluorescence emission spectrum are needed so that the different fluorescence signals can be spectrally separated to improve signal to noise ratio of single molecule fluorescence detection.

Further advancement of instrumentation to integrate cerain functions is beneficial, and in some cases crucial, to meet the requirements of specific biophysical studies. For example, integrating position tracking in the ODFS system to allow detection of motion with more degrees of freedom is important when position information is needed for calibrating the tensile force applied to the biomolecule, and deconvolution between position and rotary motion detection is crucial to avoid crosstalk. Furthermore, instrumentation that allows independent control of force and torque along multiple axes can offer more flexibility in studying mechanical properties of more complex systems. Such further advancement of technologies in single-molecules studies, despite the challenges it may present, will offer unprecedented opportunities for addressing a diverse range of novel questions to further our understanding of fundamental biological processes.

6.2 Bibliography

1. Neuman, K. C. & Nagy, A. Single-molecule force spectroscopy: optical tweezers, magnetic tweezers and atomic force microscopy. *Nat Methods* **5,** 491–505 (2008).
2. Lipfert, J., van Oene, M. M., Lee, M., Pedaci, F. & Dekker, N. H. Torque spectroscopy for the study of rotary motion in biological systems. *Chem. Rev.* (2014).

3. Juette, M. F. *et al.* The bright future of single-molecule fluorescence imaging. *Curr. Opin. Chem. Biol.* **20,** 103–111 (2014).
4. Blackwood, E. M. & Kadonaga, J. T. Going the distance: A current view of enhancer action. *Science* **281,** 60–63 (1998).
5. Marsman, J. & Horsfield, J. A. Long distance relationships: enhancer–promoter communication and dynamic gene transcription. *Biochim. Biophys. Acta BBA - Gene Regul. Mech.* **1819,** 1217–1227 (2012).
6. Krivega, I. & Dean, A. Enhancer and promoter interactions—long distance calls. *Curr. Opin. Genet. Dev.* **22,** 79–85 (2012).
7. Dekker, J., Rippe, K., Dekker, M. & Kleckner, N. Capturing chromosome conformation. *Science* **295,** 1306–1311 (2002).
8. Hughes, J. R. *et al.* Analysis of hundreds of cis-regulatory landscapes at high resolution in a single, high-throughput experiment. *Nat. Genet.* **46,** 205–212 (2014).
9. Hegyi, H. Enhancer-promoter interaction facilitated by transiently forming G-quadruplexes. *Sci. Rep.* **5,** (2015).
10. Long, X., Parks, J. W., Bagshaw, C. R. & Stone, M. D. Mechanical unfolding of human telomere G-quadruplex DNA probed by integrated fluorescence and magnetic tweezers spectroscopy. *Nucleic Acids Res.* **41,** 2746–2755 (2013).
11. Jin, J. *et al.* Synergistic action of RNA polymerases in overcoming the nucleosomal barrier. *Nat Struct Mol Biol* **17,** 745–52 (2010).
12. Felsenfeld, G., Clark, D. & Studitsky, V. Transcription through nucleosomes. *Biophys. Chem.* **86,** 231–237 (2000).
13. Vlijm, R. *et al.* Nucleosome Dynamics Involve Spontaneous Fluctuations in the Handedness of Tetrasomes. *Biophys. J.* **106,** 74a (2014).
14. Vlijm, R., Smitshuijzen, J. S. J., Lusser, A. & Dekker, C. NAP1-Assisted Nucleosome Assembly on DNA measured in real time by single-molecule magnetic tweezers. *PLoS ONE* **7,** e46306 (2012).
15. Gupta, P., Zlatanova, J. & Tomschik, M. Nucleosome assembly depends on the torsion in the DNA molecule: a magnetic tweezers study. *Biophys J* **97,** 3150–7 (2009).
16. Ma, J., Bai, L. & Wang, M. D. Transcription under torsion. *Science* **340,** 1580–1583 (2013).

17. Lavelle, C. DNA torsional stress propagates through chromatin fiber and participates in transcriptional regulation. *Nat. Struct. Mol. Biol.* **15,** 123–125 (2008).
18. Grunstein, M. Histone acetylation in chromatin structure and transcription. *Nature* **389,** 349–52 (1997).
19. Libertini, L. J., Ausio, J., van Holde, K. E. & Small, E. W. Histone hyperacetylation. Its effects on nucleosome core particle transitions. *Biophys J* **53,** 477–87 (1988).
20. Greer, E. L. & Shi, Y. Histone methylation: a dynamic mark in health, disease and inheritance. *Nat. Rev. Genet.* **13,** 343–357 (2012).
21. Rossetto, D., Avvakumov, N. & Côté, J. Histone phosphorylation: a chromatin modification involved in diverse nuclear events. *Epigenetics Off. J. DNA Methylation Soc.* **7,** 1098–1108 (2012).
22. Bannister, A. J. & Kouzarides, T. Regulation of chromatin by histone modifications. *Cell Res.* **21,** 381–395 (2011).
23. Lee, M., Kim, S. H. & Hong, S.-C. Minute negative superhelicity is sufficient to induce the B-Z transition in the presence of low tension. *Proc. Natl. Acad. Sci.* **107,** 4985–4990 (2010).
24. Hugel, T. *et al.* Experimental test of connector rotation during DNA packaging into bacteriophage φ29 capsids. *PLoS Biol* **5,** e59 (2007).